

ULS analysis of FRP composite sandwich plates

Sandwich PULS – development of a semi-analytical method

Master's Thesis in the International Master's Programme Naval Architecture and Ocean Engineering

NIKLAS BLOMGREN AND MATEJ PREVC

Department of Shipping and Marine Technology
Division of Marine Technology
CHALMERS UNIVERSITY OF TECHNOLOGY
Gothenburg, Sweden 2015
Master's thesis 2015:X-15/325

MASTER'S THESIS IN THE INTERNATIONAL MASTER'S PROGRAMME IN
NAVAL ARCHITECTURE AND OCEAN ENGINEERING

ULS analysis of FRP composite sandwich plates

Sandwich PULS – development of a semi-analytical method

NIKLAS BLOMGREN AND MATEJ PREVC

Department of Shipping and Marine Technology
Division of Marine Technology
CHALMERS UNIVERSITY OF TECHNOLOGY
Gothenburg, Sweden 2015

ULS analysis of FRP composite sandwich plates -
Sandwich PULS – development of a semi-analytical method
NIKLAS BLOMGREN AND MATEJ PREVC

© NIKLAS BLOMGREN AND MATEJ PREVC, 2015

Master's Thesis 2015:X-15/325
ISSN 1652-8557
Department of Shipping and Marine Technology
Division of Marine Technology
Chalmers University of Technology
SE-412 96 Gothenburg
Sweden
Telephone: + 46 (0)31-772 1000

Cover:
First buckling mode of an FRP composite sandwich plate, from Abaqus CAE (in front),
and a piece of the Sandwich PULS code written in Fortran code (in back).

Chalmers Reproservice
Gothenburg, Sweden 2015

ULS analysis of FRP composite sandwich plates -
Sandwich PULS – development of a semi-analytical method
*Master's Thesis in the International Master's Programme in Naval Architecture and
Ocean Engineering*
NIKLAS BLOMGREN AND MATEJ PREVC
Department of Shipping and Marine Technology
Division of Marine Technology
Chalmers University of Technology

ABSTRACT

The use of fibre-reinforced polymers (FRP) composite sandwich structures is desirable because of their advantages compared to using steel structures. Many of the advantages are due to reduced weight, for example improved stability, lower fuel consumption, higher top speed, and increase in payload. Other advantages such as lower maintenance and long fatigue life contribute to an overall lower lifetime cost. A sandwich plate is a three-layer geometry consisting of two thin faces separated by a thick core.

The purpose of this thesis is to develop Sandwich PULS; a semi-analytical calculation tool for predicting the ultimate limit state (ULS) of FRP composite sandwich plates. This was done by extending and improving DNV GL's semi-analytical non-expert calculation tool Composite PULS, which is used for quick estimation of the ULS for unstiffened composite plates. ULS was evaluated in terms of the first buckling load and the first ply failure (FPF).

The Sandwich PULS code was developed by implementing formulations for sandwich plate theory. First-order shear deformation theory (FSDT) was implemented in Sandwich PULS to include the transverse shear deformations that are highly important for sandwich plates with poor shear stiffness of the core. The Sandwich PULS code was evaluated against non-linear finite element analyses (FEA).

It was concluded that Sandwich PULS shows good agreement with FEA predicted critical buckling loads. For all inspected plates, Sandwich PULS shows improved results compared to Composite PULS. Differences between Sandwich PULS and FEA are caused by the difference in evaluating shear stiffness. It has been shown that neglecting shear stiffness of faces results in good agreement between Sandwich PULS and FEA, while use of conventional shear correction factors proved to be unfavourable for sandwich plates.

It was found that Sandwich PULS is limited in terms of slenderness. Sandwich plates with soft core should not have slenderness below 20 to assure an accurate solution. FPF loads according to Hashin-Rotem failure criteria are on the conservative side, but differences compared to FEA are up to 40% for sandwich plates. It was concluded that a more extensive investigation of failure initiation load prediction should be performed for better understanding.

Key words: Buckling, fibre-reinforced polymers, first-order shear deformation theory, sandwich plates, semi-analytical method, shear correction factor, ultimate limit state.

Contents

ABSTRACT	I
CONTENTS	III
PREFACE	VII
NOTATIONS	IX
1 INTRODUCTION AND MOTIVATION	1
1.1 Background	1
1.2 Objectives	4
1.3 Methodology	4
1.4 Limitations and assumptions	5
1.5 Outline of the thesis	6
2 THEORETICAL BACKGROUND	7
2.1 Composite materials	7
2.2 ULS prediction of composite and sandwich plates	8
2.3 Failure modes	10
2.4 Failure criteria	11
2.4.1 Face wrinkling	11
2.4.2 Shear crimping	12
2.4.3 Hashin-Rotem and Hashin failure criteria	12
2.5 The PULS and Composite PULS codes	13
3 SANDWICH PULS	15
3.1 Kinematics and displacement field	16
3.2 Energy contributions	17
3.3 Shear stiffness implementation	18
3.4 Solution procedure	19
3.4.1 Eigenvalue analysis	20
3.4.2 Incremental solution method	21
3.4.3 Procedure for solving incremental equations	21
3.4.4 Failure initiation	23
4 FINITE ELEMENT ANALYSIS	25
4.1 Model set up	25
4.2 Load cases and boundary conditions	25
4.2.1 Uniaxial and biaxial load cases	26
4.2.2 Axial longitudinal/in-plane shear load cases	26
4.3 Element type	26

4.4	Analysis steps	30
4.5	Mesh convergence study	31
5	RESULTS AND DISCUSSION	33
5.1	Eigenvalue analysis	34
5.1.1	Sandwich Plate System (SPS)	34
5.1.2	Single-skin FRP Composite plate	35
5.1.3	FRP Sandwich plate 1	36
5.1.4	FRP Sandwich plate 2	37
5.1.5	Concluding remarks	38
5.2	Load-displacement analysis	38
5.2.1	Sandwich Plate System (SPS)	39
5.2.2	Single-skin FRP Composite plate	39
5.2.3	FRP Sandwich plate 1	40
5.2.4	FRP Sandwich plate 2	41
5.2.5	Concluding remarks	42
5.3	Failure initiation analysis	42
5.3.1	Hashin-Rotem failure criteria	42
5.3.2	Sandwich failure criteria	45
5.3.3	Concluding remarks	46
5.4	Sandwich PULS sensitivity studies	46
5.4.1	Breadth-to-thickness ratio	46
5.4.2	Face-to-core stiffness ratio	47
5.4.3	Aspect ratio	50
5.4.4	Concluding remarks	52
6	CONCLUSIONS	53
7	RECOMMENDATIONS FOR FUTURE WORK	55
8	REFERENCES	57
APPENDIX A – MATERIAL DATA		A1
A.1	Sandwich Plate System (SPS)	A1
A.2	Single-skin FRP Composite plate	A2
A.3	FRP Sandwich plate 1	A3
A.4	FRP Sandwich plate 2	A4
APPENDIX B – FIRST-ORDER SHEAR DEFORMATION THEORY		B1
APPENDIX C – ANISOTROPIC PLATE THEORY		C1
APPENDIX D – ENERGY PRINCIPLES		D1

D.1	Potential energy	D1
D.2	The principle of virtual work	D2
D.3	The principle of stationary potential energy	D2
APPENDIX E – THE RAYLEIGH-RITZ METHOD		E1
E.1	General introduction	E1
E.2	Displacement functions	E3
E.3	Differentiated displacement functions	E3
E.4	Energy contributions	E4
E.5	Integrals used in the Rayleigh-Ritz method	E7
E.6	Final expressions for energy contribution	E9
APPENDIX F – DERIVED STIFFNESS MATRICES		F1
F.1	Derivation process	F1
F.2	Derived eigenvalue stiffness matrices	F2
APPENDIX G – HASHIN-ROTEM/HASHIN (ABAQUS)		G1

Preface

This thesis is a part of the requirements for the master's degree in Naval Architecture and Ocean Engineering at Chalmers University of Technology, Gothenburg. The work of the thesis has been carried out between January and June of 2015 at the Division of Marine Technology, Department of Shipping Marine Technology, Chalmers University of Technology, in cooperation with DNV GL, Department of Technical Advisory – Structures in Høvik, Norway.

We would like to acknowledge and thank our examiner and supervisor, Professor Jonas Ringsberg, at the Department of Shipping and Marine Technology for his excellent guidance and support throughout the work with this thesis.

Further, we would like to acknowledge and thank our supervisor Dr. Philippe Noury along with Dr. Lars Brubak, Ole Jakob Hareide, M.Sc., and Jonas Boström, M.Sc., at DNV GL for their excellent supervision and guidance. We would like to express our gratitude to everyone at the DNV GL office for making it a pleasant working environment.

The project was financed through the Rolf Sörmans scholarship fund and through the Ad Futura scholarship from the Slovene Human Resources and Scholarship Fund.

Finally, it should be noted that the thesis could never have been conducted without the support from our families and friends.

Gothenburg, June 2015

Niklas Blomgren and Matej Prevc

Notations

Roman upper case letters

A	Displacement amplitude	[mm]
$\{A\}$	Displacement amplitude vector	[mm or -]
$[A]$	Extensional stiffness matrix	[N/mm]
$[A_s]$	Shear stiffness matrix	[N/mm]
B	Shear strain amplitude (xz-plane)	[-]
$[B]$	Extension-bending coupling stiffness matrix	[N]
C	Shear strain amplitude (yz-plane)	[-]
D_{ij}	Section stiffness (Abaqus)	[Nmm]
$[D]$	Bending stiffness matrix	[Nmm]
E	Young's modulus	[MPa]
F	Airy's stress function	[N]
G	Shear modulus	[MPa]
$\{G\}$	Incremental load vector	[N/mm or N]
K	Shear correction factor	[-]
K_{ij}	Shear stiffness (Abaqus)	[N/mm]
$[K]$	Incremental stiffness matrix	[N/mm or N or Nmm]
$[K^G]$	Geometric stiffness matrix	[N/mm or N or Nmm]
$[K^M]$	Material stiffness matrix	[Nmm or -]
M	Number of degrees of freedom along the longitudinal direction	[-]
N	Number of degrees of freedom along the transverse direction	[-]
P^N	Preload	[N]
Q^N	Reference load	[N]
$[Q]$	Stiffness matrix	[MPa]
S	Shear strength	[MPa]
U	Internal potential energy	[Nmm]
U_b	Bending strain energy contribution	[Nmm]
U_m	Membrane strain energy contribution	[Nmm]

U_{mb}	Extension-bending coupling energy contribution	[Nmm]
U_p	In-plane strain energy contribution	[Nmm]
U_s	Shear strain energy contribution	[Nmm]
W	Load potential from external forces	[Nmm]
X	Longitudinal strength	[MPa]
Y	Transverse strength	[MPa]
Z	Out-of-plane strength	[MPa]

Roman lower case letters

a	Length	[mm]
b	Breadth	[mm]
d	Vertical distance between the midplane of two sandwich plate faces	[mm]
h	Thickness	[mm]
k	Curvature	[-/mm]
l	Characteristic length on the surface of the shell	[mm]
m	Number of half-sine waves along the longitudinal direction	[-]
n	Number of half-sine waves along the transverse direction	[-]
q	Dimensionless displacement (rotation) amplitude	[-]
t	Thickness	[mm]
w	Out-of-plane displacement	[mm]
$w_{0,init}$	Initial out-of-plane displacement (imperfection)	[mm]
x	Longitudinal coordinate	[mm]
y	Transverse coordinate	[mm]
z	Out-of-plane coordinate	[mm]

Greek upper case letters

Λ	Eigenvalue	[-]
Π	Potential energy	[Nmm]

Greek lower case letters

γ	Shear strain	[-]
$\Delta\eta$	Incremental step/Arc-length parameter	[-]
ε	Normal strain	[-]
ε_0	Membrane/Mid-plane strain	[-]
λ_i	Load multiplier	[-]
ν	Poisson's ratio	[-]
σ	Normal stress	[MPa]
τ	Shear stress	[MPa]
ϕ	Rotation	[-]

Subscripts

1	Longitudinal-to-fibre direction
2	Transverse-to-fibre direction
3	Out-of-plane-to-fibre direction
c	Core
C	Compression
f	Face
s	Step
S	Symmetric
T	Tension
x	Longitudinal direction
y	Transverse direction
z	Out-of-plane direction

Abbreviations

BC	Boundary Condition
CLT	Classical Laminate Theory
DOF	Number of Degrees Of Freedom
FCSR	Face-to-Core Stiffness Ratio

FEA	Finite Element Analysis
FFF	First Fibre Failure
FPF	First Ply Failure
FRP	Fibre Reinforced Polymers
FSDT	First-order Shear Deformation Theory
FW	Face Wrinkling
HOT	Higher Order Theories
IMO	International Maritime Organization
LPF	Last Ply Failure
LT	Layer-wise Theories
LTR	Length-to-Thickness Ratio
MT	Matrix Tension failure
MTs	Mixed Theories
PULS	Panel Ultimate Limit State
SC	Shear Crimping
SOLAS	Safety Of Life At Sea
SPS	Sandwich Plate System
ULS	Ultimate Limit State

1 Introduction and motivation

This chapter gives a brief introduction to the problem and motivation behind the work of this thesis.

1.1 Background

Fibre-reinforced polymers (FRP) composites and sandwich structures are becoming more and more used in a large number of applications. Commercial aircraft, such as the new Airbus A350, wind turbine blades and bridges made partially or primarily out of FRP composites have been known and used for many years. In the future, a significant growth in the use of such materials is expected in automotive segments as well. The first fiberglass boats appeared in the early 1940s and FRP composites have been used in boats, yachts, high-speed light craft, naval ships and submarines ever since, Marsh (2006).

As described in Job (2015), the use of FRP composites in the shipbuilding segment is still in its beginning stages. Their use in marine applications has so far been limited to naval vessels and non-structural components in commercial vessels, such as cabins on cruise ships, lifeboats and hatch covers on bulk carriers. Here and in many other applications, FRPs are usually combined with other materials and form so-called FRP sandwich plates. Those are plates with FRP composites used in thin faces and combined with a thick core material, such as balsa wood, PVC foam, honeycomb, etc.

The most commonly used structural material in the shipbuilding segment today is steel. Using FRP composite materials instead of steel can have many advantages, for example:

- higher strength vs. self-weight ratio: reduced weight of structures for the same strength,
- corrosion resistance: no need for corrosion addition to thicknesses,
- long-lasting: lower lifetime costs,
- long fatigue life,
- tailor-made structural components with desired properties,
- reduced magnetic, radar and infra-red signatures,
- dimensional stability: no thermal shrinking or swelling,
- nonconductive: does not conduct electricity,
- thermal isolation: does not conduct heat.

In most cases the important advantage of using FRP composites is structural weight savings, which can be reflected in different ways. One of them is reduced fuel consumption and reduced fuel costs. Hand-in-hand with reduced fuel consumption goes a reduced carbon footprint. Having fluctuating oil prices in mind, another and maybe more intriguing reason is the increase in payload, which results in a shorter payback time. The latter is of great importance especially for cruise ships, since the only possibility to increase their payload is to build up. That is due to the draught, breadth and length limitations for ships in canals and ports. To avoid reduction of ship stability, the use of light-weight structural materials above the waterline is a way to overcome the problem. On the other hand, for naval ships reduced structural weight is of importance to allow for increased speed of the vessel. Adding the fact that composites reduce magnetic, radar and infra-red signatures, one can see why the use of these materials as a structural material has been increasing in naval ships.

Compared with steel, FRP composites have higher upfront costs, but the maintenance and lifetime costs are much lower, Job (2015). Since composites are not corrosive there is not the same need for extensive maintenance, which is another reason why higher initial investment has a rather short payback time. In an investigation done by Evegren et al. (2011), extra structural costs of the composite superstructure on the cruise ship under investigation will be compensated by fuel savings in 5.9 years, but if extra cabin capacity and an increased payload due to this is taken into the calculation the break-even is after about 2.5 years.

One major drawback why composites are not used for commercial ships is fire safety. SOLAS requires structural materials to be non-combustible, which seems to represent an insuperable obstacle for FRP composites. An amendment to the fire safety chapter of SOLAS, see IMO (2004), has loosened this obstacle a bit and paved the way for extensive research and development projects and product development, the goal of which has been to demonstrate the equivalent fire safety for composite applications, Job (2015). Despite all the efforts, no structural FRP solution has been built for a commercial ship.

Another reason for why using FRP composites is rather difficult are their orthotropic properties. On the one hand, structures made out of composites can be tailor-made for its specific use, which is a great advantage. On the other hand, this makes it harder to compare and standardize properties, behaviour and structural response of composite structures. Several research papers can be found on comparing composite plates made under the same circumstances but having different material properties, Hayman et al. (2011).

Estimating ultimate limit state (ULS), which is defined by Hollaway et al. (2001) as the load where the structure fails due to reaching its maximum strength, is even more cumbersome. Furthermore, agreement between results obtained with FEA and experimental results are rather bad and ultimate strengths are often overestimated, Boyle et al. (2001). Due to these uncertainties, definition of the ULS is not the same in literature. It might be referred to as the first buckling load, the first fibre/ply failure load, or, as previously mentioned, the maximum load-carrying capacity.

Current design approaches stated in class regulations for marine single-skin FRP and sandwich constructions are based on the first ply failure or the first buckling load, DNV (2013). To increase safety of such structures and to ensure that these loads will not occur during normal operation, additional safety factors are applied on these loads to obtain the limit load, as illustrated in Figure 1.1.

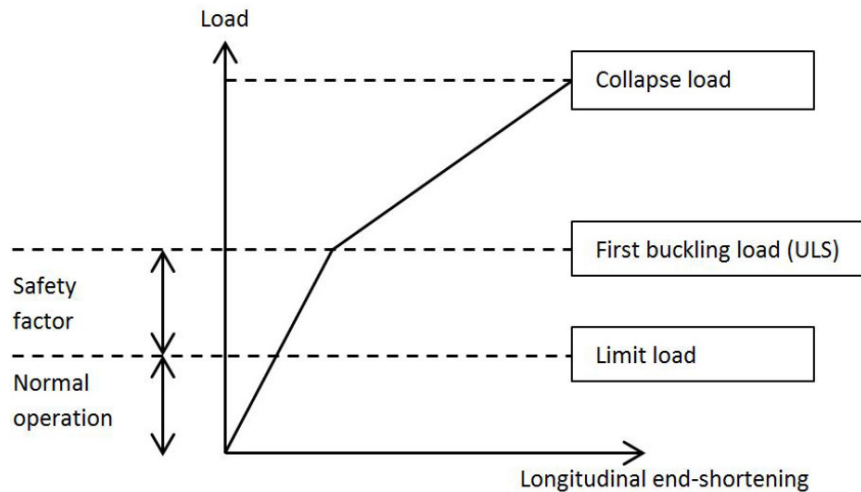


Figure 1.1 Principal load-displacement curve showing different load states for current traditional design approaches, from Braaten and Boström (2013).

The limit load as defined in Figure 1.1 is in many cases overly conservative since FRP composites show additional post-buckling residual strength, which has been the focus of many researches. If uncertainties behind the estimated collapse load are minimized and the estimation of the ULS agrees with experimental results, a less conservative limit load can then be set in class regulations. This is the goal and the idea behind future design approaches, as illustrated in Figure 1.2, which will result in a more optimized but still safe structure.

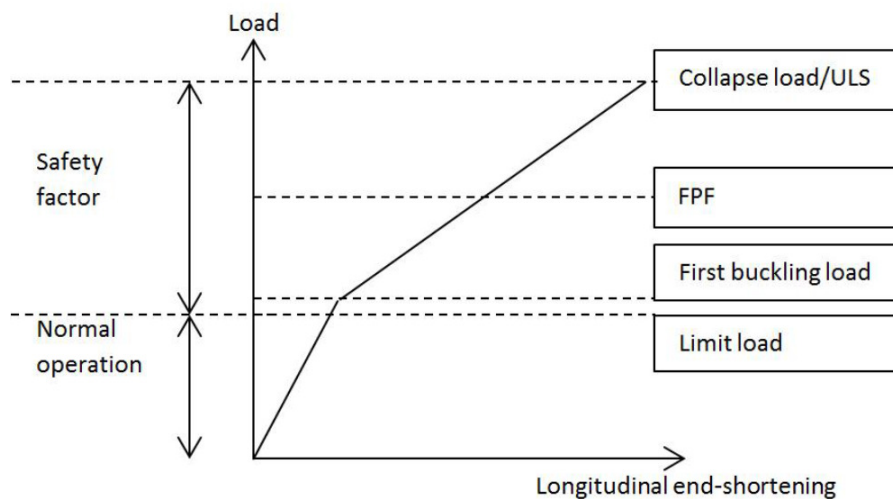


Figure 1.2 Principal load-displacement curve showing different load states for future design approaches, from Braaten and Boström (2013).

While obtaining the FPF and the first buckling load is a rather simple and computational undemanding task, the ULS estimation is a highly complex task, especially for FRP composite structures. In the post-buckling zone non-linear response caused by the large deflection theory and material degradation have to be accounted for, which results in a high computational cost.

The DNV GL's code PULS (Panel Ultimate Limit State), see Steen et al. (2004), has been developed having these high computational, modelling and post-processing times in mind, which is why it comes with certain limitations. PULS is limited to the load

bearing capacity assessment of steel or aluminium thin-walled stiffened panels used in ship and offshore constructions. It is further limited to rectangular, not curved plates. PULS is a recognized buckling evaluation tool and its main purpose is to be a user-friendly, non-expert analyses tool with a low computational cost. The PULS code is implemented and used for automatic buckling controls as part of the DNV GL's Nauticus Hull commercial programs.

Until 2013, the PULS code could only evaluate the buckling response of steel and aluminium panel structures. Since then, a new Composite PULS code, see Braaten and Boström (2013), based on the PULS code has been developed in order to evaluate the ultimate strength of unstiffened composite plates.

The Composite PULS code has certain limitations: it is only applicable to thin symmetric laminates, since the classical laminate plate theory (the Kirchhoff's plate theory) and symmetrical ply degradation model are implemented. It is further limited to simply supported plates and it has been developed for one material only. The purpose of this thesis is to extend the Composite PULS code towards becoming a computational tool that can, with tolerable accuracy and within reasonable computational time, estimate the ULS capacity of FRP composite sandwich plates.

1.2 Objectives

The main objective of this master's thesis project was to develop the semi-analytical method Sandwich PULS based on the Composite PULS code in order to predict the ULS capacity of FRP composite sandwich plates. A comparative investigation of formulations for PULS against non-linear finite element simulations, the Composite PULS code and other existing formulations should be carried out. In order to satisfy the main objectives of the project, the following three main aims have been identified.

- The developed code should incorporate a set of formulations for the PULS code in order to predict the first buckling load of FRP composite sandwich plates.
- The developed code should incorporate a set of formulations for the PULS code in order to predict the FPF of FRP composite sandwich plates.
- The developed code should be validated against an advanced FE analysis based on the same failure initiation criteria.

Further, the project aims for the Sandwich PULS code to remain a computational tool that can with tolerable accuracy, i.e. within approximately 10%, and preferably on the conservative side predict the ULS of sandwich plates. Calculation time of the developed Sandwich PULS code should maintain reasonable, i.e. less than one minute and/or be reasonably faster than commercial FE software.

1.3 Methodology

To predict the ULS of FRP sandwich composite plates the theories behind the existing Composite PULS code had to be extended. First, an extensive investigation on theoretical background was performed on the topic of buckling of single-skin and sandwich plates as well as a detailed study of the principles of the existing Composite PULS code. The extension of the code was done by implementing formulations for sandwich plate theory, as well as replacing the classical laminate theory (CLT) with first-order shear deformation theory (FSDT), see Chapter 3.

The comparative investigation of formulations implemented in Sandwich PULS was performed in three phases:

- Phase 1: Eigenvalue analysis: compare the first buckling loads.
- Phase 2: Load-displacement analysis: compare non-linear model response.
- Phase 3: Failure initiation analysis: compare failure initiation loads.

In every phase, results were compared to non-linear finite element analyses (FEA) and the existing Composite PULS code. The first phase was to perform the eigenvalue buckling analysis. Four plate models with different material setups and geometries, see Appendix A, were used to validate the eigenvalue buckling analysis. The first buckling load was registered for the different plates subjected to different load cases of biaxial or combined longitudinal uniaxial/in-plane shear loading. The second phase was to perform the load-displacement analysis where plates were subjected to uniaxial compression, assuming linear elastic material properties, to investigate model response of the implemented formulations. The same plate models were used in the load displacement analysis as for the eigenvalue buckling analysis. The third phase was to perform failure initiation analyses for the FRP Sandwich plate 2, see Appendix A, subjected to either biaxial or combined longitudinal uniaxial/in-plane shear loading. Finally, a set of sensitivity studies was performed in order to investigate the validity and limitations of the Sandwich PULS code.

The implementation of FSDT and sandwich theory into the Composite PULS code was done using the programming language Fortran 95. The non-linear FEA was done in Abaqus standard version 6.14-2, see Dassault Systèmes (2014). In the non-linear Sandwich PULS analysis and FEA the shape of the lowest buckling mode from the buckling analysis was used as an initial imperfection for the load-displacement and failure analyses.

1.4 Limitations and assumptions

The thesis was carried out in corporation with DNV GL and limited to extending the already existing Composite PULS code. This chapter covers the limitations and assumptions made for the development of the code towards predicting the ULS of sandwich plates.

With the objective of developing the Sandwich PULS code for sandwich plates, the structures investigated were geometrically limited to unstiffened rectangular plates with symmetric layups. The development of the code was limited to ULS in terms of failure initiation from face wrinkling, shear crimping and the Hashin-Rotem failure criterion presented in Chapter 2.4.

The thesis was further limited to only study simply supported plates under uniformly distributed uniaxial, biaxial or combined uniaxial longitudinal/in-plane shear loads, from here on referred to as axial/shear loads. It is believed that these load cases create a good representation of the in-plane loading conditions that occur in a largescale ship structure. Since buckling of plates was of major interest, the thesis was limited to studying in-plane loads only. Disregarding out-of-plane loads, e.g. hydrostatic pressure, wave loads etc., made the analysis less conservative.

Neither simply supported nor clamped boundary conditions are considered as realistic representations able to reproduce the behaviour of hull plates in a largescale ship structure. Plates that are simply supported underestimate the structural stiffness, while clamped plates make it too stiff. The real response lies somewhere in between the two.

Simply supported plates were chosen because they produce lower ultimate loads and by that a conservative result in comparison to clamped plates, Misirlis (2012). Moreover, application of the Rayleigh-Ritz approximation method for clamped plates is difficult, since problems with convergence occur.

Four different plate models were used in the study:

- Sandwich Plate System (SPS): layer-wise isotropic,
- single-skin FRP Composite plate: orthotropic,
- FRP Sandwich plate 1: isotropic core, orthotropic faces,
- FRP Sandwich plate 2: isotropic core, orthotropic faces.

All four plates have various slenderness, i.e. thickness-to-breadth ratio, aspect ratio, material properties and different layups, see Appendix A. Material behaviour was assumed to be linear, while geometrical non-linearities were considered. All plates were assumed to have an initial imperfection in the shape of its first buckling mode, with an amplitude of 0.1% of the plate breadth. Verification of the developed Sandwich PULS code was limited to results created in the FEA software Abaqus. The models in Abaqus were limited to using shell elements.

1.5 Outline of the thesis

In Chapter 1, an introduction to the problem and motivation behind the work is presented. Objectives, methodology, together with the project's limitations and assumptions are included.

In Chapter 2, the theoretical background that the thesis is based on is presented. It gives a general description of composite materials and a description of their failure modes and failure criteria. Related work done by others authors and the existing PULS code is presented here.

In Chapter 3, the newly developed Sandwich PULS code is presented. Main changes in the code due to the implementation of FSDT are described as well as sandwich plate theories and solution procedures.

Chapter 4 presents the FE model and analysis procedure used for validating results with Abaqus. The chapter includes a model set-up, a description of loading cases and boundary conditions, choice of element type, mesh convergence study and analysis steps.

In Chapter 5 results and discussion of results are presented. Results obtained with Sandwich PULS are compared with Composite PULS and validated against Abaqus.

In Chapter 6 conclusions of the thesis are presented.

Chapter 7 presents recommendations for future work.

The Appendix chapters contain material data for plates that have been analysed in this thesis. Further, a description of the theories and derived mathematical expression that have been implemented in Sandwich PULS are presented.

2 Theoretical background

This chapter gives a brief introduction to composite and sandwich materials, a theoretical framework behind the existing PULS code as well as theories and conclusions from related work done by other authors.

2.1 Composite materials

This chapter presents definitions for composite and sandwich materials based on work done by Agarwal et al. (2006) and Zenkert (1997).

A composite material is defined as having two or more distinct constituent materials or phases, but is mostly recognised as a composite material when there are significant differences in the physical properties of the constituent phases. It is the combination of properties from two or more materials that in many cases make them advantageous in comparison to other materials considering strength-to-weight ratio, stiffness, toughness, insulation, among other properties, Agarwal et al. (2006).

These properties vary with the type of constituents and the way the composite is composed. Composites usually consist of a continuous phase embedded with one or more discontinuous phases. Most commonly the discontinuous phases have superior material properties acting as reinforcement, while the continuous phase termed as matrix protects and keeps the reinforcement in place. Depending on geometry, the reinforcing material can be categorized as either particles or fibres. Fibre-reinforced composites are defined by the number of fibre layers as well as the orientation of the fibres, Agarwal et al. (2006).

Composites with reinforcement embedded in matrix, yielding similar properties through the thickness of the geometry, are referred to as single-skin designs. In contrast to single-skin designs, composites also appear in discontinuous constellations with layers of different material.

A sandwich element is defined as a three-layer geometry consisting of two thin faces separated by a thick core, see Figure 2.1.

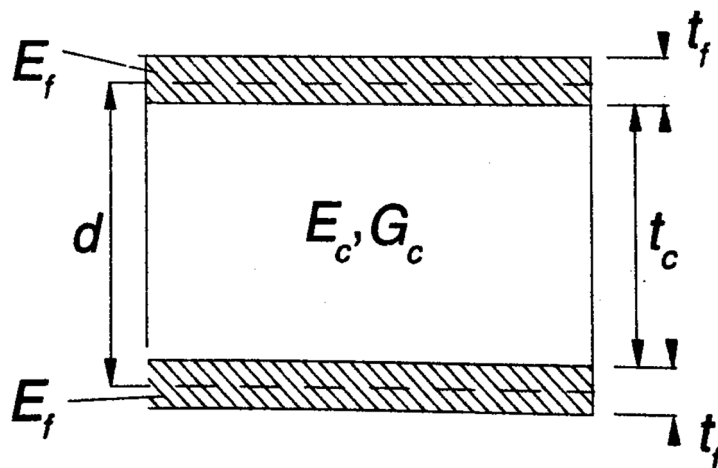


Figure 2.1 Sandwich plate. E is the Young's modulus, G is the shear modulus, t is the thickness and d is the distance between midplanes of the two faces. Core properties are denoted with subscript c and properties of faces are denoted with subscript f , from Zenkert (1997).

The faces most commonly consist of the same stiff and strong material, while the core consists of a light and comparatively weaker material. Both faces and core can be either isotropic material or consist of composite materials with varying properties.

A sandwich element is designed so that the faces consisting of high-performing material are situated as far as possible from the neutral axis and the centre of bending, hence the faces will counteract external bending moments more efficiently. The core stabilizes the faces against buckling and wrinkling, see Chapter 2.3, as well as resists shear, keeping the faces bounded together, Zenkert (1997).

2.2 ULS prediction of composite and sandwich plates

The classical laminate plate theory (CLT), see Reddy (2004), is only valid for thin plates, for which shear deformations can be neglected. This is not the case for sandwich plates, which are usually considered as thick plates, and therefore the shear deformations should be accounted for to capture accurate plate behaviour, see Zenkert (1997). It is the poor shear stiffness of the core material that makes the transverse shear deformations important.

Carrera and Brischetto (2009) presented and assessed a large variety of plate theories for capturing composite and sandwich plate behaviour under bending and vibration. The theories assessed are *Classical laminate theory* (CLT), *First-order shear deformation theory* (FSDT) and *Higher order theories* (HOTs) with refinements including higher order terms in the kinematic assumptions made for the displacements field and by that creating a better representation of deforming sandwich plates. Further, *Layer-wise theories* (LTs), where the number of variables is independent for each layer as well as *Mixed theories* (MTs) including inter-laminar continuity of shear and normal stresses at the interface of two adjacent layers, are assessed.

Carrera and Brischetto (2009) concluded that there are two independent sources of error in the 2D modelling of sandwich structures, one related to length-to-thickness ratio (LTR) and the other related to face-to-core-stiffness ratio (FCSR). For increasing FCSR the kinematics of the two faces become increasingly independent. Errors caused by FCSR cannot be reduced using even HOTs. To increase the accuracy, where FCSR causes errors, LTs analysis becomes necessary. To reduce the errors due to LTR, HOTs can be conveniently used.

For the plates investigated by Carrera and Brischetto (2009) with FCSR in a range of 10^6 - 10^9 , CLT and FSDT are never reliable for thick or moderately thick plates. For thin or very thin plates, accuracy of results is very much subordinated to the FCSR. It was concluded that “CLT and FSDT are not suitable for application to sandwich plates, even when very thin plates are considered”, Carrera and Brischetto (2009).

Compared to HOTs, FSDT is relatively simple to apply to semi-analytical methods for predicting post-buckling response of composite plates, as it was done in work by Yang (2014). Several material degradation models have been investigated by this author to obtain an estimation of the ultimate strength. It was shown that a ply region degradation model based on the FSDT assumptions yields accurate results for thicker plates, while the strength estimations for thinner plates are underestimated. Yang’s suggestion for future work is to implement his semi-analytical tool and degradation model into PULS. He also suggests extending his methods to ultimate strength analysis of sandwich plates.

The key factor when FSDT is applied is the determination of the transverse shear correction factor (K) that will yield accurate results and give good representation of the

plate's behaviour. K is used to compensate for the FSDT assumption that the transverse shear strains are constant through the plate thickness. A generally proposed value of the shear correction factor for single-skin layups is $5/6$, Agarwal et al. (2006).

Birman and Bert (2002) discussed the importance of the shear correction factor (K) for sandwich structures and how to evaluate it. Six methods for the estimation of K for sandwich structures have been compared. These methods are based on:

1. the comparison of natural frequencies,
2. the comparison of average stresses throughout the cross section,
3. the minimization of the quadratic error of the shear stress,
4. modelling the sandwich structure as a discrete mass system,
5. the comparison of the shear strain energies and
6. the comparison of the average strains.

Methods 1-3 yield $K = 1$. Method 4 yields $K = 1$ for sandwich plates with very thin faces only. If the thicknesses of the core and faces are in the same order, values of the shear correction factor are even larger than 1. Methods 5 and 6 give an estimate of K as a function of the stiffness and geometry. Both methods 5 and 6 yield low values of K if the shear stiffness of the core is low compared to the shear stiffness of the faces, which is usually the case for sandwich structures.

Structures, in this case plates, are seldom perfect and usually have small initial geometrical imperfections. In a post-buckling analysis it is important to include initial imperfections as the load-carrying capacity may be greatly overestimated when starting out with a "perfect" structure, Bathe (1996). According to Bathe (1996) the lowest calculated buckling load may be a reasonable estimate of the actual collapse load, assuming that pre-buckling displacements are small. Therefore, defining initial imperfections similar to the lowest buckling modes on a "perfect" structure could greatly reduce the load-carrying capacity but also make it much more realistic.

Misirilis (2012) developed an approach for progressive collapse analysis of composite structures based on nonlinear FEA. During development, the effect on compressive strength from boundary conditions, initial imperfections and material configurations were investigated.

In his findings Misirilis (2012) presents the effects and importance of initial geometric imperfection. ULS of composite plates is greatly affected by geometrical initial imperfections when the plate is thick. The effect on ULS from amplitude of the imperfection reduces with the slenderness of the plate. Irrespective of the slenderness, ULS is greatly affected by the shape of the initial imperfection. Like Bathe (1996), Misirilis (2012) concluded that the shape of the first buckling mode is a conservative assumption, but not the most conservative one. The possibility of wrinkling and local instabilities for laminates could cause further reduction of plate strength lower than that of first-buckling mode shape imperfection. Misirilis (2012) also concluded that a simply supported boundary condition is more conservative than a clamped condition, as a clamped condition (and all investigated boundary conditions that constrained unloaded edges) resulted in higher ultimate loads.

The only obtained source with regards to ultimate strength experimental results for sandwich plates was Boyle et al. (2001). Boyle et al. (2001) presented experimental, numerical and analytical results for buckling and post-buckling of orthotropic rectangular sandwich plates with an aspect ratio of 1.33 or 2.0. The plates were made of FRP faces with either an orthotropic balsa wood or isotropic foam core. The

sandwich plates were subjected to uniaxial compression with clamped loaded edges and simply supported unloaded edges. Boyle et al. (2001) concluded that there is good agreement between analytical, numerical and experimental results of the buckling load. Regarding post-buckling behaviour, there is poor agreement between the numerical and experimental results.

2.3 Failure modes

For composites, failure can be initiated in many different ways; often internal material failure occurs long before any changes in behaviour can be observed. Internal failure is initiated through one or several of the following modes, as defined by Agarwal et al. (2006):

1. breaking of fibres,
2. microcracking of the matrix,
3. debonding: separation of fibres from the matrix,
4. delamination: separation of lamina from each other in a laminated composite.

The severity of the failure modes differs greatly from one composite to another, highly dependent on the material composition, reinforcement, geometry, layup and the kind of loading applied to the geometry. Depending on the fibre volume fraction, failure tends to be initiated in different ways for different loads.

For longitudinal tensile loading the most common failure initiation is fibre breakage at the weakest cross section. Composites with fibre volume fraction under 40% exhibit brittle failure, a fibre volume fraction between 40% and 65% yields brittle failure with fibre pullout and a fibre volume fraction over 65% yields brittle failure with fibre pullout and shear failure or debonding, Agarwal et al. (2006).

Subjected to longitudinal compressive loads composites with a fibre volume fraction less than 40% exhibit matrix yield and/or matrix microcracking and debonding of constituents. With a fibre volume fraction over 40% failure is initiated through transverse tensile failure due to Poisson's ratio effects, shear failure or fibre microbuckling. The fibre microbuckling occurs with either matrix still elastic, preceded by matrix yielding or preceded by debonding of constituents, Agarwal et al. (2006).

For composites subjected to transverse tensile loads failure initiation occurs most commonly by matrix tensile failure or debonding combined with the possibility of fibre splitting. Composites subjected to transverse compressive loads exhibit matrix shear failure or matrix shear failure combined with debonding and possibly fibre crushing. Composites under in-plane shear loading fail either by matrix shear failure, debonding or a combination of both, Agarwal et al. (2006).

Due to the differences in composition between sandwich plates and single-skin composites, see Chapter 2.1, sandwich structures can fail in additional ways. The most common failure modes for sandwich plates acting as beam elements are shown in Figure 2.2 when exerted to different loads or load combinations, Zenkert (1997). One can notice that for buckling loads different local buckling instabilities can occur in addition to the global buckling - the instabilities which are of importance in this thesis.

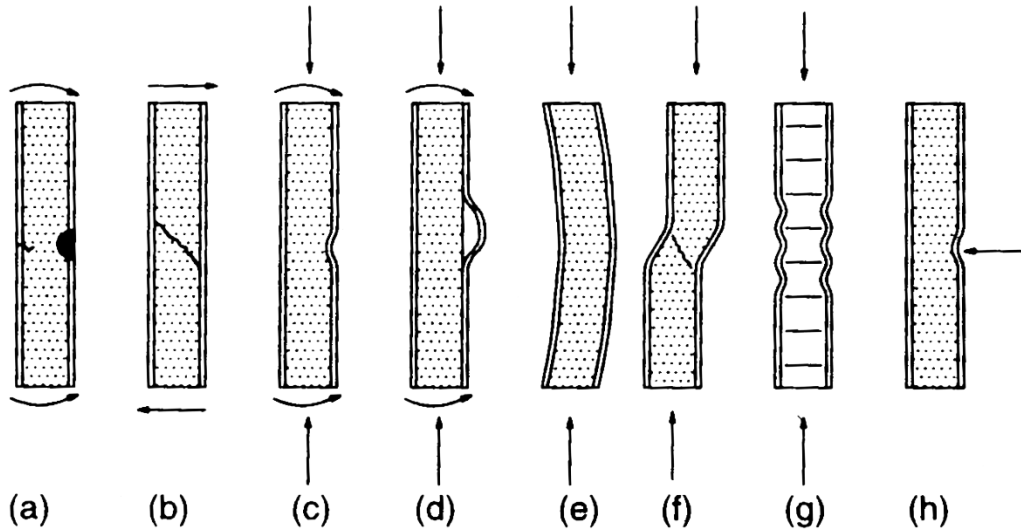


Figure 2.2 Failure modes for sandwich plates acting as beams under different loads. (a) Face yielding under bending, (b) core shear failure under shear loads, (c & d), face wrinkling under compression & bending, (e) general buckling under compression, (f) shear crimping under compression, (g) face dimpling under compression and (h) local indentation due to lateral load, from Zenkert (1997).

2.4 Failure criteria

Local buckling failure criteria for sandwich plates, face wrinkling and shear crimping, are presented in this chapter. Generally used failure criteria for orthotropic/composite materials, the Hashin-Rotem and the Hashin failure criteria, are briefly described here as well.

2.4.1 Face wrinkling

Several different expressions for the face wrinkling, local instability as seen in Figure 2.2d, can be found in literature. The one presented by Harris and Crisman (1965) includes amplitude of initial waviness and distinguishes between core tension, core compression and core shear failure. It can be applied to orthotropic material facings under uniaxial compression. A similar yet simpler and more conservative expression for the face wrinkling critical stress was proposed by Zenkert (1997). It states that face wrinkling will occur when the compressive stress in face reaches the critical wrinkling stress, defined as:

$$\sigma_{f,cr,x} = 0.5 \sqrt[3]{E_{fx} E_{cx} G_{cx}} \quad [\text{MPa}] \quad (2.1a)$$

$$\sigma_{f,cr,y} = 0.5 \sqrt[3]{E_{fy} E_{cy} G_{cy}} \quad [\text{MPa}] \quad (2.1b)$$

More detailed formulae for the biaxial loading case can be found in literature, but according to experimental work presented in Allen (1969), Equations (2.1a) and (2.1b) give good predictions and are on the conservative side. For combined loading cases Sullins et al. (1969) suggested that the following interaction equation should be used:

$$\left(\frac{\sigma_{f,1}}{\sigma_{f,cr,x}} \right)^3 + \left(\frac{\sigma_{f,2}}{\sigma_{f,cr,y}} \right) = 1 \quad (2.2)$$

where $\sigma_{f,1}$ and $\sigma_{f,2}$ are the major and minor principal compressive stresses in the faces defined as:

$$\sigma_{f,1,2} = \frac{\sigma_{f,x} + \sigma_{f,y}}{2} \pm \left[\left(\frac{\sigma_{f,x} - \sigma_{f,y}}{2} \right)^2 + \tau_{f,xy}^2 \right]^{0.5} \quad [\text{MPa}] \quad (2.3)$$

2.4.2 Shear crimping

The core thickness and shear modulus must be adequate to prevent the shear failure in the core under compressive loads as it can be seen in Figure 2.2(f). The described local instability is known as shear crimping. Zenkert (1997) proposed a simple expression for the shear crimping critical stress, which can be expressed as:

$$\sigma_{f,cr} = \frac{S}{2t_f} \quad [\text{MPa}] \quad (2.4)$$

where S is the shear stiffness of sandwich plate, which will be later described in Chapter 3.3.

2.4.3 Hashin-Rotem and Hashin failure criteria

The Hashin-Rotem failure criterion, see Hashin (1973), and the Hashin failure criterion, see Hashin (1980), are based on experimentally observed failures for different loading conditions. Both are mode-dependent, i.e. different failure modes are being distinguished.

The expressions for the Hashin-Rotem failure are rather simple and only in-plane stress contributions are taken into the consideration. In addition, the Hashin failure criteria include interlaminar stresses, i.e. out-of-plane normal and shear stress contributions.

Failure in fibre tension

Hashin-Rotem criterion:

$$\left(\frac{\sigma_{11}}{X_T} \right)^2 = 1 \quad (2.5a)$$

Hashin criterion:

$$\left(\frac{\sigma_{11}}{X_T} \right)^2 + \left(\frac{\tau_{12}^2 + \tau_{13}^2}{S_{12}S_{13}} \right) = 1 \quad (2.5b)$$

Failure in fibre compression

Hashin-Rotem and Hashin criterion:

$$\left(\frac{\sigma_{11}}{X_C} \right)^2 = 1 \quad (2.6)$$

Failure in matrix tension

Hashin-Rotem criterion:

$$\left(\frac{\sigma_{22}}{Y_T}\right)^2 + \left(\frac{\tau_{12}}{S_{12}}\right)^2 = 1 \quad (2.7a)$$

Hashin criterion:

$$\frac{(\sigma_{22} + \sigma_{33})^2}{Y_T Z_T} + \frac{\tau_{23}^2 - \sigma_{22} \sigma_{33}}{S_{23}^2} + \frac{\tau_{12}^2 + \tau_{13}^2}{S_{12} S_{13}} = 1 \quad (2.7b)$$

Failure in matrix compression

Hashin-Rotem criterion:

$$\left(\frac{\sigma_{22}}{Y_C}\right)^2 + \left(\frac{\tau_{12}}{S_{12}}\right)^2 = 1 \quad (2.8a)$$

Hashin criterion:

$$\left(\frac{Y_C Z_C}{2S_{23}^2} - 1\right) \left(\frac{\sigma_{22}}{Y_C} + \frac{\sigma_{33}}{Z_C}\right) + \left(\frac{\sigma_{22} + \sigma_{33}}{2S_{23}}\right)^2 + \frac{\tau_{23}^2 - \sigma_{22} \sigma_{33}}{S_{23}^2} + \frac{\tau_{12}^2 + \tau_{13}^2}{S_{12} S_{13}} = 1 \quad (2.8b)$$

According to Agarwal et al. (2006), the interlaminar stresses are negligible in the regions away from the free boundary, i.e. free edges, holes, and joints, etc. If neglected the described failure criteria are then almost the same, only the expression for fibre failure in tension differs.

2.5 The PULS and Composite PULS codes

Panel Ultimate Limit State (PULS) is a semi-analytical calculation tool used for the ultimate capacity prediction by estimating non-linear buckling response developed by DNV GL. Only a brief description of the methods behind the PULS and Composite PULS codes are presented here; more thorough descriptions can be found in works by Byklum and Amdahl (2002), Byklum (2002), Steen and Byklum (2005) and Steen et al. (2004).

The PULS code was first developed for unstiffened, regularly and non-regularly stiffened and corrugated steel plates under uniaxial or biaxial compressive, tensile, shear and/or out-of-plane loads. It is limited to simply supported rectangular non-curved plates. Clamped plates can be modelled by adding springs to the plate edges with the risk of obtaining inaccurate results if spring stiffness is poorly estimated. PULS was extended to Composite PULS for the ULS prediction of unstiffened composite panels, see Braaten and Boström (2013).

The PULS and Composite PULS codes are written in Fortran 95 programming language and use MS Excel user-interface, which makes them both computationally efficient and user friendly. The PULS and Composite PULS codes are based on CLT, i.e. the Kirchhoff's plate assumptions. To capture the non-linear post-buckling response of plates, the large deflection plate theory, to account for initial imperfections w_{init} , is implemented. The initial imperfection is set to take the shape of the first buckling mode, while the amplitude of the imperfection can be selected (e.g. $w_{0,init} = b/1000$).

Energy methods, see Appendix D, are used to describe the non-linear plate response due to the large deformation theory in the PULS and Composite PULS codes. Using the principle of minimum potential energy a set of non-linear equilibrium equations is developed, which can be solved by using the Rayleigh-Ritz method, see Appendix E.

If assuming CLT, as for the PULS and Composite PULS codes, the total potential energy is expressed only by the mid-plane deflection w , which is approximated by using a series of admissible functions together with unknown amplitudes. It is more favourable to express the potential energy with as few approximated functions as possible. Adding more functions results in more terms and consequently in a higher computational cost, as explained in Braaten and Boström (2013).

The extensional and shear stiffness coupling contributions, i.e. terms A_{16} and A_{26} of the extensional stiffness matrix, as defined in Appendix C, are not implemented in the Composite PULS code. This simplification is reasonable, since there is no such coupling if cross-ply layups are used. According to Agarwal (2006), for cross-ply layups \bar{Q}_{16} and \bar{Q}_{26} terms will cancel each other out if there is an equal number of plies orientated at a positive and negative ply orientation angle θ and having the same thickness. Positions of these plies in such laminates are irrelevant.

Based on findings by Ashton (1969), additional simplification to not implement D_{16} and D_{26} terms of the bending stiffness matrix, as defined in Appendix C, was made in the Composite PULS code. For a general case there is a coupling between in-plane stresses and shear strains and these terms should be included, as mentioned by Hareide (2014). Therefore, terms D_{16} and D_{26} are not to be neglected especially if layups that include plies with $+45^\circ/-45^\circ$ orientations are being investigated.

Stresses and displacement field are obtained in the PULS and Composite PULS codes using the Airy's stress function F , after which different failure criteria can be evaluated. For the PULS code, the von Mises yield criterion is evaluated, while for the Composite PULS code the Hashin-Rotem failure criterion is implemented, see Braaten and Boström (2013).

A complete degradation model with instantaneous degradation was implemented in the Composite PULS code. Symmetrical ply degradation was assumed in order to keep the model conservative and because the PULS code cannot capture asymmetry (i.e. $[B] = 0$ or no coupling between strain and curvature is assumed). The implemented degradation model was not fully validated and is not included. Only the first buckling load and the Tsai-Wu failure criterion for FPF are being evaluated in the Composite PULS code.

3 Sandwich PULS

In this chapter, the further development of the PULS and Composite PULS codes is presented. The new code is called Sandwich PULS. The main change compared to the other two codes is the implementation of first-order shear deformation plate theory (FSDT), which relaxes some assumptions of the Kirchhoff's classical laminate plate theory (CLT).

FSDT has been assumed even though HOTs would be preferred, as concluded by Carrera and Brischetto (2009). Since one of the objectives of this thesis is that Sandwich PULS should remain a computational tool with a low computational cost, it is believed that implementation of HOTs would have made computational costs too high. Even the implementation of FSDT could have a high computational cost as it was implied from work done by Yang (2014).

Changes needed for this and implementations to the existing Composite PULS code are briefly presented and highlighted in equations with dashed lines. Full derivations and a more thorough explanation of theories implemented in Sandwich PULS can be found in appendices as referred to in the text. General differences between the PULS, Composite PULS and Sandwich PULS codes are presented in Table 3.1.

Table 3.1 General differences between the PULS, Composite PULS and Sandwich PULS codes.

	PULS	Composite PULS	Sandwich PULS
Panel type	Steel or aluminium	Single-skin	Sandwich/ Multiple materials
Plate theory	CLT	CLT	FSDT
Geometries	Rectangular, non-curved	Rectangular, non-curved, unstiffened, symmetrical layup	
BCs	Simply supported, "clamped"	Simply supported	
ULS	Ultimate strength	FPF/FFF/LPF	FPF/FW/SC
Failure criteria	von Mises	Hashin-Rotem/ Tsai-Wu	Hashin-Rotem/ FW/FC

The plate schematic geometry is presented in Figure 3.1 where notations used in this chapter are indicated and described.

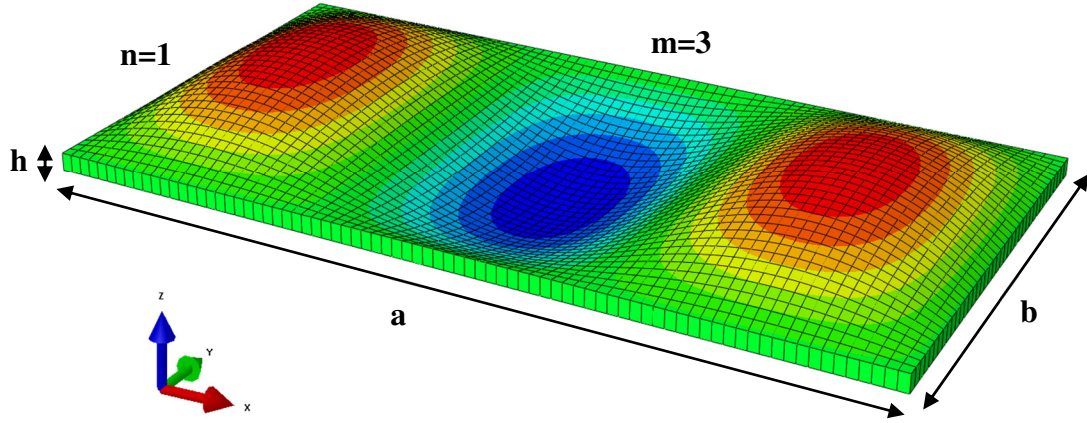


Figure 3.1 Plate geometry where a is the length, b is the breadth, h is the thickness, m is the number of buckling half-sine waves along the longitudinal direction and n is the number of buckling half-sine waves along the transverse direction.

3.1 Kinematics and displacement field

Composite PULS uses Kirchhoff's assumptions, which are valid for thin plates only. For thick plates and plates where shear deformations are not to be neglected, i.e. for sandwich plates, first-order shear deformation theory (FSDT) needs to be implemented in Sandwich PULS under the assumptions presented in Appendix B.

Since the PULS and Composite PULS codes are based on the large deflection plate theory, the non-linear terms are added to the membrane strain in order to acquire better approximation for the deflections that are large compared to the plate thickness. Due to the implementation of FSDT the bending strains are dependent not only on the derivative of the deflection, but also on the shear strains. The following extended strain field is then defined as:

$$\varepsilon_x = \varepsilon_x^0 + zk_x = \left(\frac{\partial u_0}{\partial x} + \frac{1}{2} \left(\frac{\partial w}{\partial x} \right)^2 + \frac{\partial w_{init}}{\partial x} \frac{\partial w}{\partial x} \right) + z \left(\frac{\partial \phi_x}{\partial x} \right) \quad [-] \quad (3.1a)$$

$$\varepsilon_y = \varepsilon_y^0 + zk_y = \left(\frac{\partial v_0}{\partial y} + \frac{1}{2} \left(\frac{\partial w}{\partial y} \right)^2 + \frac{\partial w_{init}}{\partial y} \frac{\partial w}{\partial y} \right) + z \left(\frac{\partial \phi_y}{\partial y} \right) \quad [-] \quad (3.1b)$$

$$\begin{aligned} \gamma_{xy} &= \gamma_{xy}^0 + zk_{xy} = \\ &= \left(\frac{\partial u_0}{\partial y} + \frac{\partial v_0}{\partial x} + \frac{\partial w}{\partial x} \frac{\partial w}{\partial y} + \frac{\partial w_{init}}{\partial x} \frac{\partial w}{\partial y} + \frac{\partial w_{init}}{\partial y} \frac{\partial w}{\partial x} \right) + z \left(\frac{\partial \phi_x}{\partial y} + \frac{\partial \phi_y}{\partial x} \right) \quad [-] \quad (3.1c) \end{aligned}$$

$$\gamma_{xz} = \frac{\partial w}{\partial x} + \phi_x \quad [-] \quad (3.1d)$$

$$\gamma_{yz} = \frac{\partial w}{\partial y} + \phi_y \quad [-] \quad (3.1e)$$

Displacement functions are represented in the form of truncated, i.e. finite number of approximation terms, double Fourier series as:

$$w = \sum_{m=1}^M \sum_{n=1}^N A_{mn} \sin \frac{m\pi x}{a} \sin \frac{n\pi y}{b} \quad [\text{mm}] \quad (3.2a)$$

$$\gamma_{xz} = \sum_{m=1}^M \sum_{n=1}^N B_{mn} \cos \frac{m\pi x}{a} \sin \frac{n\pi y}{b} \quad [-] \quad (3.2b)$$

$$\gamma_{yz} = \sum_{m=1}^M \sum_{n=1}^N C_{mn} \sin \frac{m\pi x}{a} \cos \frac{n\pi y}{b} \quad [-] \quad (3.2c)$$

where M and N are the numbers of degrees of freedom used in the Rayleigh-Ritz approximation method, see Appendix E.

There is no coupling between the membrane and the bending strains for symmetric layups. Therefore there is no need for implementation of the in-plane displacement fields, u and v , and only the three displacement functions, shown in Equations (3.2a), (3.2b) and (3.2c), are used to describe the buckling problem when FSDT is applied.

3.2 Energy contributions

The principle of minimum potential energy is reformulated using the Rayleigh-Ritz method in order to solve the buckling problem. Total potential energy consists of separate energy contributions from in-plane (U_p) and shear strains (U_s) and energy contribution from external forces (W) as:

$$\Pi = U_p + U_s + W \quad [\text{Nmm}] \quad (3.3)$$

The in-plane strain energy contribution can be further divided into three contributions associated, respectively, with the membrane strain energy U_m , the bending strain energy U_b and the strain energy U_{mb} due to bending-stretching coupling, as can be seen in Equation (3.4). The latter is non-zero only for non-symmetric plates, which are not within the scope of this thesis.

$$\begin{aligned} U_p &= \frac{1}{2} \int_V \{\boldsymbol{\varepsilon}\}^T \{\boldsymbol{\sigma}\} dV = \frac{1}{2} \int_A \int_{-h/2}^{h/2} \{\boldsymbol{\varepsilon}\}^T [\bar{Q}] \{\boldsymbol{\varepsilon}\} dz dA = \\ &= \frac{1}{2} \int_A \left[\{\boldsymbol{\varepsilon}^0\}^T [A] \{\boldsymbol{\varepsilon}^0\} + 2\{\boldsymbol{\varepsilon}^0\}^T [B] \{k\} + \{k\}^T [D] \{k\} \right] dA = \quad [\text{Nmm}] \quad (3.4) \\ &= U_m + U_{mb} + U_b \end{aligned}$$

The implementation of FSDT into the Sandwich PULS code only influences the energy contribution from the bending strains, since they are dependent on the curvatures, which are further based on the FSDT assumptions, see Equation (B.5). The energy contribution from the membrane strains and the potential from external loads are not dependent on the implemented FSDT and is therefore kept unaltered, as presented in Byklum (2002). As presented in Chapter 2.5, terms D_{16} and D_{26} of the bending stiffness matrix should be accounted for and are implemented in the Sandwich PULS code.

The expanded bending strain energy contribution is expressed as:

$$\begin{aligned}
U_b &= \frac{1}{2} \int_A \{\kappa\}^T [D] \{\kappa\} dA = \\
&= \frac{1}{2} \int_0^a \int_0^b \left[D_{11} (k_x)^2 + 2D_{12} k_x k_y + D_{22} (k_y)^2 + 2D_{16} k_x k_{xy} + \right. \\
&\quad \left. + 2D_{26} k_y k_{xy} + D_{66} (k_{xy})^2 \right] dx dy \\
&= \frac{1}{2} \int_0^a \int_0^b \left[D_{11} \left(\frac{\partial^2 w}{\partial x^2} - \frac{\partial \gamma_{xz}}{\partial x} \right)^2 + D_{22} \left(\frac{\partial^2 w}{\partial y^2} - \frac{\partial \gamma_{yz}}{\partial y} \right)^2 + \right. \\
&\quad + 2D_{12} \left(\frac{\partial^2 w}{\partial x^2} - \frac{\partial \gamma_{xz}}{\partial x} \right) \left(\frac{\partial^2 w}{\partial y^2} - \frac{\partial \gamma_{yz}}{\partial y} \right) + \quad [\text{Nmm}] \quad (3.5) \\
&\quad + 2D_{16} \left(\frac{\partial^2 w}{\partial x^2} - \frac{\partial \gamma_{xz}}{\partial x} \right) \left(2 \frac{\partial^2 w}{\partial x \partial y} - \frac{\partial \gamma_{xz}}{\partial y} - \frac{\partial \gamma_{yz}}{\partial x} \right) + \\
&\quad + 2D_{26} \left(\frac{\partial^2 w}{\partial y^2} - \frac{\partial \gamma_{yz}}{\partial y} \right) \left(2 \frac{\partial^2 w}{\partial x \partial y} - \frac{\partial \gamma_{xz}}{\partial y} - \frac{\partial \gamma_{yz}}{\partial x} \right) + \\
&\quad \left. + D_{66} \left(2 \frac{\partial^2 w}{\partial x \partial y} - \frac{\partial \gamma_{xz}}{\partial y} - \frac{\partial \gamma_{yz}}{\partial x} \right)^2 \right] dx dy
\end{aligned}$$

The shear strains are neglected in the Composite PULS code since CLT was assumed. If FSDT is assumed, the shear strain contribution to the total potential energy has to be implemented. It can be expressed as:

$$\begin{aligned}
U_s &= \frac{1}{2} \int_V \{\gamma_s\}^T \{\sigma_s\} dV = \\
&= \frac{1}{2} \int_{-h/2}^{h/2} \int_A \{\gamma_s\}^T [\bar{Q}_s] \{\gamma_s\} dz dA = \\
&= \frac{1}{2} \int_A \{\gamma_s\}^T [A_s] \{\gamma_s\} dA = \quad [\text{Nmm}] \quad (3.6) \\
&= \frac{1}{2} \int_A \left[A_{44} (\gamma_{yz})^2 + 2A_{45} \gamma_{xz} \gamma_{yz} + A_{55} (\gamma_{xz})^2 \right] dz dA
\end{aligned}$$

Full derivations of the bending and shear strain energy contributions after the Rayleigh-Ritz method is applied are shown in Appendix E.

3.3 Shear stiffness implementation

As mentioned in Chapter 2.2 the shear correction factor (K) has to be used to compensate for the FSDT assumption that the transverse shear strains are constant through the plate thickness. In Sandwich PULS shear correction is accounted for and implemented inside of the transverse shear stiffness matrix $[A_s]$ calculation, i.e. inside terms A_{44} , A_{45} and A_{55} .

Dependent on the type of plate being analysed in Sandwich PULS, a different shear correction approach is used. For a general single-skin orthotropic plate this is done by applying the shear correction factor K to the shear stiffness matrix as:

$$[A_s] = K[A'_s] = \frac{5}{6}[A'_s] \quad [\text{N/mm}] \quad (3.7a)$$

where $K = 5/6$ is a general valid and accepted value for orthotropic plates, see Agarwal et al. (2006).

For a sandwich plate the method presented by Birman and Bert (2002), which is based on the comparison of the shear strain energies, is used to evaluate the shear correction factor. If the sandwich core has low stiffness, both axial and shear, compared to the stiffness of the faces, the shear stiffness matrix can then be obtained as:

$$[A_s] = K[A'_s] = 2.35 \frac{G_c}{G_f} [A'_s] \quad [\text{N/mm}] \quad (3.7b)$$

Two different options for sandwich plates to compensate for the assumption of constant shear stress through the thickness are presented in Zenkert (1997). Both options assume that a sandwich plate has thin faces, i.e. $t_f \ll t_c$, weak core, i.e. $E_f \gg E_c$, and that the shear moduli G_f of the faces are large. An assumption that $A_{45} = A_{54} = 0$ can also be made since most core materials are at least orthotropic (for example balsa, honeycombs) or even isotropic (for example most foams). For an isotropic core the terms A_{44} and A_{55} are equal and Zenkert (1997) proposes two options for how to obtain them:

$$A_{44} = A_{55} = G_c t_c \quad [\text{N/mm}] \quad (3.7c)$$

$$A_{44} = A_{55} = \frac{G_c d^2}{t_c} \quad [\text{N/mm}] \quad (3.7d)$$

All four options for the shear stiffness evaluation are implemented in the Sandwich PULS code. Results from sensitivity studies dependent on these options are presented in Chapter 5, where the options are denoted as:

- Kopt1: shear stiffness evaluated using Equation (3.7c),
- Kopt2: shear stiffness evaluated using Equation (3.7d),
- Kopt3: shear stiffness evaluated using Equation (3.7b),
- K=5/6: shear stiffness evaluated using Equation (3.7a).

3.4 Solution procedure

A presentation of the solution procedure that is used in the Sandwich PULS code follows the methodology of this thesis, as presented in Chapter 1.3. First, the procedure for solving the eigenvalue problem is presented, which is to be used for defining the imperfection shape and represents one of the ULS loads, see DNV (2013). The incremental solution procedure, which is needed for capturing the buckling and post-buckling behaviour of the plate, is presented next. The procedure to obtain the failure initiation load is presented last.

The eigenvalue analysis and the incremental solution method are completely separated calculation processes in the PULS codes, even though almost the same theoretical principles and similar problem formulations apply for both. Because of that, the

implementations of the FSDT in the eigenvalue analysis and the load-displacement analysis are presented in separate sections.

Only parts that have been changed in the solution procedure due to the implementation of FSDT are presented in this chapter. Further and more detailed descriptions of the procedure can be found in Yang (2014), Byklum (2002) and Steen (1998).

3.4.1 Eigenvalue analysis

The eigenvalue, i.e. first critical buckling load, is obtained after solving the following system of equations written in a general matrix form:

$$([K^M] - \Lambda[K^G])\{A\} = \{0\} \quad (3.8)$$

where $[K^M]$ is the material stiffness matrix, $[K^G]$ is the geometric stiffness matrix, Λ is the eigenvalue and $\{A\}$ is the corresponding eigenvector.

The displacement field corresponding to FSDT, shown in equation (3.2), has 3 displacements: the out-of-plane displacement and the additional shear strains. The displacement vector corresponding to the eigenvalue and to the assumed displacement field can be written as:

$$\{A\} = \begin{Bmatrix} A_{ij} \\ \vdots \\ A_{MN} \\ B_{ij} \\ \vdots \\ B_{MN} \\ C_{ij} \\ \vdots \\ C_{MN} \end{Bmatrix} = \begin{Bmatrix} \{A\} \\ \{B\} \\ \{C\} \end{Bmatrix} \quad [\text{mm or -}] \quad (3.9)$$

Due to the expanded displacement field, the material and geometric stiffness matrices are 9-times larger. The material stiffness matrix is obtained after the in-plane strain energy contribution is derived twice with respect to the displacement amplitudes, as shown in Equation (3.10).

$$[K^M] = \begin{bmatrix} \frac{\partial^2 U}{\partial A_{ij} \partial A_{kl}} & \frac{\partial^2 U}{\partial A_{ij} \partial B_{kl}} & \frac{\partial^2 U}{\partial A_{ij} \partial C_{kl}} \\ \frac{\partial^2 U}{\partial B_{ij} \partial A_{kl}} & \frac{\partial^2 U}{\partial B_{ij} \partial B_{kl}} & \frac{\partial^2 U}{\partial B_{ij} \partial C_{kl}} \\ \frac{\partial^2 U}{\partial C_{ij} \partial A_{kl}} & \frac{\partial^2 U}{\partial C_{ij} \partial B_{kl}} & \frac{\partial^2 U}{\partial C_{ij} \partial C_{kl}} \end{bmatrix} \quad [\text{N/mm or N or Nmm}] \quad (3.10)$$

In a similar manner, the geometric stiffness matrix is obtained. It should, however, be noted that the geometric stiffness matrix is not dependent on the implementation of FSDT. The matrix is expanded with terms equal to zero in order to match the material stiffness matrix dimensions, since the external load potential is dependent only on the out-of-plane displacement.

The exact size of the stiffness matrices, i.e. the exact size of the eigenvalue system of equations, depends on the chosen number of terms, i.e. degrees of freedom, for the Rayleigh-Ritz trial functions, see Appendix E.

Derived final expressions for the stiffness sub-matrices are shown in Appendix F and are implemented in the Sandwich PULS code. The material and geometric stiffness matrices are evaluated and sent to the eigenvalue solver, which is a built-in Fortran subroutine. As a result, the eigenvalue for a certain loading case is obtained.

3.4.2 Incremental solution method

The perturbation incremental method, see Steen (1998), is applied to predict pre- and post-buckling behaviour in the PULS codes. This method makes it possible to solve the non-linear plate equilibrium equations in increments by computing the rate form of these equations with respect to the perturbation parameter. The latter one is varied from 0 to 1 within each stage, which makes the load path piecewise linear. If the perturbation parameter is sufficiently small, i.e. if a sufficiently large number of load stages is used, any load history can be approximated by using this procedure, Steen (1998).

If the arc length parameter $\Delta\eta$ is used as the perturbation parameter, the relation linking the change in the arc length parameter with a change of the external load and a change of displacement and shear strains, must be satisfied:

$$\Delta\Lambda^2 + \Delta q_{mn}^2 = \Delta\eta^2 \quad [-] \quad (3.11)$$

As mentioned, here q_{mn} are not only the displacement amplitudes, i.e. A_{mn} , as in the PULS and Composite PULS codes, but also the shear strain amplitudes, i.e. B_{mn} and C_{mn} , since FSDT is applied. The displacement amplitudes are to be made non-dimensional with respect to the plate thickness as:

$$q_{mn} = \frac{A_{mn}}{t} \quad [-] \quad (3.12)$$

As the increment size goes towards zero, the relation is found by combining Equation (3.11) and Equation (3.12) and thus arriving at:

$$\dot{\Lambda}^2 + \sum_w \frac{\dot{A}_{mn}^2}{t^2} + \sum_{\gamma_{xz}} \dot{B}_{mn}^2 + \sum_{\gamma_{yz}} \dot{C}_{mn}^2 = 1 \quad [-] \quad (3.13)$$

3.4.3 Procedure for solving incremental equations

Here the procedure for solving the first-order incremental equations is briefly described, based on the work done by Yang (2014). First, incremental equilibrium equations need to be established in a similar manner as for the eigenvalue analysis. The principle of minimum total potential energy should be written in the rate form as:

$$\begin{bmatrix} \frac{\partial^2 \Pi}{\partial A_{mn} \partial A_{pq}} & \frac{\partial^2 \Pi}{\partial A_{mn} \partial B_{pq}} & \frac{\partial^2 \Pi}{\partial A_{mn} \partial C_{pq}} \\ \frac{\partial^2 \Pi}{\partial B_{mn} \partial A_{kl}} & \frac{\partial^2 \Pi}{\partial B_{mn} \partial B_{pq}} & \frac{\partial^2 \Pi}{\partial B_{mn} \partial C_{pq}} \\ \frac{\partial^2 \Pi}{\partial C_{mn} \partial A_{kl}} & \frac{\partial^2 \Pi}{\partial C_{mn} \partial B_{pq}} & \frac{\partial^2 \Pi}{\partial C_{mn} \partial C_{pq}} \end{bmatrix} \cdot \begin{Bmatrix} \dot{A}_{mn} \\ \dot{B}_{mn} \\ \dot{C}_{mn} \end{Bmatrix} + \begin{bmatrix} \frac{\partial^2 \Pi}{\partial A_{mn} \partial \Lambda} \\ \frac{\partial^2 \Pi}{\partial B_{mn} \partial \Lambda} \\ \frac{\partial^2 \Pi}{\partial C_{mn} \partial \Lambda} \end{bmatrix} \cdot \dot{\Lambda} = \{0\} \quad (3.14)$$

Or rewritten as:

$$[K]\{\dot{A}_{mn}\} + \{G\}\dot{\Lambda} = \{0\} \quad (3.15)$$

where $[K]$ is the incremental stiffness matrix, $\{G\}$ is the incremental load vector and $\dot{\Lambda}$ is the rate of load parameter.

The incremental stiffness matrix can be rewritten as:

$$[K] = \begin{bmatrix} [K_{AA}] & [K_{AB}] & [K_{AC}] \\ [K_{BA}] & [K_{BB}] & [K_{BC}] \\ [K_{CA}] & [K_{CB}] & [K_{CC}] \end{bmatrix} \quad [\text{N/mm}] \quad (3.16)$$

All implementations are based on the conclusions made and discussed in Chapter 3.2 when explaining the potential energy contributions.

Due to the relaxed in-plane rotation assumptions of FSDT, the incremental stiffness submatrices are dependent on the energy contribution from the bending strains, which are redefined as shown in Equation (3.5). The energy contribution from shear strains, which are redefined as shown in Equation (3.6), is included in the $[K_{BB}]$ and $[K_{CC}]$ submatrices. The membrane strains and the external load potential only influence the $[K_{AA}]$ sub-matrix, which has not been affected by the implementation of FSDT. Derived expressions for the bending and shear strain-based stiffness matrices are shown in Appendix F.

With FSDT applied, the system of $(3 \cdot M \cdot N)$ equations, see Equation (3.14), has $(3 \cdot M \cdot N + 1)$ unknowns. An equal number of terms is assumed for the three displacement fields, i.e. $DOF = M \cdot N$ for each displacement or shear strain. DOF along the shorter plate edge, i.e. N , is set manually, while DOF along the longer plate edge is dependent of the plate aspect ratio, i.e. $M = a/b \cdot N$.

The last equation needed to solve the linear system of equations is Equation (3.13) that has been previously extended due to the implemented FSDT. After Equation (3.15) is inserted into Equation (3.13) the arc length increment $\dot{\Lambda}$ can be obtained as:

$$\dot{\Lambda} = \pm \frac{t}{\sqrt{t^2 + \sum_w ([K]^{-1}\{G\})^2 + t^2 \sum_\gamma ([K]^{-1}\{G\})^2}} \quad [-] \quad (3.17)$$

One should observe that the additional summation over shear strains term is present in (3.17) due to the implementation of FSDT.

The load parameter and the displacement and shear strain amplitudes for the next stage are calculated as:

$$A_{mn}^{(s+1)} = A_{mn}^{(s)} + \Delta\eta \frac{\partial A_{mn}^{(s)}}{\partial \eta} \quad [\text{mm or -}] \quad (3.18a)$$

$$\Lambda^{(s+1)} = \Lambda^{(s)} + \Delta\eta \frac{\partial \Lambda^{(s)}}{\partial \eta} \quad [\text{mm}] \quad (3.18b)$$

Equations (3.18a) and (3.18b) can be written in the expanded Taylor series form, but if a small increment size is used it is enough to take only the linear terms and still keep sufficient accuracy. Using the second and higher order terms will only increase computational cost, as concluded in Byklum (2002). Due to this simplification, the estimated deflections are smaller than the real ones for all PULS codes, if a small

enough increment size is not used. This effect becomes more significant in the areas where change in deflection is large, i.e. where the non-linear Taylor series terms become non-negligible.

3.4.4 Failure initiation

The incremental procedure is stopped when a given failure criterion is reached. Since sandwich plates are in the scope of this thesis, the face wrinkling (see Chapter 2.4.1) and the shear crimping (see Chapter 2.4.2) local instability failure criteria have been implemented in the Sandwich PULS code. The Hashin-Rotem failure criterion (see Chapter 2.4.3) was already implemented in the Composite PULS code and can be evaluated in the Sandwich PULS code as well.

To satisfy sufficient accuracy in the PULS codes when close to failure, the increment parameter $\Delta\eta$ is made smaller until stress from the applied external loads is within 1% of the failure stress.

4 Finite element analysis

This chapter presents the FE model and analyses used to compare and validate the PULS, Composite PULS and Sandwich PULS codes. All models and analyses were made in the FE software Abaqus/Standard, see Dassault Systèmes (2014).

4.1 Model set up

All geometries, in this study all rectangular plates, were modelled as two-dimensional deformable planar shell elements. In order to define the composite materials, the composite-layup tool in Abaqus was used. To analyse the different loading cases, uniaxial, biaxial and axial/shear loading, two different set ups were used. All plates were simply supported for all loading conditions and for details about boundary conditions and model set-up see Chapter 4.2.

All plates were modelled using conventional shell elements with both displacement and rotational degrees of freedom. Element types supported for analysis of laminated composite plates are based on first-order shear flexible theory. In this theory the transverse shear strain is assumed to be constant through the thickness of the shell. In order to estimate interlaminar shear stresses the shear correction factor was derived in Abaqus from the distribution of transverse shear stresses, see Dassault Systèmes (2014). To obtain interlaminar stresses, the shell was numerically integrated during analysis using Simpson's rule allowing integration points at the interface of two layers. Three integration points were defined through the thickness for each layer, at the top, in the middle and at the bottom.

To investigate the validity of the shell theory, i.e. if the assumption that plane sections remain plane is satisfied, Equation (4.1) where the left side is the material, a slenderness ratio was used.

$$\frac{K_{\alpha\alpha} l^2}{D_{(\alpha+3)(\alpha+3)}} \geq 100 \quad [-] \quad (4.1)$$

K_{ij} is the shear stiffness, D_{ij} is the section stiffness and l is a characteristic length on the surface of the shell. If the expression in Equation (4.1) is satisfied, the shell theory is sufficient. If the expression is not satisfied, membrane strains will not vary linearly through the section and shell theory might give inaccurate results. The shear stiffness, K_{ij} , and section stiffness, D_{ij} , were obtained from the Abaqus data file *filename.dat* after running a data check of the analysis with defined pre-processor output. All plates used in the study, see Appendix A, fulfilled the expression in Equation (4.1), hence the shell theory is valid.

4.2 Load cases and boundary conditions

In this section the boundary conditions for different load cases are presented. Figure 4.1 shows the load cases applied to the plate models.

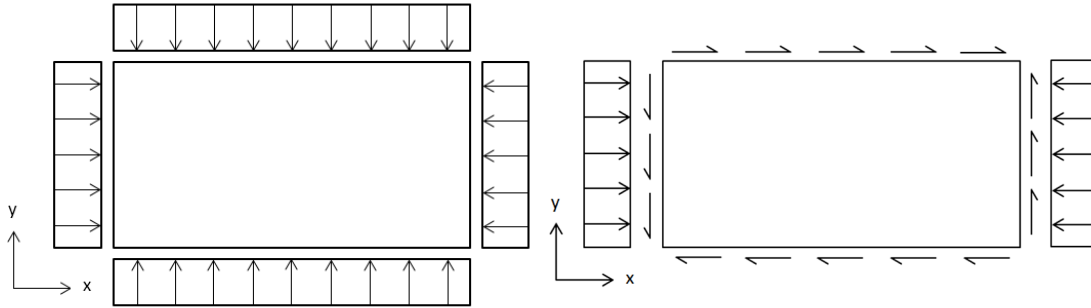


Figure 4.1 Loading conditions investigated: biaxial (a-left) and axial longitudinal/in-plane shear (b-right).

4.2.1 Uniaxial and biaxial load cases

For the uniaxial and biaxial load cases, loads were applied in a reference point outside the geometry as concentrated forces. The boundary conditions were set up so that one edge was free to move and another was restricted in the longitudinal and transverse directions, respectively, see Table 4.1. The loads in the longitudinal and transverse directions were each applied uniformly distributed over the edges by using equation constraints between the reference point and the edge free to move in the respective direction. By defining all edges as sets, the edges were made sure to remain straight when loads were applied.

Table 4.1 Boundary condition set-up used for simply supported plate under biaxial load cases where a is the length, b is the breadth and $U1-U3$ are the displacements in the respective directions.

$X=0$	$X=a$	$Y=0$	$Y=b$
$U3=0$	$U1=U3=0$	$U3=0$	$U2=U3=0$

4.2.2 Axial longitudinal/in-plane shear load cases

For the axial/shear load cases both axial loads and shear loads were applied as uniformly distributed shell edge loads. All edges were simply supported to restrict out-of-plate displacement. Instead of restricting edges in the longitudinal and transverse direction, two nodes in corners were restricted, which allowed for deformations caused by the shear loading. The boundary conditions for axial/shear loading are explained in Table 4.2.

Table 4.2 Boundary condition set-up used for simply supported plate under axial/shear load cases where a is the length, b is the breadth and $U1-U3$ are the displacements in the respective directions.

$X=0$	$X=a$	$Y=0$	$Y=b$	$X=0, Y=0$	$X=a, Y=0$
$U3=0$	$U3=0$	$U3=0$	$U3=0$	$U1=U2=0$	$U2=0$

4.3 Element type

For 2D planar shell models in Abaqus/Standard one can assign either triangular mesh elements, quadrilateral mesh elements or quad-dominated mesh elements. A quad-dominated element shape primarily uses quadrilateral elements but allows for element degeneration to triangular elements in transition regions. The elements supported for the modelling of composite shells all use five or six DOF. Elements using five DOF are

only suitable for “thin shells”, where thin-shell theory is assumed, and take no out-of-plane shear contribution into consideration. Solutions for “thick plates” can be inaccurate using elements with five DOF, why these elements were disregarded. Most element types come with the option of reduced or full integration. Reduced integration is indicated by “R” in the element name, with fewer integration points in each element. Full integration is advantageous when greater solution accuracy is required, but requires more computational effort.

With the option to choose geometric order, the available elements are a three-node linear or six-node quadratic triangular element, or a four-node linear or eight-node quadratic quadrilateral element, see Figure 4.2. Triangular elements provide accurate results in most situations but might require high mesh refinement in order to do so. That is due to utilizing constant bending and membrane strain approximations, why solutions involving large strain or high strain gradients might yield inaccurate solutions. S3 and S3R refer to the same 3-node triangular shell element that is a degenerated version of S4R, compatible with both S4R and S4. A drawback using degenerating elements is that when connection between elements change as they degenerate, the solution accuracy can be slightly off. Only using rectangular plates in this study, element degeneration is not considered necessary, why triangular elements are disregarded. The quadrilateral element types considered are four-node linear S4 or S4R and eight-node quadratic S8R, all using six DOF.

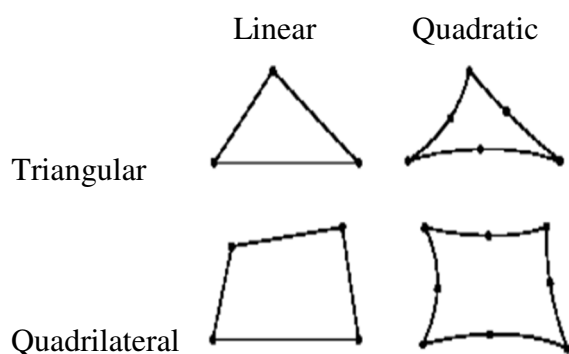


Figure 4.2 Triangular and quadrilateral element shapes with three, six, four or eight nodes, from Dassault Systèmes (2014).

S4 and S4R are both linear quadrilateral elements based on four-node elements, accounting for finite membrane strain and suitable for large strain analysis. S4 elements are fully integrated, having four integration points per elements, compared to one integration point per element for elements using reduced integration, for example S4R and S8R.

S8R is a second-order element developed for analysis of thick shells limited to small strain. Being limited to small strain, solution accuracy using S8R elements might degrade as the strain increases. In order to function properly, transverse shear flexibility is required, Dassault Systèmes (2014). Having eight nodes per element, the same accuracy can be obtained with fewer elements for plates under large deflection compared to linear quadrilateral elements with four nodes.

An analysis of the FRP Sandwich plate 2 under uniformly distributed uniaxial compression was performed for 3200, 5000 or 20000 number of elements of type S4R, 3200 elements of type S8R or 3200 elements of type S4. Figure 4.3 shows 3200 number of elements of type S4R, Figure 4.4 shows 20000 number of elements of type S4R.

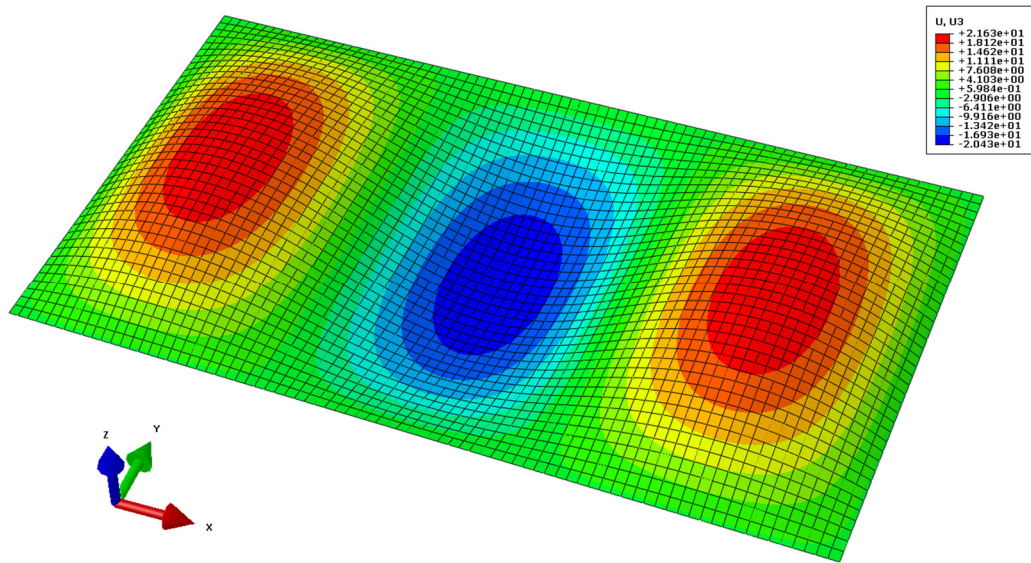


Figure 4.3 FRP Sandwich plate 2 (900x1800 mm) under uniformly distributed uniaxial compression for 3200 number of elements of type S4R showing out-of-plane displacement. The deformation was scaled with a factor of 7 in all directions.

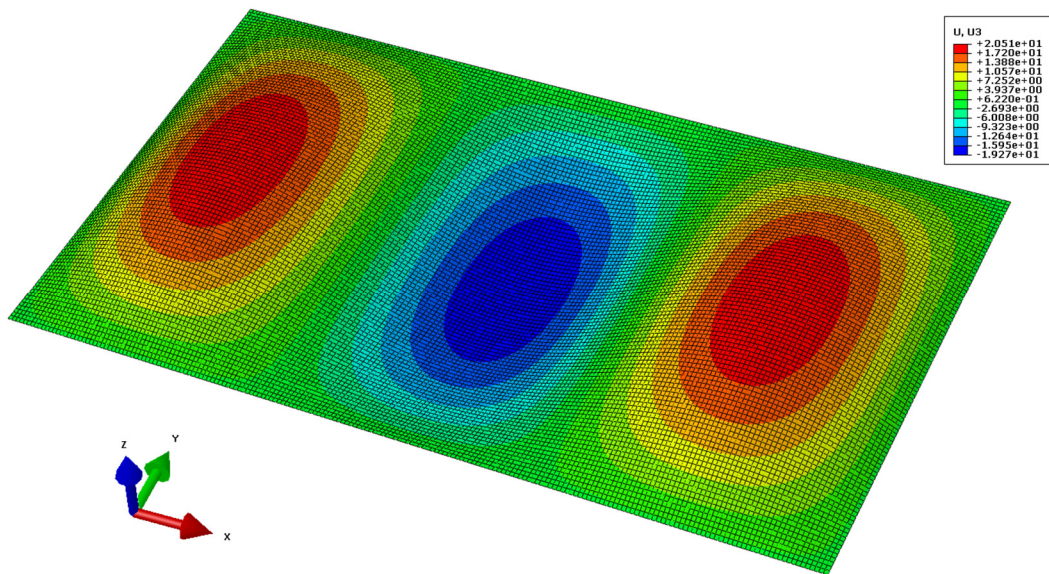


Figure 4.4 FRP Sandwich plate 2 (900x1800 mm) under uniformly distributed uniaxial compression for 20000 number of elements of type S4R showing out-of-plane displacement. The deformation was scaled with a factor of 7 in all directions.

The five cases of different numbers of elements and element type are compared in terms of load-displacement for end shortening and maximum out-of-plane displacement, see Figure 4.5, as well as the first buckling load and the FPF load, see Table 4.3.

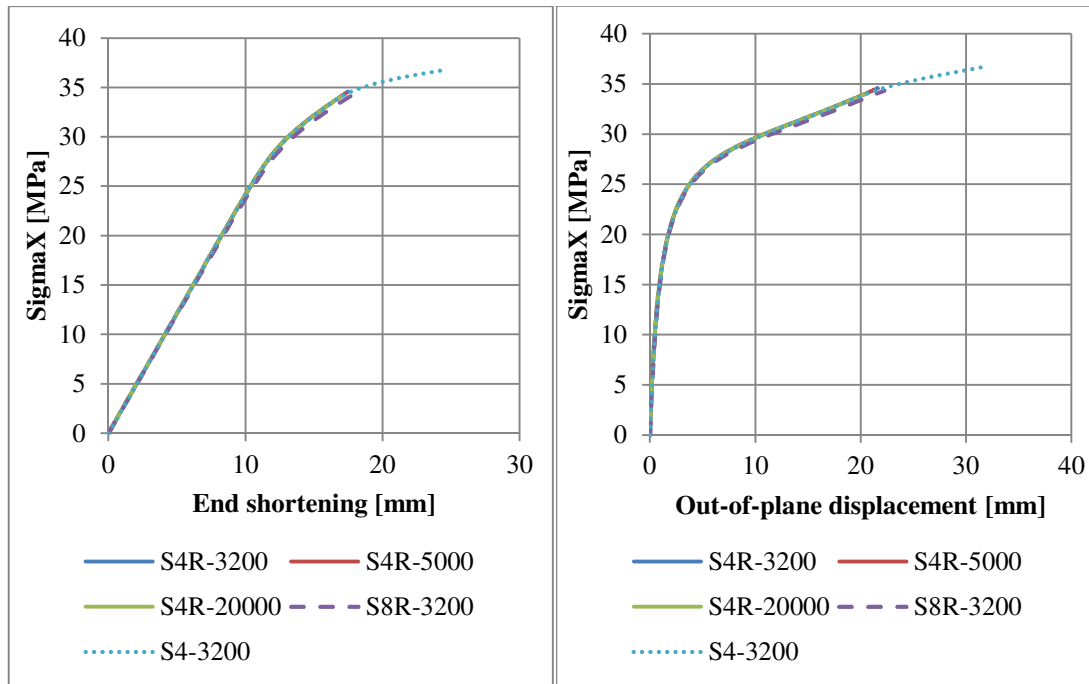


Figure 4.5 Load-displacement for FRP Sandwich plate 2 (900x1800 mm) under uniformly distributed uniaxial compression with different element types and number of elements for plate end shortening (a-left) and maximum out-of-plane displacement (b-right).

Table 4.3 First buckling load and FPF load for different element types and number of elements.

	S4R-3200	S4R-5000	S4R-20000	S8R-3200	S4-3200
Buckling load [MPa]	31.27	31.25	31.23	31.23	31.24
FPF [MPa]	28.35	28.33	28.30	28.03	28.34

For the FRP sandwich plate under investigation, FPF occurs before buckling and the limitation to small strain for S8R elements does not influence the results. Element type S4 gave the same solution as S4R, indicating that increased solution accuracy is not required. S4 outperforms S4R as well as S8R in terms of range of solution as the analysis for both S4R and S8R abort at about the same value, while S4 keeps going. This indicates that for analyses further than FPF, full integration using S4 elements might be advantageous.

Element type S8R was the most conservative even though differences were small. At the point of FPF the difference between S8R and the others element types was about 1%. The difference between type S4R with 3200 elements and 20000 elements is less than 0.2% for FPF. The S4R element was chosen as it was concluded to give results with sufficient accuracy for FRP Sandwich plate 2, having the lowest computational time. FRP Sandwich plate 2 had the most complex set-up of all plates investigated, see Appendix A, experiencing the most shear effects. Therefore, FRP Sandwich plate 2 was considered to require the most advanced element type, why element type S4R is considered to give results with sufficient accuracy for all plates.

4.4 Analysis steps

In this section the analysis procedures for each analysis step, eigenvalue analysis, load-displacement analysis and post buckling analysis up to first ply failure are presented.

In Abaqus the eigenvalue buckling problem is solved by finding buckling loads using linear perturbation. The buckling analysis is initiated at the base state, with a preload P^N subjected to the geometry. In this eigenvalue analysis where critical buckling loads are to be found, preloads are set to zero. In the buckling analysis, reference loads Q^N are scaled by load multipliers λ_i in order to find the number of requested buckling modes.

The critical buckling loads can be defined as:

$$P^N + \lambda_i Q^N = 0 \quad (4.2)$$

N is a number of degrees of freedom and i indicates the buckling mode. With zero preloads and the reference load $Q^N = 1$ MPa each eigenvalue yielded the external force subjected to the geometry, which is the critical buckling load for every buckling mode. Figure 4.6 shows the first buckling mode obtained for the FRP Sandwich plate 2 under uniaxial loading.

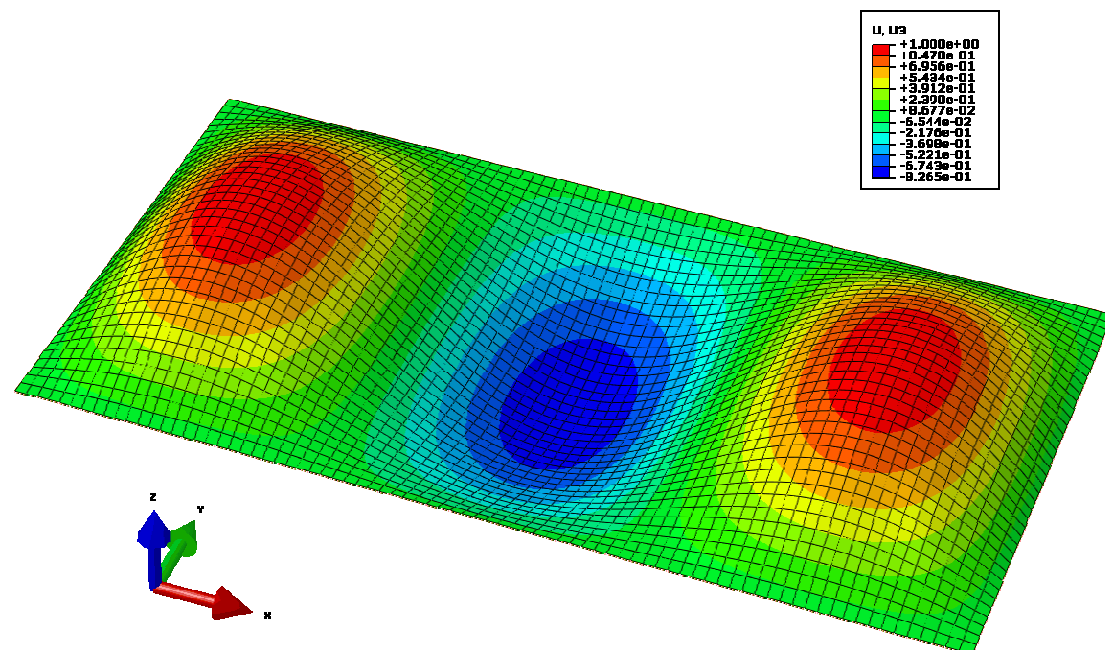


Figure 4.6 Out-of-plane displacement for the first buckling mode of FRP sandwich plate 2 (900x1800 mm) under uniformly distributed uniaxial loading in the longitudinal direction.

In Abaqus, an eigenvalue buckling analysis can sometimes result in negative eigenvalues corresponding to negative buckling modes. In most cases the occurrence of negative eigenvalues is the software's feature to indicate that the same load applied in the opposite direction would make the structure buckle. One of the most common cases is a plate under shear loading, where the same eigenvalue is reported both positive and negative, which indicates that the plate would buckle at the same shear load if applied in the opposite direction, Dassault Systèmes (2014).

In many cases the physical behaviour of negative buckling modes can be understood when displayed. Sometimes negative eigenvalues correspond to buckling modes not possible to explain in terms of physical behaviour, which could be if a preload is applied that causes geometrical nonlinearities. In such cases a geometrically nonlinear load-displacement analysis could be performed to investigate the possibility of unstable collapse. A way to avoid negative buckling modes could be by applying a preload, Dassault Systèmes (2014).

In a few cases with axial/shear loading the eigenvalue buckling analyses yielded negative eigenvalues as well as positive ones. This problem occurred especially for the SPS plate where for some load combinations no positive eigenvalues could be found without greatly increasing the number of iterations and by that the computational time. To avoid this problem the eigenvalue solver method was changed from Subspace to Lanczos, which allowed minimum eigenvalue of interest to be specified. In that way negative eigenvalues were bypassed and the positive eigenvalues found without significant difference in computational time.

The load-displacement analyses were performed using the Static Riks analysis procedure, which accounts for geometrical and material non-linearities. Static Riks is an incremental solution method with a reference load that scales with a load proportional factor for each increment. The incrementation is based on arc length allowing the Riks method to solve for loads and displacements simultaneously, Dassault Systèmes (2014).

Automatic arc length incrementation was used to allow the analyses to shorten step length when required and to increase the step when allowed in order to save computational time. The initial arc length increment was 0.1, minimum 0.001 and maximum 1 to assure continuous output without having too large steps.

For the load-displacement and post-buckling up to first ply failure analyses the buckling shape corresponding to the first buckling load was used as initial imperfection with an amplitude of 0.1% of the breadth for each plate, respectively. Initial imperfection was implemented by adding the string `*NODE FILE, U` to the keywords in the buckling analysis, which logs the shapes of all the buckling modes requested for in the analysis. The initial imperfection used was chosen by adding the string `*IMPERFECTION, FILE=file name, STEP=1`, followed by the buckling mode requested and the imperfection amplitude into the keyword of the analysis.

In the third step of the analysis, post-buckling behaviour up to first ply failure was investigated. This analysis step was performed for the FRP sandwich plate 2, see Appendix A. Damage initiation for fibre-reinforced composites based on Hashin's damage initiation theory was added to the model. The failure initiation criteria can be set to follow either the model proposed by Hashin and Rotem by setting the parameter $\alpha=0$, or the model proposed solely by Hashin, taking out-of-plane normal and shear stress contributions into consideration, by setting $\alpha=1$, see Appendix G. For this study the Hashin failure criteria, see Chapter 2.4.3, was used to register failure initiation.

4.5 Mesh convergence study

A mesh convergence study was performed in order to investigate the required mesh size for convergence of Abaqus results, and at the same time keep the number of elements down in order to maintain computational efficiency. The convergence study was performed by computing the eigenvalue corresponding to first buckling load for a set of mesh sizes under biaxial or axial/shear loading. As the four plates used in the study

have different aspect ratios, the number of elements was determined along the breadth. Each plate was assigned mesh with 10, 15, 20, 30, 50 and 100 elements over its breadth, respectively, as well as an initial mesh size generated by default settings in Abaqus. The range of the initial default meshes varied from 10 to 25 elements along the breadth for the four different plates. The mesh convergence study was performed with S4R elements used in the study, see Chapter 4.3. Figure 4.7 shows the mesh convergence for the FRP Sandwich plate 2.

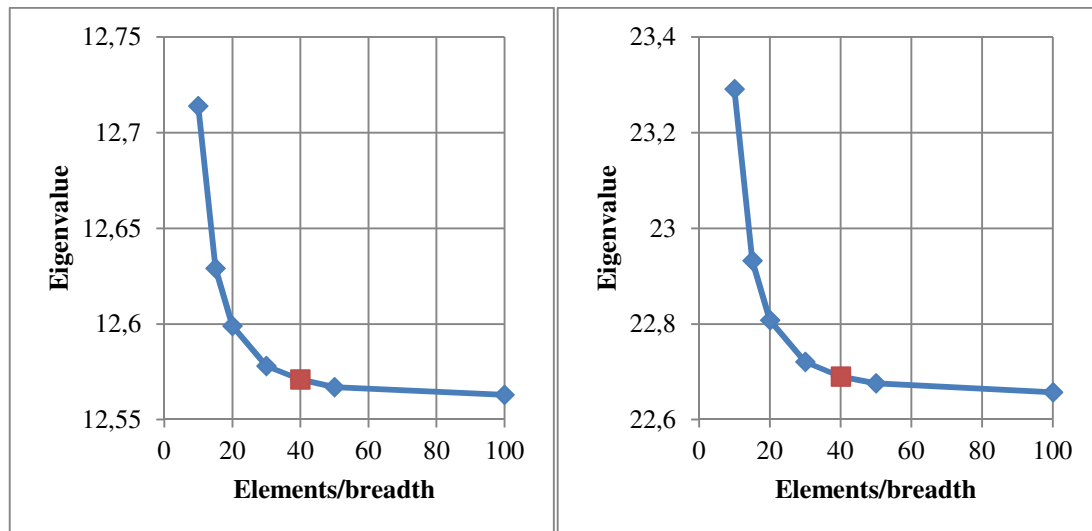


Figure 4.7 Mesh convergence for FRP Sandwich plate 2 (900x1800 mm) subjected to biaxial (a-left) or axial/shear (b-right) loading. The chosen mesh size is indicated with a red square in the figures.

All but one initial mesh size for the four plates showed less than 1% difference for first buckling load compared to the finest and converged mesh with 100 elements along the breadth. The value not below 1% difference was the single-skin FRP composite plate under axial/shear loading, where the buckling load was 2.3% higher. The mesh was still believed to give results accurate enough for the eigenvalue analysis. For the load-displacement analysis a new mesh was regenerated for the single-skin FRP Composite plate so that all plates contained a mesh with at least 20 elements along the breadth, which assured less than 1% difference in results compared to the finest and converged mesh size. For the FRP Sandwich plate 2, a mesh size with 40 elements along its breadth was assigned for the failure initiation analysis. 40 elements along the breadth correspond to 3200 number of elements in total with element sizes of 22.5x22.5 mm.

5 Results and discussion

This chapter presents the results from all numerical simulations and calculations using the different versions of the PULS codes and the FE models presented in Chapter 4. Together with the results, detailed discussions of observations made are presented. The different versions of the PULS codes are referred to as C-PULS (Composite PULS, described in Chapter 2.5) and S-PULS (Sandwich PULS, developed in this thesis as described in Chapter 3). The structure of this chapter follows the methodology of this thesis, which is presented in Chapter 1.3.

Results presented as interaction curves for the plates under biaxial loads show interaction for the applied uniformly distributed longitudinal and transverse loads. Interaction curves for the plates under axial/shear loads show interaction for the applied uniformly distributed uniaxial longitudinal and shear loads.

In Chapter 5.1 the eigenvalue analysis results are presented and discussed for all four plates investigated, see Appendix A. The discussion is focused on the agreement between the first buckling loads from S-PULS and Abaqus, as well as on the differences between the first buckling loads from S-PULS and C-PULS. The first buckling loads are presented as interaction curves for varying combinations of biaxial or axial/shear load cases. “SigmaX,crit.” and “SigmaY,crit.” denote the first buckling loads in the longitudinal and transverse directions, respectively. “TauXY,crit.” denotes the first buckling load, when the plates are subjected to shear load.

In Chapter 5.2 the load-displacement analysis is presented. Load-displacement curves are obtained, describing model response, for all four plates, see Appendix A, under uniformly distributed uniaxial longitudinal compression denoted as “SigmaX”.

Chapter 5.3 presents the failure initiation analysis. The FPF and sandwich failure loads are presented as interaction curves for the FRP Sandwich plate 2, see Appendix A, under varying combinations of biaxial or axial/shear loads. “SigmaX,fail.” and “SigmaY,fail.” denote the failure initiation loads in the longitudinal and transverse directions, respectively. “TauXY,fail.” denotes the failure initiation load, when the plates are subjected to shear load.

Final parts of this chapter cover sensitivity studies performed on the FRP Sandwich plate 2 presented in Chapter 5.4, which provide an assessment of the Sandwich PULS code validity for different breadth-to-thickness, face-to-core shear stiffness and aspect ratios.

As explained in Chapter 3.3, different options for the shear stiffness evaluation of sandwich plates are implemented in the Sandwich PULS code and used for the FRP Sandwich plate 2. Results dependent on these evaluation options and are denoted as:

- Kopt1: shear stiffness evaluated using Equation (3.7c),
- Kopt2: shear stiffness evaluated using Equation (3.7d),
- Kopt3: shear stiffness evaluated using Equation (3.7b),
- K=5/6: shear stiffness evaluated using Equation (3.7a).

5.1 Eigenvalue analysis

Validation of the Sandwich PULS code, after the implementation of FSDT, for the eigenvalue analysis was done in steps for plates with increasing complexity. The Sandwich PULS code was tested and validated for the SPS, single-skin FRP Composite plate, FRP Sandwich plate 1 and for the FRP Sandwich plate 2. Plate dimensions and material properties for the plates can be found in Appendix A. Sandwich PULS (S-PULS) is compared to Composite PULS (C-PULS) and validated against Abaqus.

5.1.1 Sandwich Plate System (SPS)

For the biaxial load cases, differences between S-PULS and Abaqus results are up to 13%, see Figure 5.1, while for the axial/shear load cases differences are below 5%, see Figure 5.2. For the SPS plate the importance of transverse shear deformations is large. S-PULS shows good agreement with Abaqus, while C-PULS gives overestimated first buckling loads.

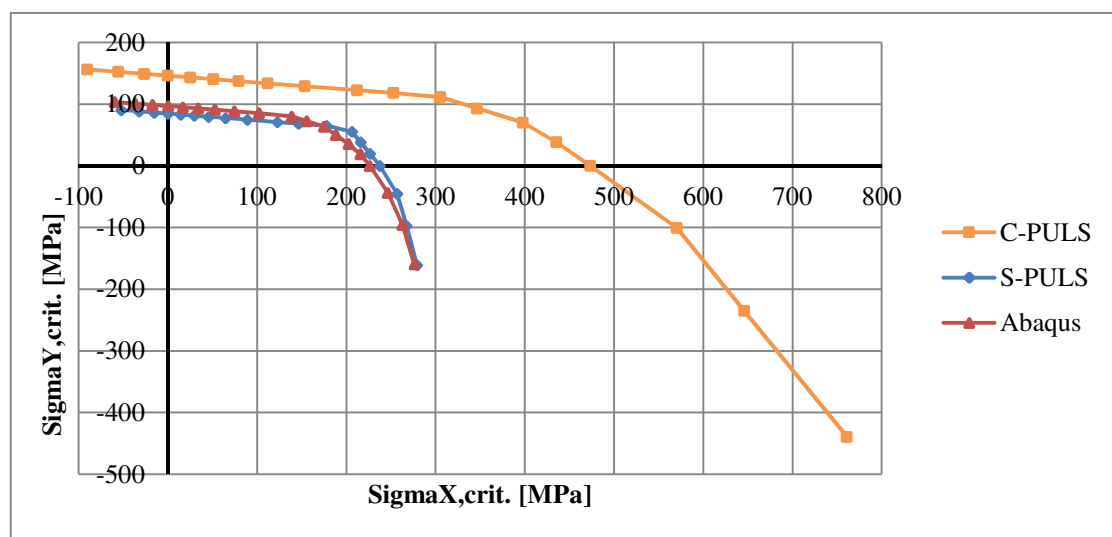


Figure 5.1 The first buckling load interaction curves for the SPS plate under biaxial loads for C-PULS and S-PULS, validated against Abaqus.

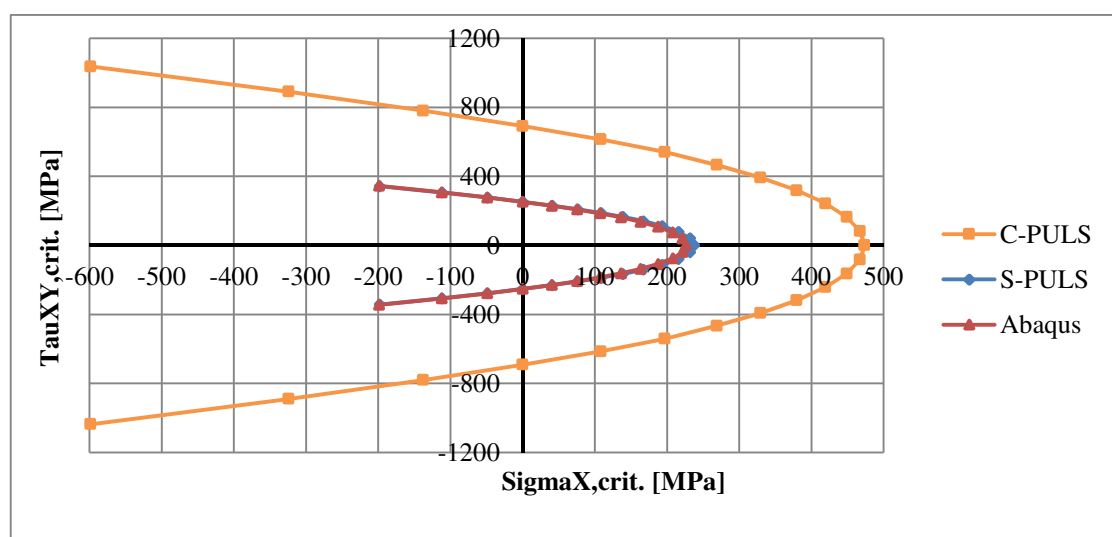


Figure 5.2 The first buckling load interaction curves for the SPS plate under axial/shear loads for C-PULS and S-PULS, validated against Abaqus.

The different buckling modes, i.e. different numbers of half-sine waves in the longitudinal direction, yield different first buckling loads as presented in Figure 5.3. In S-PULS the first buckling modes shift from four half-sine waves ($m = 4$) to only one half-sine wave ($m = 1$) in the longitudinal direction. Abaqus yields a buckling mode shifting in steps from four to one half-sine waves, which can explain the disagreement between the S-PULS and Abaqus predicted first buckling loads in this region.

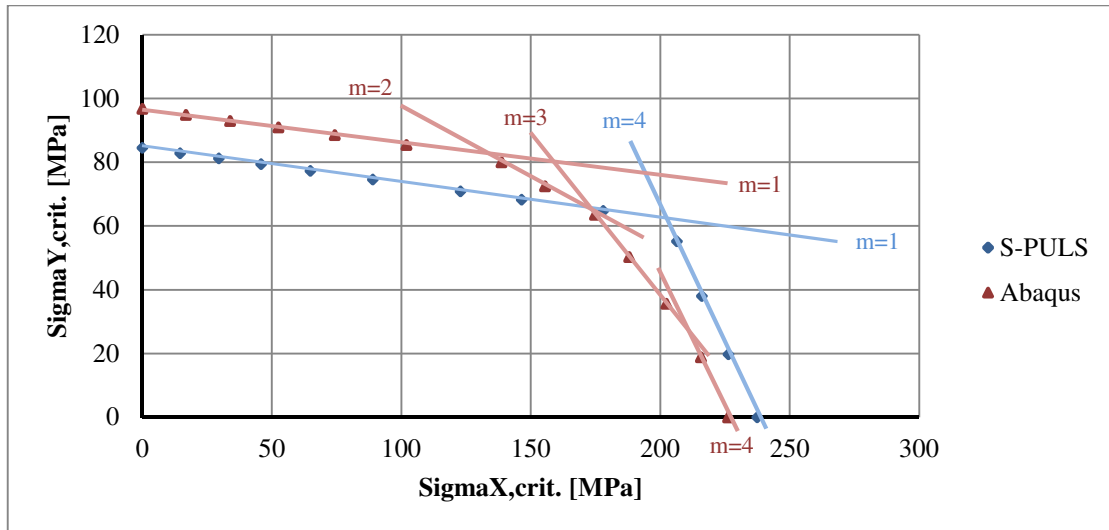


Figure 5.3 Shifting between different buckling modes for S-PULS and Abaqus, where m is number of half-sine waves in the longitudinal direction.

5.1.2 Single-skin FRP Composite plate

Both C-PULS and S-PULS show good agreement with Abaqus for biaxial and axial/shear loading cases. For biaxial loading differences between S-PULS and Abaqus are at most 2.1%, see Figure 5.4. For the axial/shear loading case, shown in Figure 5.5, differences between the results are up to 9%; a majority of the results still differ less than 5%.

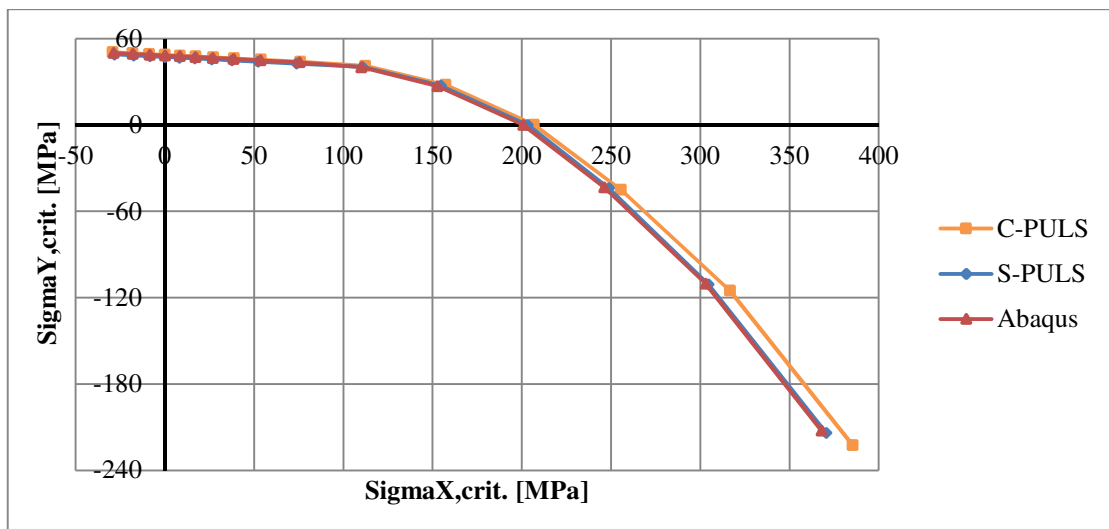


Figure 5.4 The first buckling load interaction curves for the single-skin FRP Composite plate under biaxial loads for C-PULS and S-PULS, validated against Abaqus.

S-PULS is more conservative for positive shear loads, while for opposite shear loads it is less conservative, see Figure 5.5. Results obtained with C-PULS and S-PULS are symmetric, i.e. an opposite direction of the shear load gives the same eigenvalue, while the Abaqus interaction curve is shifted down.

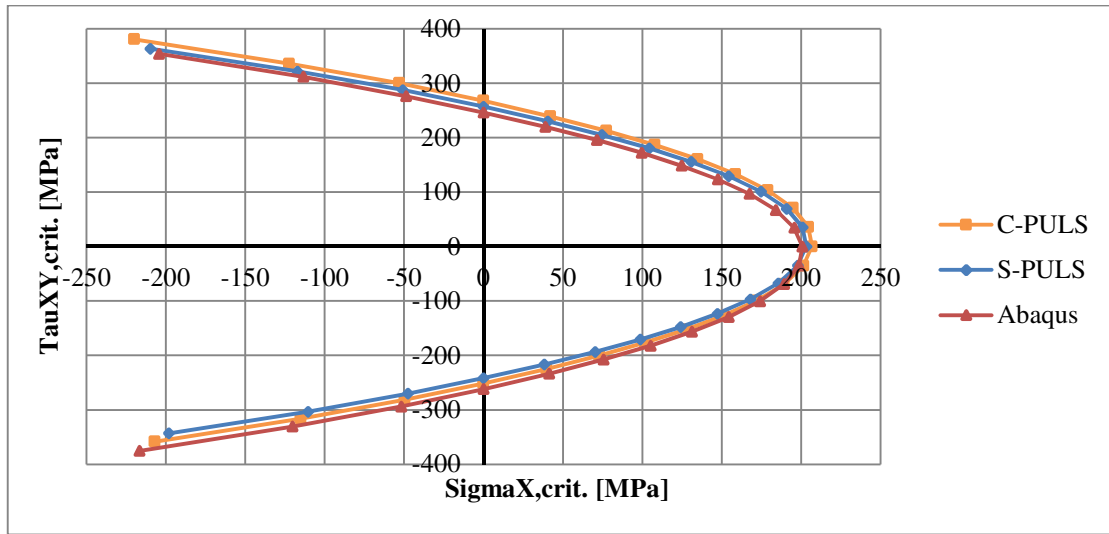


Figure 5.5 The first buckling load interaction curves for the single-skin FRP Composite plate under axial/shear loads for C-PULS and S-PULS, validated against Abaqus.

Since the single-skin composite plate analysed is considered as a thin plate, the effect from shear strains accounted for in S-PULS is small, resulting in very similar results for C-PULS and S-PULS.

5.1.3 FRP Sandwich plate 1

The FRP sandwich plate 1 shows good results under both biaxial loading, see Figure 5.6, and axial/shear loading, see Figure 5.7. In both cases the differences between S-PULS and Abaqus are less than 2%.

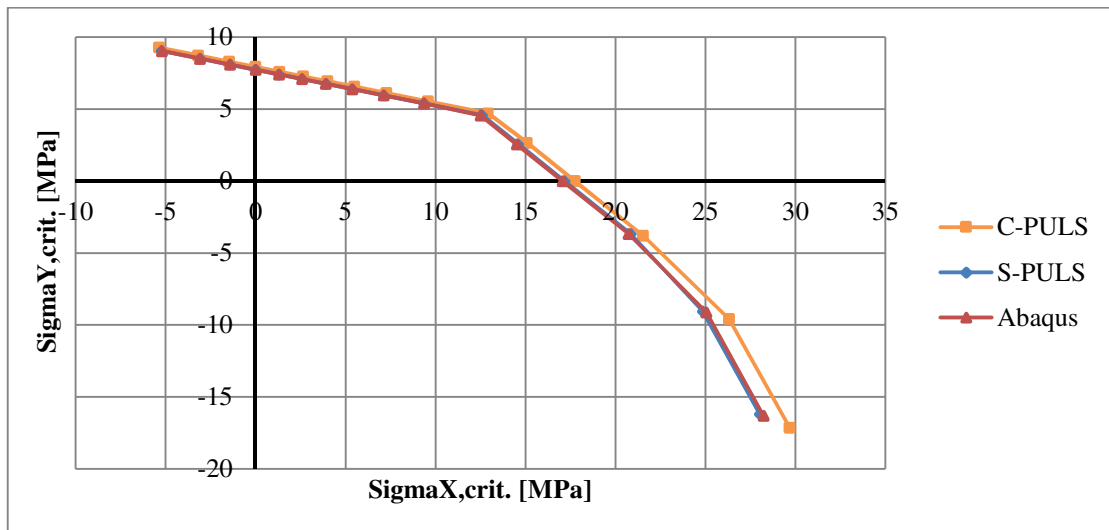


Figure 5.6 The first buckling load interaction curves for the FRP Sandwich plate 1 under biaxial loads for C-PULS and S-PULS, validated against Abaqus.

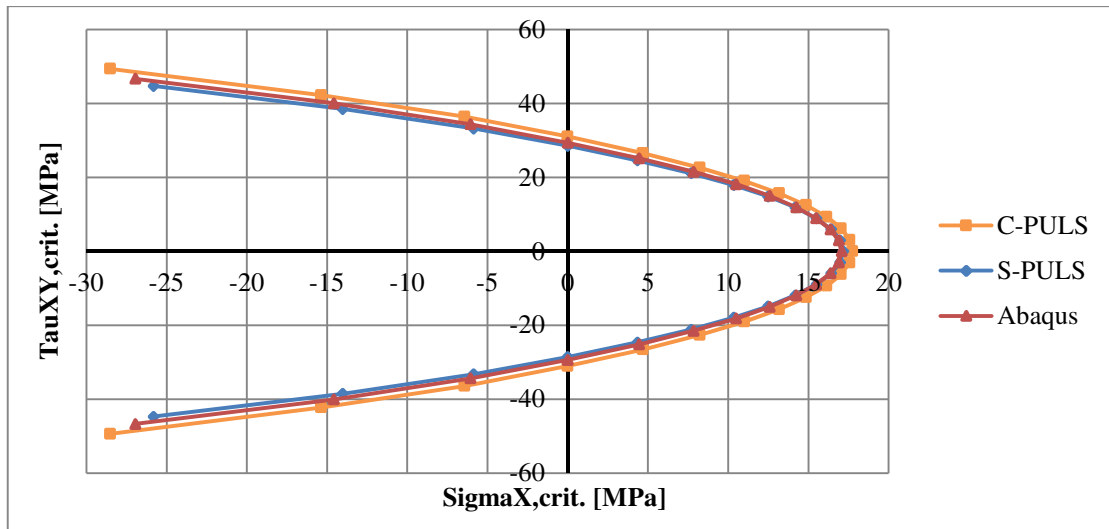


Figure 5.7 The first buckling load interaction curves for the FRP Sandwich plate 1 under axial/shear loads for C-PULS and S-PULS, validated against Abaqus.

It can be noticed that C-PULS and S-PULS show very similar results. As for the single-skin composite plate the FRP Sandwich plate 1 is considered as a thin plate, where the effect from shear strains is small. Additionally, the plate does not fulfil assumptions of the sandwich plate theory implemented in S-PULS, presented in Chapter 3.3, since the faces are not thin compared to the core thickness.

5.1.4 FRP Sandwich plate 2

The FRP sandwich plate 2 shows good agreement between “S-PULS, Kopt1”, “S-PULS, Kopt2” and Abaqus under biaxial load cases, see Figure 5.8, and axial/shear load cases, see Figure 5.9. C-PULS gives overestimated critical buckling loads, while “S-PULS, Kopt3” results are over-conservative for all load cases. “S-PULS, Kopt1” shows better agreement for the plate under biaxial loads, while “S-PULS, Kopt2” gives better results for the plate under axial/shear loads compared with Abaqus.

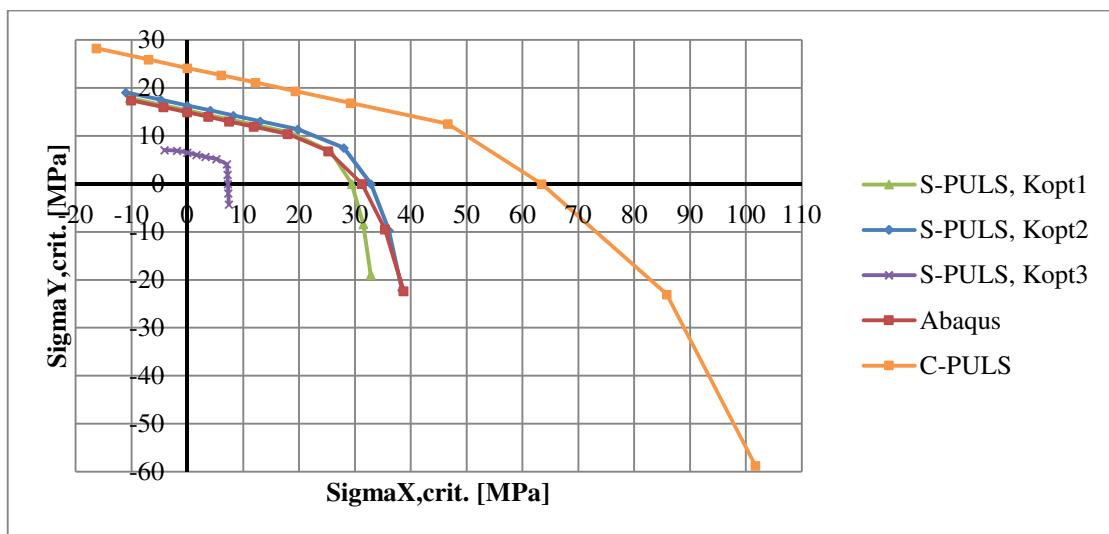


Figure 5.8 The first buckling load interaction curves for the FRP Sandwich plate 2 under biaxial loads for C-PULS and S-PULS with different shear stiffness evaluation options, validated against Abaqus.

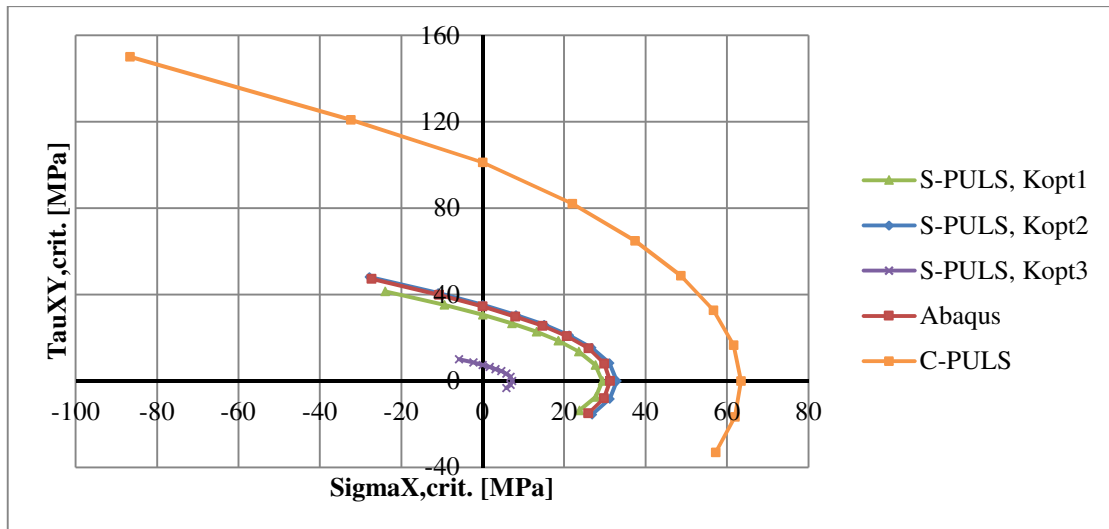


Figure 5.9 The first buckling load interaction curves for the FRP Sandwich plate 2 under axial/shear loads for C-PULS and S-PULS with different shear stiffness evaluation options, validated against Abaqus.

FRP Sandwich plate 2 fulfils the assumptions of the sandwich plate theory implemented in S-PULS, presented in Chapter 3.3, having thick and soft core and thin faces. The effect from shear strains is great and “S-PULS, Kopt1” and “S-PULS, Kopt2” outperforms C-PULS. “S-PULS, Kopt1” is more conservative compared to “S-PULS, Kopt2”, since the latter one accounts for some of the face thickness, which slightly increases shear stiffness, see Chapter 3.3.

5.1.5 Concluding remarks

It was found that for the SPS plate and the FRP Sandwich plate 2, where the effects from shear strains are considerable, CLT is no longer adequate and the difference between C-PULS compared to S-PULS and Abaqus is significant. For FRP Sandwich plate 2 critical buckling loads predicted by S-PULS are within a 10%, mostly below a 5%, difference compared to results obtained in Abaqus.

In few cases, S-PULS and Abaqus yield different first buckling modes, i.e. a different number of half-sine waves. An investigation with increased degrees of freedom for the approximation functions in S-PULS was performed as an attempt to increase the accuracy, but showed no effect on the results. It is therefore believed that a slight difference between S-PULS and Abaqus evaluated shear stiffness of the plate is the reason for differently predicted first buckling modes.

For the FRP Sandwich plate 2, the first buckling loads are slightly on the conservative side for “S-PULS, Kopt1”, while for “S-PULS, Kopt2” the first buckling loads are slightly on the non-conservative side. The “S-PULS, Kopt3” shear stiffness evaluation option is over-conservative.

5.2 Load-displacement analysis

The load-displacement analysis with linear material properties was performed in order to validate the model response for Sandwich PULS (S-PULS). The maximum out-of-plane displacement was investigated for all four plates, see Appendix A, subjected to uniformly distributed uniaxial compression. Results were compared to Composite PULS (C-PULS) and validated against Abaqus. To distinguish between pre- and post-buckling behaviour, first buckling loads are represented by dashed horizontal lines.

It should be mentioned that the PULS codes underestimate displacements in general. This is due to the Rayleigh-Ritz method that has been used to approximate displacements, which results in a stiffer model, see Appendix E.1.

5.2.1 Sandwich Plate System (SPS)

As for the eigenvalue analysis, S-PULS gives a significantly better estimation of the model response than C-PULS, see Figure 5.10. Even though the S-PULS and Abaqus predicted first buckling loads are close, the differences between the predicted out-of-plane displacements at the first buckling loads are large. The differences are due to different shear stiffness estimations, as established in the eigenvalue analysis, see Chapter 5.1.1. In Figure 5.10 it is seen that the difference between S-PULS and C-PULS is not only at the point of first buckling load, as differences are present throughout the plate response. The load-displacement curves for S-PULS and C-PULS do not converge toward Abaqus due to the different shear stiffness estimations.

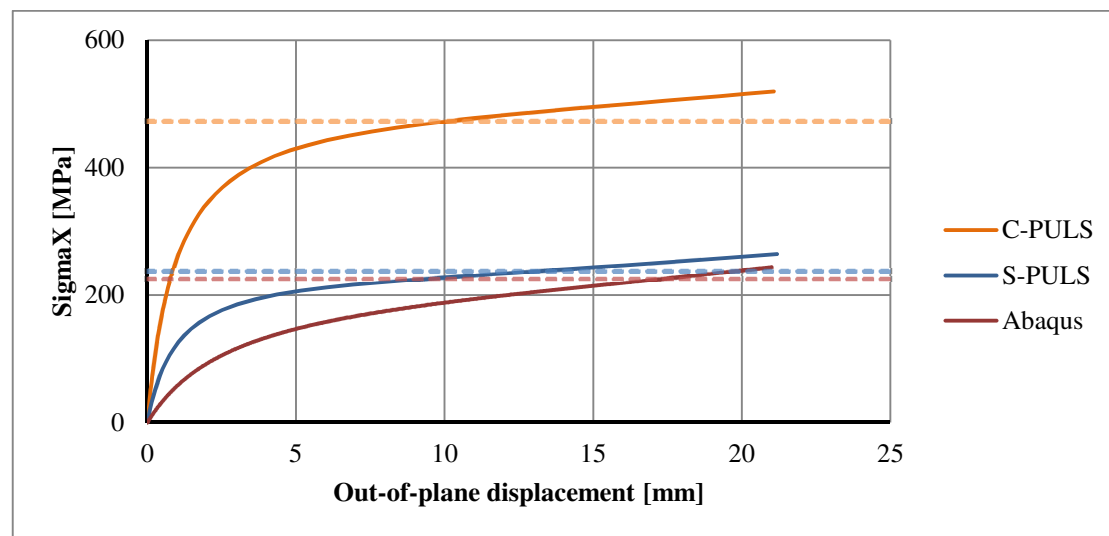


Figure 5.10 Maximum out-of-plane displacement (@L/8) curves for the SPS plate under uniaxial compression for C-PULS and S-PULS, validated against Abaqus.

5.2.2 Single-skin FRP Composite plate

The single-skin FRP Composite plate shows similar results for S-PULS and C-PULS. Both PULS codes deviate the most at small out-of-plane displacements, while they converge towards the Abaqus plate behaviour for larger out-of-plane displacements, see Figure 5.11. As explained in the eigenvalue analysis, see Chapter 5.1.2, the differences between S-PULS and C-PULS are small due to the small effects of shear strains for the single-skin FRP Composite plate. As concluded by Braaten and Boström (2013), differences between Abaqus and C-PULS are partly due to the Rayleigh-Ritz approximation method in combination with the perturbation method, where the non-linear contribution from the large deflection theory is neglected. S-PULS being based on C-PULS, see Chapter 1.4, inherits the same weaknesses.

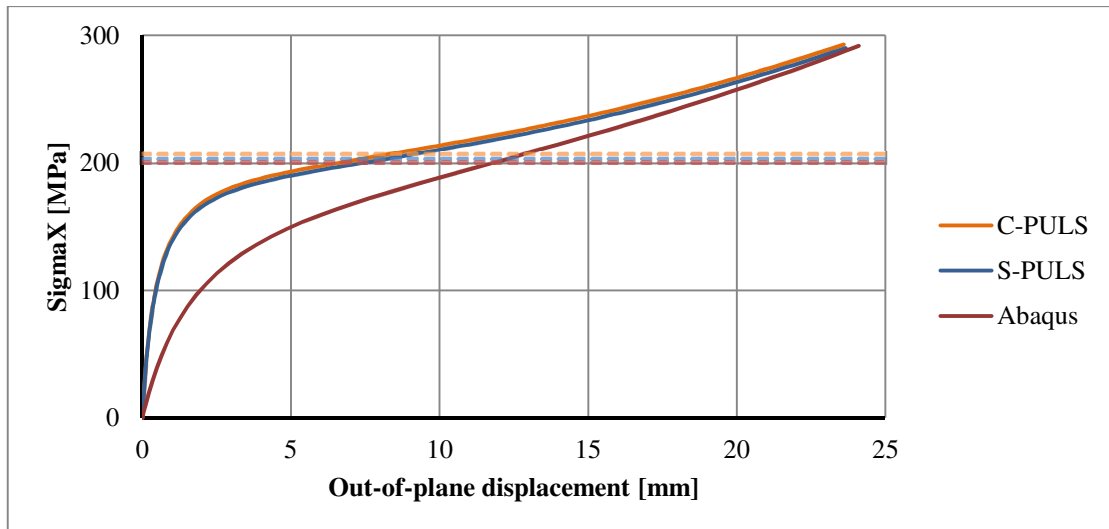


Figure 5.11 Maximum out-of-plane displacement ($@L/6$) curves for the single-skin FRP Composite plate under uniaxial compression for C-PULS and S-PULS, validated against Abaqus.

5.2.3 FRP Sandwich plate 1

As with the single-skin FRP Composite plate, see Chapter 5.2.2, the differences between C-PULS, S-PULS and Abaqus, see Figure 5.12, can be explained by the Rayleigh-Ritz and linear perturbation methods implemented in the PULS codes. There are noticeable differences between S-PULS and C-PULS, which are due to the reduced sandwich plate shear stiffness implemented in S-PULS, see Chapter 3.3. The effect of shear strains is relatively small, since the plate is rather thin, which is explained in the eigenvalue analysis of the same plate, see Chapter 5.1.3. For larger out-of-plane displacements, i.e. more than 10 mm for this case, the C-PULS and S-PULS plate responses converge towards the Abaqus-predicted plate response. The C-PULS and S-PULS curves remain parallel to each other for the larger displacements due to different estimates of shear stiffness.

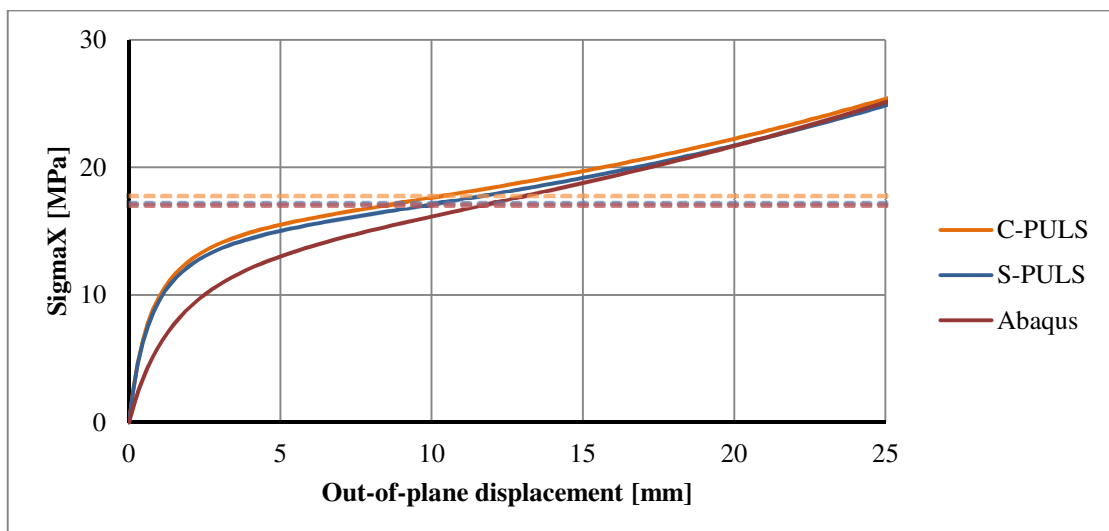


Figure 5.12 Maximum out-of-plane displacement ($@L/4$) curves for the FRP Sandwich plate 1 under uniaxial compression for C-PULS and S-PULS, validated against Abaqus.

5.2.4 FRP Sandwich plate 2

The FRP Sandwich plate 2 is considered as a thick plate with thin faces and soft core, which is why the effect of shear strains is great and significant differences between C-PULS and S-PULS occur, see Figure 5.13. Different options for shear stiffness evaluation have been used in S-PULS, see Chapter 3.3. “S-PULS, Kopt1” and “S-PULS, Kopt2” give a good plate response, which is close to Abaqus. As with the eigenvalue analysis of the plate, presented in 5.1.4, the “S-PULS, Kopt3” curve gives a too weak plate response, while C-PULS gives a too stiff plate response. Small enough incremental steps have been used to reduce the weakness of the PULS codes when neglecting the non-linear terms from the large deflection theory.

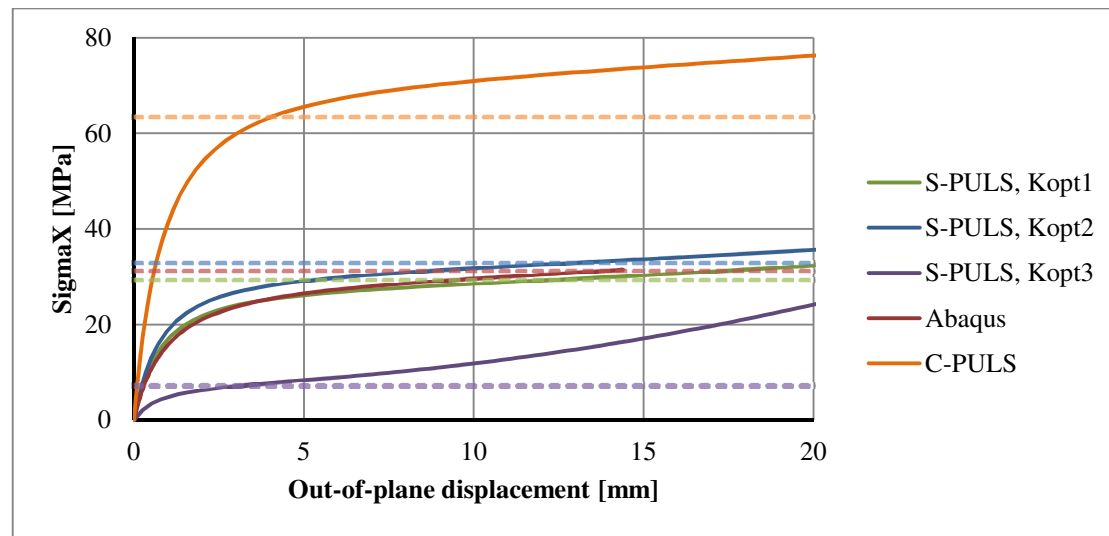


Figure 5.13 Maximum out-of-plane displacement (@L/6) curves for the FRP Sandwich plate 2 under uniaxial compression for C-PULS and S-PULS with different shear stiffness evaluation options, validated against Abaqus.

End shortening curves for the FRP Sandwich plate 2 under uniaxial compression are shown in Figure 5.14. When “S-PULS, Kopt3” reaches a critical buckling load, see Figure 5.14 at around 8 MPa, the other options are still predicting linear plate response. After a load of 30 MPa is reached “S-PULS, Kopt1” and “S-PULS, Kopt2” reach their critical buckling load approximately together with Abaqus. The effect of shear strains is not accounted for in C-PULS, which results in a too stiff plate behaviour and the C-PULS plate response remains in the linear pre-buckling behaviour. Other curves are deep in the post-buckling behaviour when C-PULS reaches the critical buckling load, not seen in Figure 5.14.

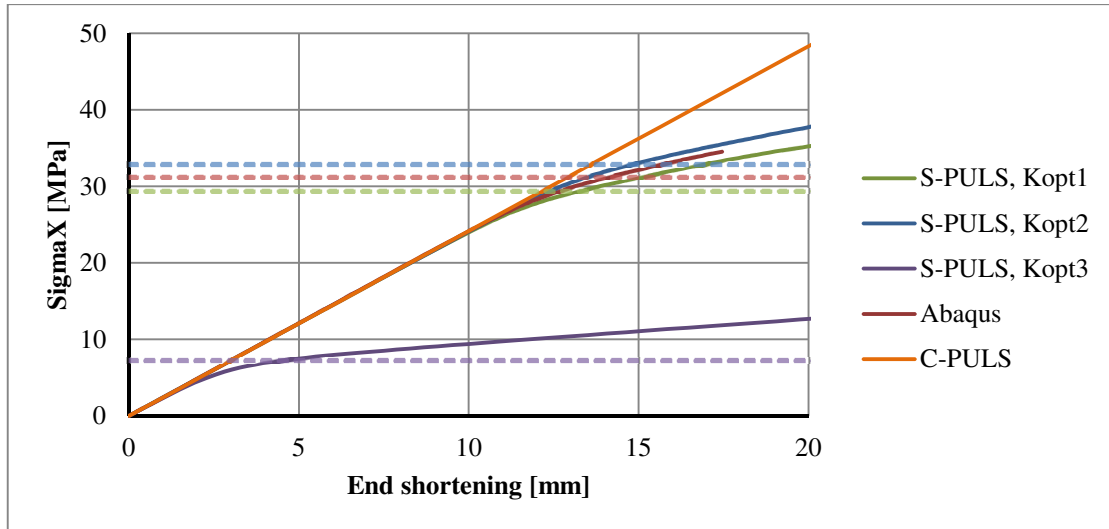


Figure 5.14 End shortening curves for the FRP Sandwich plate 2 under uniaxial compression for C-PULS and S-PULS with different shear stiffness evaluation options, validated against Abaqus.

5.2.5 Concluding remarks

S-PULS predicts a better model response than C-PULS, especially for the FRP Sandwich plate 2 where the effect from shear strains is large. Compared to Abaqus, S-PULS predicts a stiffer model response for the SPS plate, single-skin FRP Composite plate and FRP Sandwich plate 1.

For the FRP Sandwich plate 2, the shear stiffness evaluation option “S-PULS, Kopt1” is slightly on the conservative side, “S-PULS, Kopt2” is slightly on the non-conservative side and “S-PULS, Kopt3” is over-conservative, in agreement with the eigenvalue analysis.

5.3 Failure initiation analysis

This chapter presents failure initiation interaction curves for biaxial and axial/shear load cases for the FRP Sandwich plate 2. Due to the small shear strain effect for the FRP Sandwich plate 1 and because it does not fulfil the assumptions of the sandwich plate theory, see Chapter 3.3, only the FRP Sandwich plate 2 was chosen for the failure initiation analysis. Failure initiation is defined as the first ply failure (FPF) according to the Hashin-Rotem criterion and as the face wrinkling and shear crimping critical loads in Sandwich PULS (S-PULS), see Chapter 2.4. Abaqus registers FPF according to the Hashin failure criterion, see Appendix G.

5.3.1 Hashin-Rotem failure criteria

Results of FPFs under biaxial load cases are presented in Figure 5.15, and under axial/shear load cases in Figure 5.16, as interaction curves. S-PULS registers failure initiation much earlier than Abaqus, especially when a longitudinal compressive load is dominant, i.e. when $\sigma_x > \sigma_y$ or $\sigma_x > \tau_{xy}$. There is only a small difference between “S-PULS, Kopt1” and “S-PULS, Kopt2”.

The FPFs are initiated before the first buckling loads for most load cases. Due to the soft core, loads are taken by the FRP faces, which are thin. From a design point of view, it is believed that to reach the post-buckling plate behaviour, i.e. an FPF load higher than first buckling load, either a stiffer core or faces with increased thickness should be

used. Post-buckling behaviour can also be reached if FFF is evaluated or if a degradation model until LPF would be implemented in the S-PULS code, which is not within the scope of this thesis.

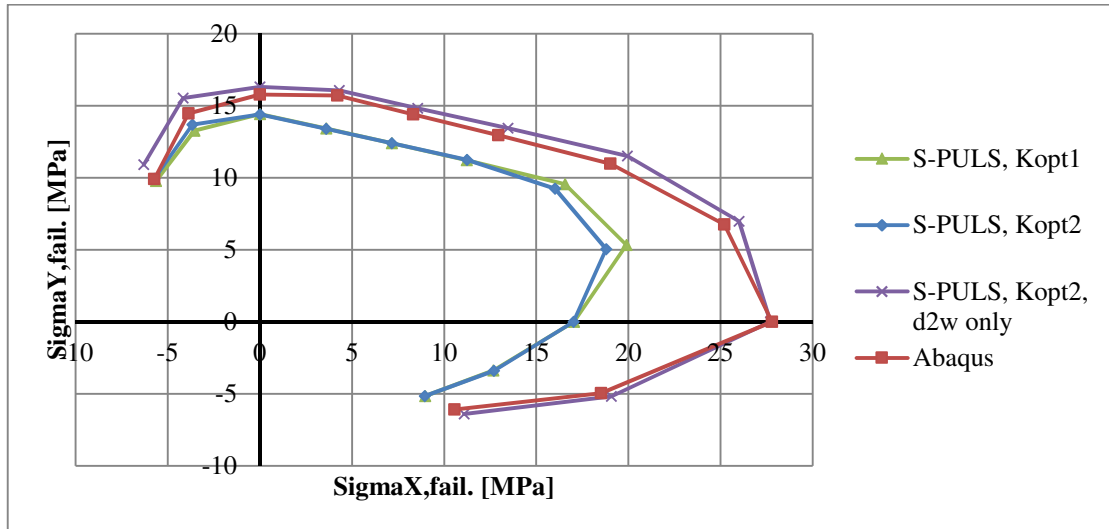


Figure 5.15 FPF interaction curves for the FRP Sandwich plate 2 under biaxial loads for S-PULS with different shear stiffness evaluation options, validated against Abaqus.

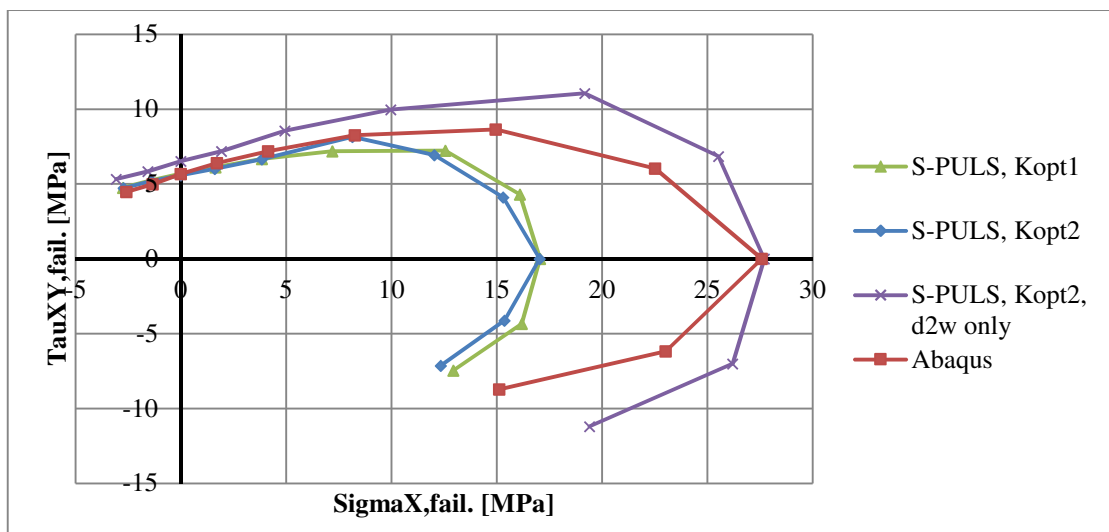


Figure 5.16 FPF interaction curves for the FRP Sandwich plate 2 under axial/shear loads for S-PULS with different shear stiffness evaluation options, validated against Abaqus.

Positions where the FPFs are initiated in the plate are the same for S-PULS and Abaqus. The FPFs occur at the place of the maximum out-of-plane displacement, i.e. at the extremes of half-sine waves, and are initiated by matrix tension failure. The matrix failure is initiated in the same plies both for S-PULS and Abaqus in most load cases, see Table 5.1 and Table 5.2.

For rectangular plates with an aspect ratio of 2 and symmetrical layup, FPF can be initiated at two different positions. If ply failure is initiated at the position of a maximum positive half-sine wave, the ply that is on the opposite side of the midplane most likely fails at the same time, but at the position of the maximum negative half-sine wave. This

occurs for some load cases for the FRP Sandwich plate 2 analysed, see Table 5.1 and Table 5.2.

Table 5.1 Ply numbers and fibre orientation (in parenthesis) where the FPFs occur for biaxial load cases. The relationship between the components of the reference loads for biaxial load cases are indicated in the first two columns. MT indicates matrix tension failure.

SigmaX [MPa]	SigmaY [MPa]	S-PULS	Abaqus
0.87	-0.50	MT – 10 (0°)	MT – 1, 10 (0°)
0.97	-0.26	MT – 10 (0°)	MT – 10 (0°)
1.00	0.00	MT – 1, 10 (0°)	MT – 10 (0°)
0.97	0.26	MT – 1, 10 (0°)	MT – 1, 10 (0°)
0.87	0.50	MT – 1, 10 (0°)	MT – 10 (0°)
0.71	0.71	MT – 1, 10 (0°)	MT – 10 (0°)
0.50	0.87	MT – 10 (0°)	MT – 10 (0°)
0.26	0.97	MT – 10 (0°)	MT – 10 (0°)
0.00	1.00	MT – 10 (0°)	MT – 7 (90°)
-0.26	0.97	MT – 7 (90°)	MT – 7 (90°)
-0.50	0.87	MT – 4, 7 (90°)	MT – 7 (90°)

Table 5.2 Ply numbers and fibre orientation (in parenthesis) where the FPFs occur for axial/shear load cases. The relationship between the components of the reference loads for axial/shear load cases are indicated in the first two columns. MT indicates matrix tension failure.

SigmaX [MPa]	TauXY [MPa]	S-PULS	Abaqus
0.87	-0.50	MT – 8 (45°)	MT – 10 (0°)
0.97	-0.26	MT – 10 (0°)	MT – 1 (0°)
1.00	0.00	MT – 1, 10 (0°)	MT – 10 (0°)
0.97	0.26	MT – 10 (0°)	MT – 1 (0°)
0.87	0.50	MT – 9 (-45°)	MT – 10 (0°)
0.71	0.71	MT – 9 (-45°)	MT – 9 (-45°)
0.50	0.87	MT – 2, 9 (-45°)	MT – 9 (-45°)
0.26	0.97	MT – 2, 9 (-45°)	MT – 2 (-45°)
0.00	1.00	MT – 9 (-45°)	MT – 2 (-45°)
-0.26	0.97	MT – 2, 9 (-45°)	MT – 9 (-45°)
-0.50	0.87	MT – 9 (-45°)	MT – 9 (-45°)

According to DNV (2013), matrix failure is not a preferred failure mode and is to be avoided. Structural design principles suggest that the layup shall be designed in such a way that loads are carried mainly by the fibres, so that fibre failure is critical. Here, the FPFs are initiated by matrix failure, which is expected for compressive loads, see Chapter 2.3.

The differences between the S-PULS and Abaqus results presented in Figure 5.15 and Figure 5.16, might be explained by how the stresses in each ply are calculated, i.e. based on how the curvatures are obtained in the S-PULS code. The “S-PULS, Kopt1” and “S-PULS, Kopt2” results are based on the FSDT defined curvatures, see Equation (B.5). If neglecting the in-plane shear strain derivatives, i.e. the curvatures dependent on the second derivative of the out-of-plane displacement only, as done in “S-PULS, Kopt2, d2w only”, there is good concordance between S-PULS and Abaqus for the biaxial load cases, see Figure 5.15. For the axial/shear load cases there is good concordance between S-PULS and Abaqus only for the longitudinal uniaxial load case, i.e. $\sigma_x > 0, \tau_{xy} = 0$. The other FPF results for axial/shear load cases are over-predicted, see Figure 5.16.

5.3.2 Sandwich failure criteria

Sandwich failure criteria, the face wrinkling and shear crimping criteria, are evaluated for the biaxial and axial/shear load cases using the shear stiffness evaluation option “Kopt2”, see Figure 5.17 and Figure 5.18. These failure criteria are designed for compressive (and primarily uniaxial) loads only, as explained in Chapters 2.4.1 and 2.4.2.

The sandwich failure results obtained by S-PULS are somewhat satisfactory. They are only compared to the Hashin FPF criterion, since the face wrinkling (FW) and shear crimping (SC) criteria do not exist in Abaqus. For both load cases, face wrinkling will occur in the plate before shear crimping when longitudinal axial loads are dominant, i.e. when $\sigma_x > \sigma_y$ or $\sigma_x > \tau_{xy}$. When transverse axial loads are dominant, i.e. when $\sigma_x < \sigma_y$, there is almost no difference between the criteria for the biaxial load cases, see Figure 5.17.

For the axial/shear load cases the FRP Sandwich plate 2 will fail due to the shear crimping local failure in most cases, see Figure 5.18, which is not satisfactory. Generally, the face wrinkling should occur in a plate significantly before the shear crimping. On the other hand, the shear crimping failure is defined to be used for compressive loads only, which is why results for when shear loads are dominant cannot be considered as being valid.

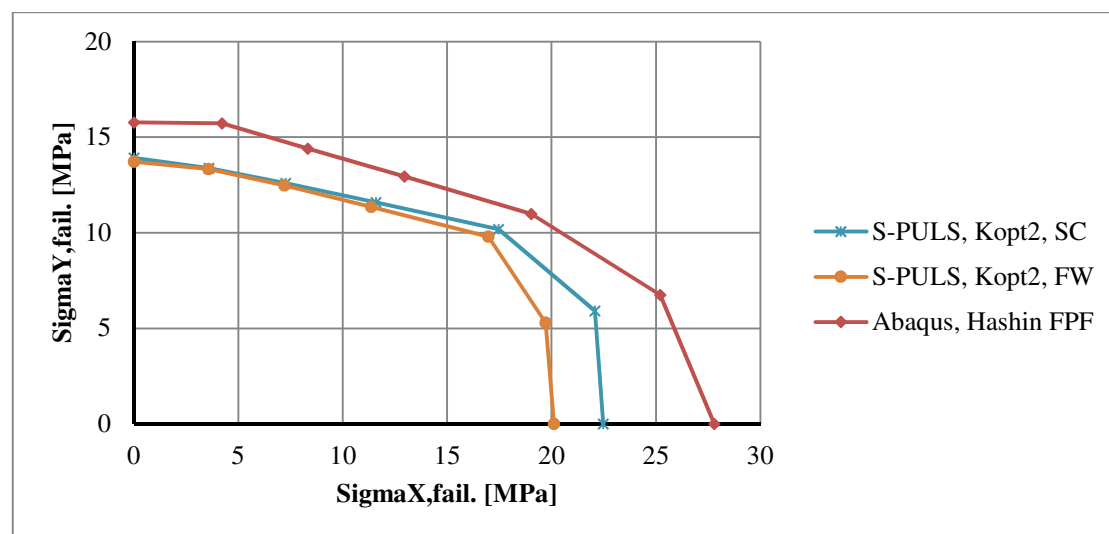


Figure 5.17 Sandwich failure initiation interaction curves for the FRP Sandwich plate 2 under biaxial loads for S-PULS with shear stiffness evaluation option 2, compared to Abaqus (Hashin FPF). SC denotes shear crimping and FW denotes face wrinkling sandwich failure.

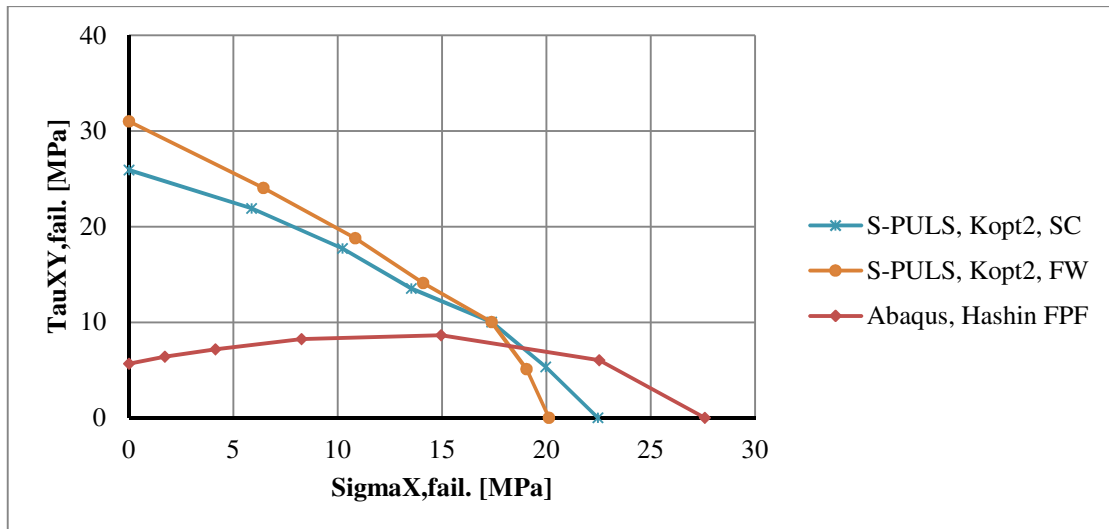


Figure 5.18 Sandwich failure initiation interaction curves for the FRP Sandwich plate 2 under axial/shear loads for S-PULS with shear stiffness evaluation option 2, compared to Abaqus (Hashin FPF). SC denotes shear crimping and FW denotes face wrinkling sandwich failure.

5.3.3 Concluding remarks

The S-PULS FPF loads according to the Hashin-Rotem failure criterion are on the conservative side, but differences compared to Abaqus are up to 40%. For the FRP Sandwich plate 2 failure is initiated before the first buckling loads. If shear strains are neglected when calculation of stresses in each ply is performed for S-PULS, predicted FPF loads show good agreement with Abaqus. Predicted failure initiation loads are then within 15%, but S-PULS is on the non-conservative side.

Face wrinkling and shear crimping critical loads are not validated, only compared to the Hashin-Rotem failure criterion. The face wrinkling and shear crimping failure criteria are formulated for uniaxial compressive loads only. When performing the sandwich failure criteria analysis for multiple interacting loads, the accuracy of results is uncertain.

5.4 Sandwich PULS sensitivity studies

This chapter presents the sensitivity studies performed in order to determine the range of accuracy of the Sandwich PULS (S-PULS) code regarding the face-to-core stiffness ratio, aspect ratio and breadth-to-thickness ratio. All sensitivity studies were performed on the FRP Sandwich plate 2 subjected to uniaxial compression.

5.4.1 Breadth-to-thickness ratio

Five cases with a different breadth-to-thickness ratio for the FRP Sandwich plate 2 were analysed in order to investigate the S-PULS sensitivity to slenderness. The analysis was performed including different shear stiffness evaluation options, see Chapter 3.3. “S-PULS, Kman” refers to Sandwich PULS with shear stiffness, which was set manually as the value predicted by Abaqus. Figure 5.19 shows the critical buckling loads obtained for different plate slenderness.

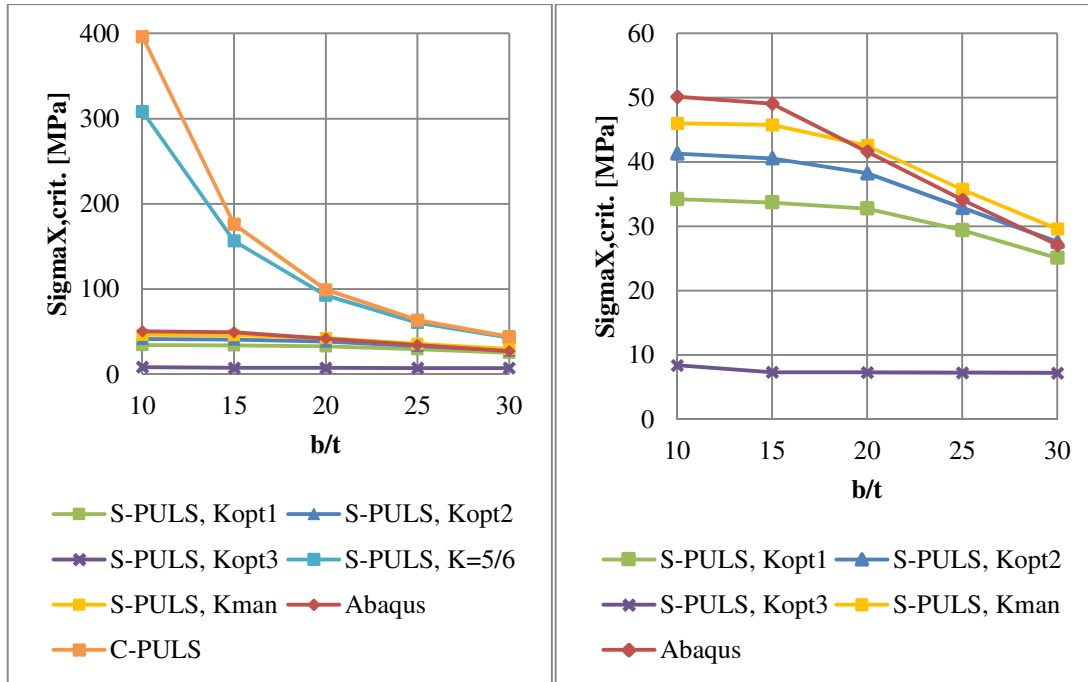


Figure 5.19 First buckling loads of the FRP Sandwich plate 2 for S-PULS with different shear stiffness evaluation options for various slenderness under uniaxial compression, validated against Abaqus and compared to (a-left), and without (b-right), C-PULS and S-PULS with $K=5/6$.

Figure 5.19a shows the difference between C-PULS, Abaqus and S-PULS with different shear stiffness evaluation options. Both C-PULS and “S-PULS, $K=5/6$ ” greatly deviate from the other cases. The deviating S-PULS curve, i.e. “S-PULS, $K=5/6$ ”, shows the major importance of choice of shear stiffness evaluation option when sandwich plates are analysed.

Figure 5.19b shows the S-PULS critical buckling loads with different shear stiffness evaluation options, which are validated against Abaqus. C-PULS and “S-PULS, $K=5/6$ ” are excluded in Figure 5.19b. “S-PULS, Kopt1” and “S-PULS, Kopt2” both show good agreement with Abaqus down to a slenderness of 20. “S-PULS, Kopt3” deviates the most from Abaqus, being over-conservative for all slenderness options. “S-PULS, Kman” shows the greatest agreement with Abaqus. An Abaqus analysis needs to be performed to set “S-PULS, Kman”, which is why it is only used for comparison and is not a valid option for implementation.

“S-PULS, Kopt1”, “S-PULS, Kopt2” and “S-PULS, Kman” agree well with Abaqus for slenderness 25 or higher. For slenderness values lower than 25 the S-PULS curves start to deviate from Abaqus, see Figure 5.19b. Using the Abaqus shell validity theory check, see Equation (4.1), slenderness 20 is just on the limit. Slenderness less than 20 does not fulfil the criterion, which is why the accuracy of the shell theory used in Abaqus cannot be guaranteed. It is believed that the plate theory used in the S-PULS code is valid for the same limits.

5.4.2 Face-to-core stiffness ratio

This chapter presents the analysis of a set of material configurations with a different face-to-core stiffness ratio. Six different face-to-core stiffness ratios, which is defined as the ratio between the shear stiffness of the faces and the shear stiffness of the core,

were used by altering the core shear stiffness. The Young's modulus of the core was scaled accordingly, while the face stiffness properties were kept constant, see Table 5.3. The material properties of the FRP Sandwich plate 2 correspond to a face-to-core shear stiffness ratio, i.e. G_f/G_c , of 120.

Table 5.3 Material properties with a face-to-core shear stiffness ratio (G_f/G_c), shear stiffness (G_c) and Young's modulus (E_c) of core are shown.

G_f/G_c	G_c [MPa]	E_c [MPa]
120	40	125
100	48	150
75	64	200
50	96	300
25	192	600
10	480	1500

Figure 5.20 shows the critical buckling loads for S-PULS and Abaqus. In Figure 5.20a it is seen that for a lower core stiffness the S-PULS results approach the Abaqus results. This is because the assumptions of the sandwich plate theory implemented in S-PULS, see Chapter 3.3, assuming strong faces and weak core, are fulfilled. For a lower face-to-core stiffness ratio, i.e. for a stronger core, the effect from shear stiffness is reduced and S-PULS and Abaqus start to approach the same solution, see Figure 5.20b.

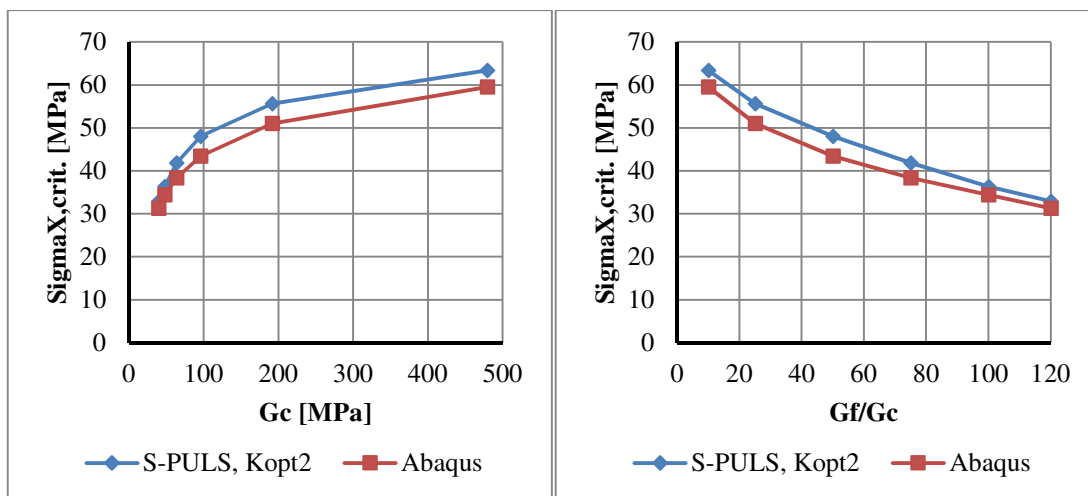


Figure 5.20 The first buckling loads under uniaxial compression for different core shear stiffness (a-left) and a face-to-core shear stiffness ratio (b-right), for the FRP Sandwich plate 2.

From Figure 5.21 to Figure 5.23 end shortening and maximum out-of-plane displacement load-displacement curves for the FRP Sandwich plate 2 with a face-to-core stiffness ratio of 10, 50 and 100 are shown. For all face-to-core stiffness ratios S-PULS agrees well with Abaqus for end shortening. For out-of-plane displacement one can see that S-PULS starts to deviate from Abaqus slightly before the critical buckling load for all stiffness ratios. The difference is believed to be caused by the difference in evaluated shear stiffness as the shear effect becomes apparent when the plate starts to deform out-of-plane.

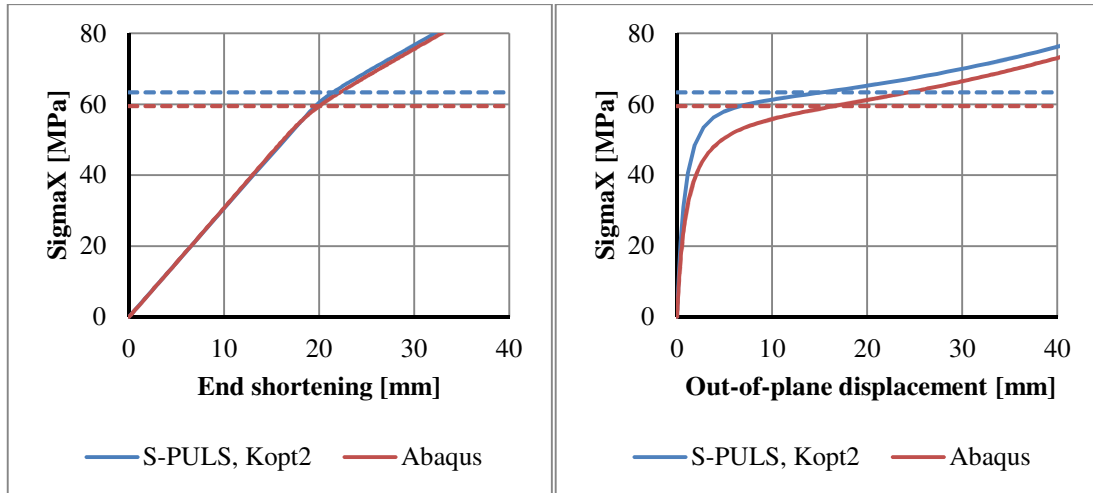


Figure 5.21 End shortening (a-left) and out-of-plane displacement (b-right) for the FRP Sandwich plate 2 with $G_f/G_c=10$ under uniaxial compression.

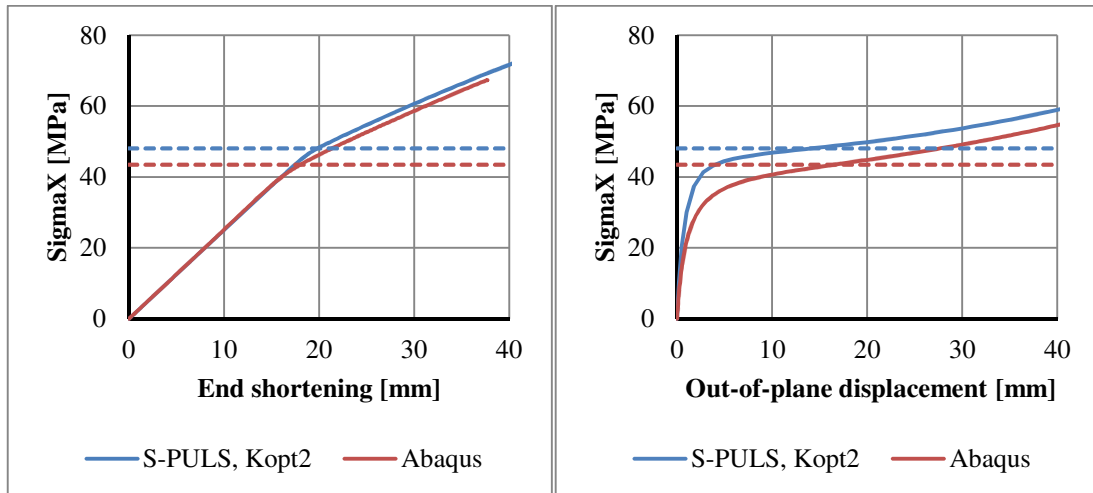


Figure 5.22 End shortening (a-left) and out-of-plane displacement (b-right) for the FRP Sandwich plate 2 with $G_f/G_c=50$ under uniaxial compression.

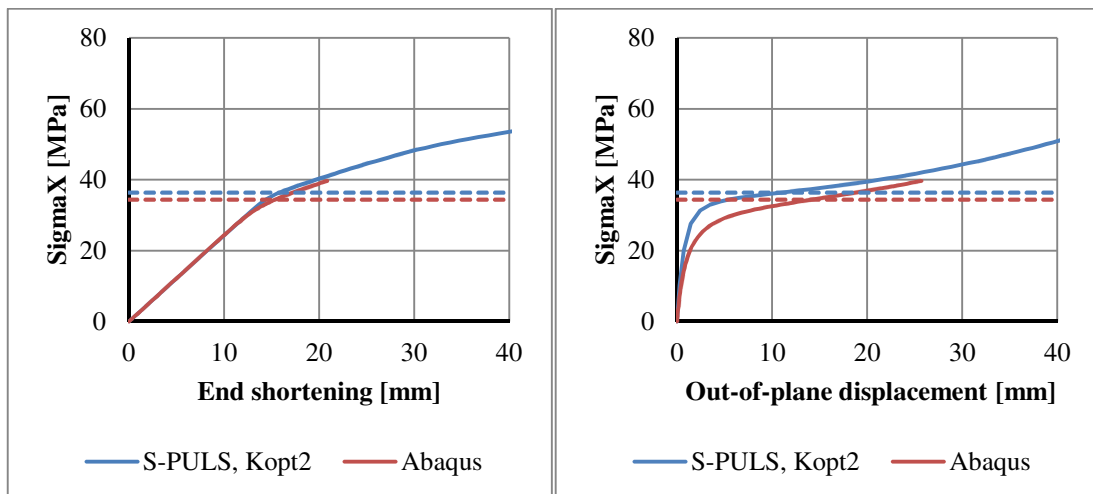


Figure 5.23 End shortening (a-left) and out-of-plane displacement (b-right) for the FRP Sandwich plate 2 with $G_f/G_c=100$ under uniaxial compression.

It can be seen in Figure 5.24 that the face-to-core stiffness ratio has little effect on the validity of S-PULS. The response due to different face-to-core stiffness is phased, lower

face-to-core stiffness ratio, i.e. stiffer core, does not influence S-PULS model response in other ways than giving a stiffer response. Different face-to-core stiffness ratios can be related to the importance of how the shear stiffness is evaluated for sandwich plates.

For a lower core stiffness, occurrence of the second buckling mode can be observed in Figure 5.24a when curves change slope for the second time, and in Figure 5.24b when curves suddenly bend upwards. By example, this occurs for $G_f/G_c=120$ at approximately 43 MPa, see Figure 5.24.

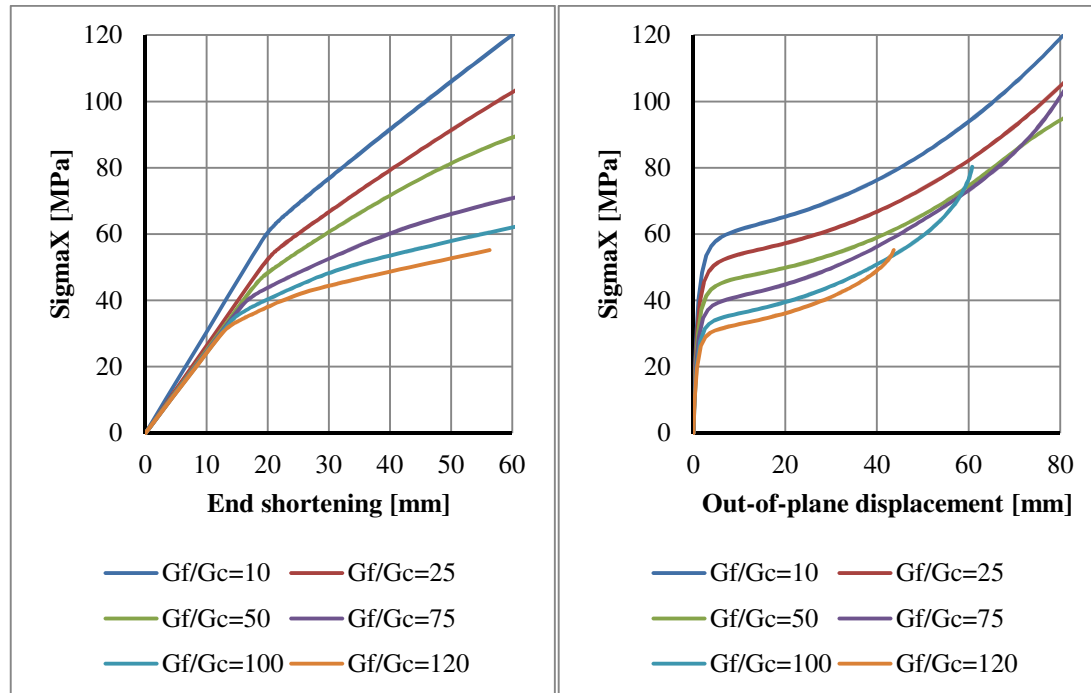


Figure 5.24 End shortening (a-left) and out-of-plane displacement (b-right) for the FRP Sandwich plate 2 with different face-to-core stiffness ratios under uniaxial compression for S-PULS.

5.4.3 Aspect ratio

The FRP Sandwich plate 2 was modelled maintaining the breadth of 900 mm, while the length was altered to obtain aspect ratios of 1, 2, 3, 4 and 5. Figure 5.25 shows the first buckling loads for S-PULS and Abaqus for different aspect ratios. The results differ most for the square plate where S-PULS and Abaqus generate different shapes of the first buckling mode. For the other aspect ratios, i.e. aspect ratios 2-5, the S-PULS and Abaqus predicted shapes of the first buckling mode are the same. For S-PULS the square plate buckles as two half-sine waves, while in Abaqus as one half-sine wave. Despite the different buckling mode shapes for aspect ratio of one, the first buckling loads for all aspect ratios predicted by “S-PULS, Kopt1” and “S-PULS, Kopt2” are within 4-7% of the Abaqus results. As before, “S-PULS, Kopt3” shows bad agreement with Abaqus being over-conservative.

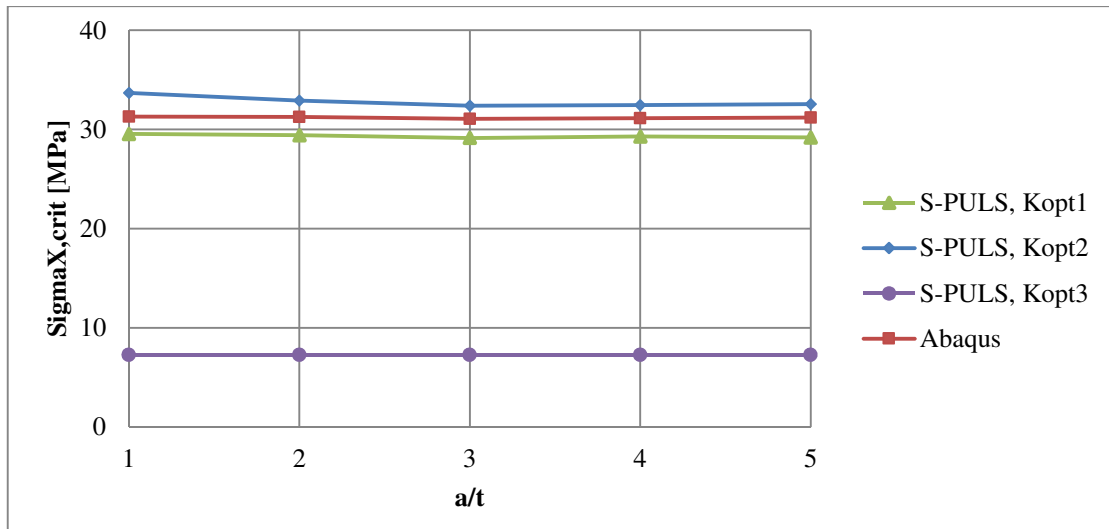


Figure 5.25 S-PULS and Abaqus first buckling loads under uniaxial compression for the FRP Sandwich plate 2 with an aspect ratio of 1-5.

In Figure 5.26, the computational times for S-PULS and Abaqus for the plates with a different aspect ratio are compared when scaled for 100 increments, in order to evaluate efficiency. It can be seen that the efficiency of S-PULS is decreased for an increasing aspect ratio. In general, S-PULS is still much faster than Abaqus.

It should be noted that pre- and post-processing are not accounted for, where Abaqus is considered to be even more time-consuming than S-PULS.

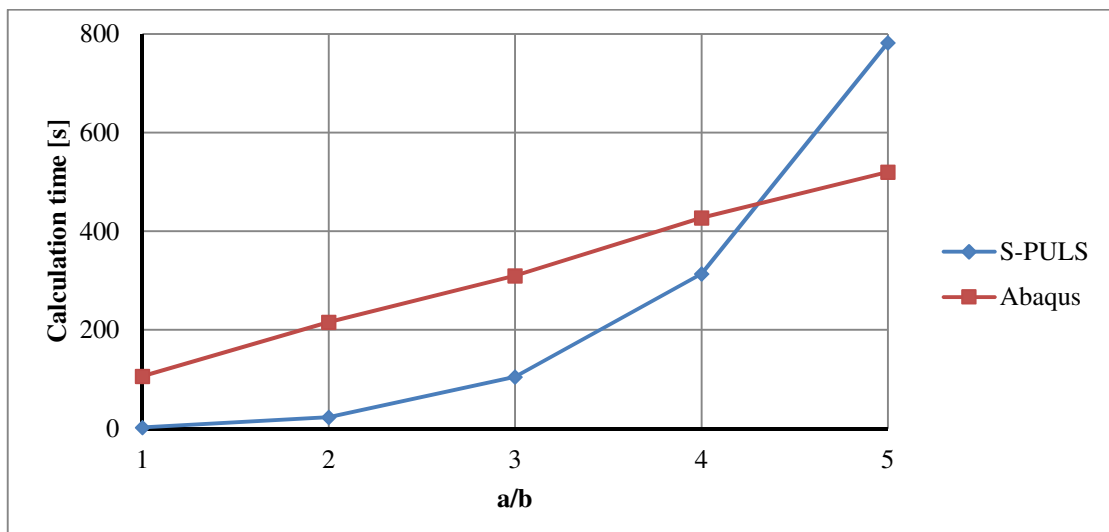


Figure 5.26 S-PULS and Abaqus calculation times for 100 increments for the FRP Sandwich plate 2 with aspect ratio of 1-5.

S-PULS calculation time increases exponentially with the aspect ratio, see Figure 5.26. This can be explained by how the number of degrees of freedom that is used for the approximated displacement fields, see Chapter 3.1, is defined in the PULS codes. Since the number of degrees of freedom in the longitudinal direction, i.e. M , is dependent on the aspect ratio, i.e. $M = DOF \cdot a/b$, the stiffness matrices, see Chapter 3.4, increase in size and more computational effort is needed to solve the problem.

Compared with C-PULS, the S-PULS calculation time is approximately 9-times longer. Due to the implemented FSDT, which makes the system of equations 9-times larger in S-PULS, see Chapter 3.4, calculation time is increased. The increase of calculation time when implementing FSDT is in accordance with the expectations presented in Chapter 3.

5.4.4 Concluding remarks

S-PULS is limited in terms of slenderness, as well as the shell theory used in Abaqus. The FRP Sandwich plate 2 with a slenderness of 25 fulfils the shell theory validity check and the S-PULS results are satisfactory. For a slenderness below 20, the physical interpretation of buckling modes is unknown and results are uncertain.

For the FRP Sandwich plate 2 with a slenderness valid for the shell theory, neither face-to-core stiffness ratio nor aspect ratio influences the quality of S-PULS results. Aspect ratio only influences calculation time, which increases exponentially with the aspect ratio. The latter can be explained by the increase in size of the stiffness matrices, which are dependent on the chosen number of degrees of freedom and thus dependent on the plate aspect ratio.

6 Conclusions

The main objective of this master's thesis project was to develop a semi-analytical method based on the Composite PULS code in order to predict the ULS capacity of sandwich plates. First-order shear deformation theory, which relaxes the Kirchhoff's assumptions used in the Composite PULS code, has been implemented in the newly developed Sandwich PULS semi-analytical computational tool.

It was concluded that in order to fully validate the Sandwich PULS code, more sandwich plate layups should be investigated. Further, the development has been limited to verification by Abaqus, lacking experimental data. It has been shown that Sandwich PULS shows good agreement with Abaqus predicting the critical buckling loads for both biaxial and combined uniaxial/in-plane shear load cases. For all inspected plates, Sandwich PULS shows improved results compared to Composite PULS. The small differences between Abaqus and Sandwich PULS are assumed to be caused by the slight difference in the evaluated shear stiffness.

For sandwich plates with thin faces and soft thick core, the sandwich plate theory, where shear stiffness of the faces is fully or partly neglected, is applicable. For this kind of plates Sandwich PULS shows good correlation with Abaqus. It was concluded that "Kopt1" or "Kopt2", should be used for the shear stiffness evaluation when sandwich plates are being analysed. It should be mentioned that Sandwich PULS evaluates shear stiffness independent on the axis direction. Implementation of a shear stiffness evaluation method that yields values dependant on the axis direction is believed to give a more realistic representation.

It has been shown that the use of only one shear correction factor for all plates does not yield satisfactory results. If $K = 5/6$ is used, the critical buckling loads are over-predicted and the predicted sandwich plate response is too stiff. For "Kopt3", results are significantly under-predicted. If the use of a uniform shear correction factor is preferred, it is believed that values between 0.4 and 0.5 are considered to give a good response for FRP Sandwich plate 2 specifically.

It was concluded that Sandwich PULS failure initiation predictions are not satisfactory. FPF loads according to Hashin-Rotem failure criteria are on the conservative side, but differences compared to Abaqus are up to 40%. Additionally, failures occur before the first buckling loads. The aim that failure predictions should be within 10% is therefore not fulfilled. Face wrinkling and shear crimping critical loads were not validated, only compared to the Hashin-Rotem failure criteria. The sandwich failure criteria predicted loads are not satisfactory and a definite conclusion cannot be given. It has been shown that a more extensive investigation of failure initiation load prediction should be performed for better understanding.

With FSDT implemented in Sandwich PULS, the displacement field is extended with additional two shear strains. Calculation time is directly dependant on the size of the matrix that needs to be solved. It has been shown that it takes approximately 9-times longer in Sandwich PULS compared with Composite PULS to perform the same analysis.

It was concluded that calculation time is very much dependent on the plate aspect ratio, which is due to an increased number of degrees of freedom that is needed for obtaining a solution. For square plates differences in calculation times between Composite PULS and Sandwich PULS can hardly be noticed, whereas for rectangular plates the calculation time increases exponentially with the aspect ratio. The Sandwich PULS

calculation time remains significantly shorter than Abaqus, even for larger aspect ratios. Pre- and post-processing times are not taken into consideration in the investigation. If so, use of Sandwich PULS would be even more advantageous in terms of time efficiency. To keep calculation time within reasonable time limits, it is recommended to use Sandwich PULS for plates with an aspect ratio of up to 3.

From the sensitivity studies performed, it was concluded that Sandwich PULS is limited in terms of slenderness. Plates should not have a slenderness below 20 in order to assure accurate solutions. Otherwise, higher order theories should be implemented in PULS, as FSDT is no longer adequate and validation by Abaqus should in that case be done by modelling sandwich plates as solids.

7 Recommendations for future work

Additional sandwich plate layups and material configurations should be investigated to get a better judgement about Sandwich PULS performance, validity and limitations in the code. Especially the part with failure initiation needs to be within the first scope of future work. Sandwich PULS could be extended first to first fibre failure or further to last ply failure. If last ply failure will be of interest, a material degradation model needs to be implemented in Sandwich PULS.

With no experimental data from tests performed for FRP Sandwich plates, preferably experiments should be performed in order to fully validate Sandwich PULS. To analyse non-symmetrical sandwich plate layups, the stretching-bending coupling matrix $[B]$ should be implemented in Sandwich PULS. Implementation of $[B]$ -matrix would be beneficial if degradation models are implemented since non-symmetrical degradation can be described. This will increase computational time even more, since two additional in-plane displacements need to be added to the displacement field when describing the buckling problem.

The difference in results between Sandwich PULS and Abaqus are mostly based on a different shear stiffness evaluation, which is why methods for evaluation of sandwich plate shear stiffness need to be further investigated. Shear correction factors should be evaluated dependent on the axis direction, i.e. evaluating K_{44} , K_{45} and K_{55} . An evaluation method based on strain energy distributions of actual shear strain and stress resultants across the cross section, could be one implementation option.

Further development of the code in terms of reducing computational time should be investigated. One way of achieving a shorter computational time would be to combine routines used for computation of the stiffness matrices. As it is now, these routines are completely separated in Sandwich PULS for the eigenvalue analysis and for the incremental solution method. Optimization of the PULS code in general should be a priority for future work.

8 References

- Agarwal, B. D., Broutman, L. J., & Chandrashekhara, K. (2006): *Analysis and Performance of Fiber Composites*, 3rd edition. John Wiley & Sons, Inc. Hoboken, New Jersey, United States.
- Allen, H. G. (1969): *Analysis and Design of Structural Sandwich Panels*. Pergamon Press, Ltd., Headington Hill Hall, Oxford, UK.
- Ashland Inc. (2011): *Technical Datasheet: DERAKANE® 8084 Epoxy Vinyl Ester Resin*. Retrieved March 5, 2015 from <http://www.ashland.com/Ashland/Static/Documents/APM/DERAKANE%208084.pdf>
- Ashton, J. E. (1969): An Analogy for Certain Anisotropic Plates. *Journal of Composite Materials*, Vol. 3, April 1969, pp. 355-358.
- Bathe, K.-J. (1996): *Finite Element Procedures*. Prentice Hall, Englewood Cliffs, New Jersey, United States.
- Birman, V., & Bert, C. W. (2002): On the Choice of Shear Correction Factor in Sandwich Structures. *Journal of Sandwich Structures and Materials*, Vol. 4, No. 1, 2002, pp. 83-95.
- Boyle, M. P., Roberts, J. C., Wienhold, P. D., Bao, G., & White, G. J. (2001): Experimental, numerical, and analytical results for buckling and post-buckling of orthotropic rectangular sandwich panels. *Composite Structures*, Vol. 52, No. 3, 2001, pp. 375-380.
- Braaten, E., & Boström, J. (2013) *Ultimate strength study of composite plates. Postbuckling analysis using semi-analytical methods*. MSc thesis. Chalmers University of Technology, Department of Shipping and Marine Technology, Division of Marine Design, Research Group Marine Structures, Göteborg, Sweden.
- Byklum, E. (2002): *Ultimate strength analysis of stiffened steel and aluminium panels using semi-analytical methods*. PhD thesis. Norwegian University of Science and Technology, Faculty of Engineering Sciences and Technology, Department of Marine Technology, Trondheim, Norway.
- Byklum, E., & Amdahl, J. (2002): *Nonlinear buckling Analysis and ultimate Strength Prediction of Stiffened Steel and Aluminium Panels*. In Proceedings of the 2nd International Conference on Advances in Structural Engineering and Mechanics, Busan, Korea, August 21-23, 2002.
- Carrera, E., & Brischetto, S. (2009): A Survey with Numerical Assessment of Classical and Refined Theories for the Analysis of Sandwich Plates. *Applied Mechanics Reviews*, Vol. 62, No. 1, 2009, 17 pp.
- Chia, C. Y., & Prabhakara, M. K. (1975): Nonlinear analysis of orthotropic plates. *Journal of Mechanical Engineering Science*, Vol. 17, No. 3, 1975, 6 pp.
- Cook, R. D., Malkus, D. S., Plesha, M. E., & Witt, R. J. (2002): *Concepts and applications of finite element analysis*, 4th edition. John Wiley & Sons, Inc. Hoboken, New Jersey, United States.
- Dassault Systèmes [Abaqus] (2014): *Abaqus version 6.14 Documentation*. User's manual. Dassault Systèmes Simulia Corp., Providence, Rhode Island, USA.

- DNV (2013): Hull Structural Design, Fibre Composite and Sandwich Constructions. *High Speed, Light Craft and Naval Surface Craft*, Part 3, Chapter 4, January 2013.
- Evegren, F., Hertzberg, T., & Rahm, M. (2011): *LASS-C: Lightweight construction of a cruise vessel*. Report. SP Technical Research Institute of Sweden, 12, Borås, Sweden.
- Hareide, O. J. (2012): *Analytical and semi-analytical methods for buckling and bending of steel elastomer sandwich plates*. Faculty of Mathematics and Natural Sciences, University of Oslo, Oslo, Norway.
- Hareide, O. J. (2014): *Buckling of composite plates using a semi-analytical approach*. In Proceedings of the 27th Nordic Seminar on Computational Mechanics (NSCM-27), KTH, Stockholm, Sweden, October 22-24, 2014.
- Harris, B. J., & Crisman, W. C. (1965): Face-wrinkling mode of buckling of sandwich panels. *Journal of Engineering Mechanics Division, Proceedings ASCE*, 91, pp. 93-111.
- Hashin, Z. (1980): Failure Criteria for Unidirectional Fiber Composites. *Journal of Applied Mechanics*, Vol. 47, June 1980, pp. 448-464.
- Hashin, Z., & Rotem, A. (1973): A Fatigue Failure Criterion for Fiber Reinforced Materials. *Journal of Composite Materials*, Vol. 7, October 1973, pp. 329-334.
- Hayman, B., Berggreen, C., Lundsgaard-Larsen, C., Delarche, A., Toftegaard, H., Dowd, R. S., & Doukae, C. (2011): Studies of the buckling of composite plates in compression. *Ships and Offshore Structures*, Vol. 6, No. 1-2, 2011, pp. 81-92.
- Hollaway, L. C., & Head, P. R. (2001): *Advanced Polymer Composites and Polymers in the Civil Infrastructure*. Elsevier Science Ltd., Oxford, UK, 2001, Ch. 4, pp. 89-106.
- IMO (2004): *SOLAS. Consolidated Edition, 2004*. International Maritime Organization, 4 Albert Embankment, London, UK.
- Intelligent Engineering Ltd. (2015): *SPS: the Sandwich Plate System. Its use in new vessels*. Retrieved May 18, 2015 from <http://www.ie-sps.com/Overview.html?sku=254>
- Job, S. (2015): Why not composites in ships? *Reinforced Plastics*, Vol. 59, No. 2, 2015, pp. 90-93.
- Juska, T., Mayes, J. S., & Seemann III, W. H. (1993): *Mechanical Properties and Impact Damage Resistance of Composites Fabricated by Low Cost, Vacuum Assisted, Resin Transfer Molding*. Research and Development Report. Naval Surface Warfare Center, Carderock Division, Bethesda, Maryland, United States.
- Marsh, G. (2006): 50 years of reinforced plastic boats. *Reinforced Plastics*, Vol. 50, No. 9, 2006, pp. 16-19.
- MatWeb (2015 a): *DIAB Divinycell® HT 70 Interpenetrating Polymer Network Foam Core Material*. Retrieved March 5, 2015 from <http://www.matweb.com/search/datasheet.aspx?matguid=9a1a64538096477a926f3caf0ab5d9b8>
- MatWeb (2015 b): *DIAB Divinycell® H 100 Semi-rigid PVC Foam Core Material*. Retrieved March 25, 2015 from <http://www.matweb.com/search/datasheet.aspx?matguid=0872e8bd246246aaa7e3c5f6edd892d9&ckck=1>

- Misirilis, K. (2012): *Progressive Collapse Analysis of Composite Ship Hull Sections*. PhD thesis. School of Marine Science and Technology, Faculty of Science, Agriculture and Engineering, Newcastle University, Newcastle upon Tyne, UK.
- Reddy, J. N. (2004): *Mechanics of Laminated Composite Plates and Shell. Theory and Analysis, 2nd edition*. CRC Press, LLC, Boca Raton.
- Steen, E. (1998): *Application of the Perturbation Method to Plate Buckling Problem*. Research report in Mechanics, No. 98-1. University of Oslo, Department of Mathematics, Mechanics division, Oslo, Norway.
- Steen, E., & Byklum, E. (2005): *Ultimate strength and postbuckling stiffness of plate panels subjected to combined loads using semi-analytical models*. In Proceedings of the International Conference on Marine Research and Transport (ICMRT 2005), Naples, Italy, September 19-21, 2005.
- Steen, E., Byklum, E., Vilming, K. G., & Østvold, T. K. (2004): *Computerized buckling models for ultimate strength assessments of stiffened ship hull panels*. In Proceedings of the 9th international symposium on Practical design of ships and other floating structures (PRADS 2004), Lübeck-Travemünde, Germany, 2004.
- Sullins, R. T., Smith, G. W., & Spier, E. E. (1969): *Manual for Structural Stability Analysis of Sandwich Plates and Shells*. NASA, Washington, United States.
- Turvey, G. J., & Marshall, I. H. (1995): *Buckling and Postbuckling of Composite Plates*. Chapman and Hall, London, UK.
- Yang, Q. J. (2014): *Semi-analytical models for predicting post-buckling response and ultimate strength of imperfect composite plates*. PhD thesis. University of Oslo, Faculty of Mathematics and Natural Sciences, Department of Mathematics, Mechanics Division, Oslo, Norway.
- Yoo, C. H., & Lee, S. C. (2011): *Stability of Structures: Principles and Applications*. Butterworth-Heinemann, Burlington, Massachusetts, United States.
- Zenkert, D. (1997): *Sandwich Construction*. EMAS Publishing, UK.
- Zenkert, D. (2005): *An Introduction to Sandwich Structures, Student Edition*. Dan Zenkert, The Royal Institute of Technology, Stockholm, Sweden.

Appendix A – Material data

All material data for the plates that has been used in this thesis is presented here. The SPS plate (Chapter A.1), single-skin FRP composite plate (Chapter A.2) and FRP Sandwich plate 1 (Chapter A.3) were only used as validation for the eigenvalue and load-displacement analyses during the implementation process. The FRP Sandwich plate 2 (Chapter A.4) was used in the eigenvalue analysis, the load-displacement analysis and the failure initiation analysis to give final evaluation of the Sandwich PULS code.

A.1 Sandwich Plate System (SPS)

The Sandwich Plate System (SPS) consists of thin steel faces and thick polyurethane elastomer core. The SPS has been used in shipbuilding due to its many advantages compared with conventional structures, such as:

- improved corrosion and fatigue performance,
- better strength-to-weight ratio,
- increased impact, blast and ballistic resistance,
- vibration damping and acoustic insulation,
- built-in fire protection.

Figure A.1a shows SPS layup and Figure A.1b shows an example of the difference between a conventional steel structure and a SPS structure.

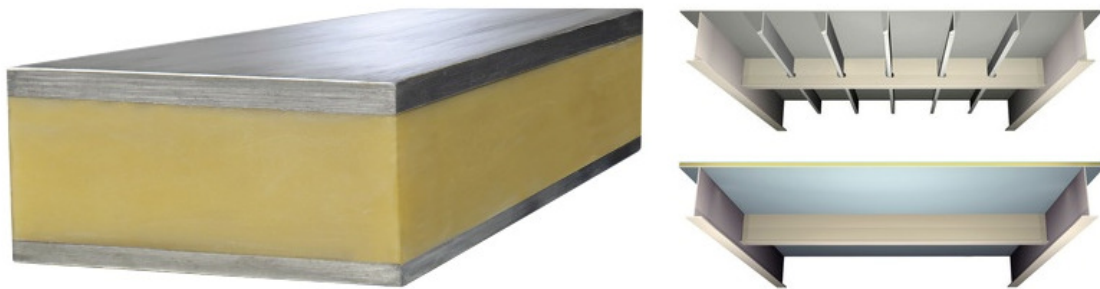


Figure A.1 Layup of the Sandwich Plate System (SPS) (a-left), a conventional stiffened steel (b-top right) and a SPS structure (b-bottom right), from Intelligent Engineering Ltd. (2015).

Plate dimensions are:

$$a = 2970 \text{ mm}$$

$$b = 990 \text{ mm}$$

$$t_{f1} = t_{f2} = 4 \text{ mm}$$

$$t_c = 25 \text{ mm}$$

$$a / b = 3.0$$

$$b / t = 30.0$$

Steel faces material properties are equal to:

$$E_f = 208 \text{ GPa}$$

$$\nu_f = 0.30$$

Elastomer core material properties are equal to, from Hareide (2014):

$$E_c = 0.75 \text{ GPa}$$

$$\nu_c = 0.30$$

It should be noted that a sandwich plate with thin faces, weak core and the fact that the shear modulus of the faces is large is assumed for this case. SPS shear stiffness matrix is evaluated according to Zenkert (1997) as:

$$A_{44} = A_{55} = \frac{G_c d^2}{t_c} = \frac{G_c \left(\frac{t_{f1}}{2} + t_c + \frac{t_{f2}}{2} \right)^2}{t_c}$$

$$A_{45} = A_{54} = 0$$

A.2 Single-skin FRP Composite plate

A single-skin FRP Composite plate with a quadriaxial layup $[0_3/+45/90/-45]_{2s}$ is used in the validation process.

Plate dimensions are:

$$a = 1920 \text{ mm}$$

$$b = 480 \text{ mm}$$

$$t_{plate} = 24 \text{ mm}$$

$$a/b = 4.0$$

$$b/t = 20.0$$

FRP material properties are:

$$E_L = 49627 \text{ MPa}$$

$$E_T = 15430 \text{ MPa}$$

$$G_{LT} = G_{LT'} = G_{TT'} = G = 4800 \text{ MPa}$$

$$\nu_{LT} = 0.27$$

The single-skin FRP Composite shear stiffness matrix is evaluated according to Agarwal et al. (2006) as:

$$A_{44} = A_{55} = K G t_{total} = \frac{5}{6} G t_{total}$$

$$A_{45} = A_{54} = 0$$

A.3 FRP Sandwich plate 1

The FRP Sandwich plate 1 used in the validation process has similar material properties as investigated plates in Boyle et al. (2001) in order to be able to recreate and compare their results.

Plate dimensions are:

$$a = 1840 \text{ mm}$$

$$b = 920 \text{ mm}$$

$$t_{plate} = 19.1 \text{ mm}$$

$$t_{f1} = t_{f2} = 3.2 \text{ mm}$$

$$t_c = 12.7 \text{ mm}$$

$$a / b = 2.0$$

$$b / t = 48.2$$

FRP faces material properties: Certainteed/Seemann 625 E-glass woven roving (225 yd/lb), from Juska et al. (1993), Derakane 8084 vinyl ester resin, from Ashland Inc. (2011):

$$\text{Layup: } [0_4]_s$$

$$t_{ply} = 0.8 \text{ mm}$$

$$n_{ply} / \text{face} = 4$$

$$E_L = 24.1 \text{ GPa}$$

$$E_T = 24.1 \text{ GPa}$$

$$G_{LT} = G_{LT'} = G_{TT'} = G = 3.65 \text{ GPa}$$

$$\nu_{LT} = 0.115$$

$$\nu_{LT'} = \nu_{TT'} = 0.331$$

$$X_{C,FRP} = Y_{C,FRP} = 331.0 \text{ MPa}$$

$$X_{T,FRP} = Y_{T,FRP} = 351.6 \text{ MPa}$$

$$S_{FRP} = 36.2 \text{ MPa}$$

Core material properties: Divinycell HT-70 PVC foam, from Boyle et al. (2001) and MatWeb (2015 a):

$$E_c = 0.896 \text{ GPa}$$

$$G_c = 0.393 \text{ GPa}$$

$$\nu = 0.15$$

$$X_{C,foam} = Y_{C,foam} = 1.15 \text{ MPa}$$

$$X_{T,foam} = Y_{T,foam} = 2.1 \text{ MPa}$$

$$S_{foam} = 0.9 \text{ MPa}$$

A sandwich plate with thin faces, weak core and with a large shear modulus of the faces compared to the core shear modulus can be evaluated according to Zenkert (1997). FRP Sandwich plate 1 shear stiffness matrix is then evaluated as:

$$A_{44} = A_{55} = G_c t_c$$

$$A_{45} = A_{54} = 0$$

A.4 FRP Sandwich plate 2

The FRP Sandwich plate 2 used in the validation process and failure analysis has the following properties:

Plate dimensions are:

$$a = 1800 \text{ mm}$$

$$b = 900 \text{ mm}$$

$$t_{plate} = 36 \text{ mm}$$

$$t_{f1} = t_{f2} = 3 \text{ mm}$$

$$t_c = 30 \text{ mm}$$

$$a / b = 2$$

$$b / t = 25$$

FRP faces material properties: Pre-preg E-glass fibre/epoxy, from Hayman (2011):

Layup: $[0/-45/+45/90]_s$

$$t_{ply} = 0.75 \text{ mm}$$

$$n_{ply} / \text{face} = 4$$

$$E_L = 49627 \text{ MPa}$$

$$E_T = 15430 \text{ MPa}$$

$$X_{C,FRP} = 915 \text{ MPa}$$

$$X_{T,FRP} = 968 \text{ MPa}$$

$$Y_{C,FRP} = 118 \text{ MPa}$$

$$Y_{T,FRP} = 24 \text{ MPa}$$

$$S_{FRP} = 65 \text{ MPa}$$

Core material properties: Divinycell H 100 Semi-rigid PVC foam, from MatWeb (2015 b):

$$E_c = 125 \text{ MPa}$$

$$G_c = 40 \text{ MPa}$$

$$\nu = 0.32$$

$$X_{C,foam} = Y_{C,foam} = 3.1 \text{ MPa}$$

$$X_{T,foam} = Y_{T,foam} = 1.7 \text{ MPa}$$

$$S_{foam} = 1.4 \text{ MPa}$$

Appendix B – First-order shear deformation theory

The classical laminate plate theory (CLT) or better known as the Kirchhoff plate theory is only valid for thin plates, for which shear deformations can be neglected. This is not the case for sandwich plates, which are usually considered as thick plates, and shear deformations thus need to be accounted for. In this thesis, the Mindlin-Reissner or the first-order shear deformation plate theory (FSDT) has been chosen for the implementation in the Sandwich PULS code. The chapter is summarized and adopted from Reddy (2004) and Agarwal et al. (2006).

The first-order shear deformation plate theory is an extension of the Kirchhoff plate theory. The kinematic assumptions of the Kirchhoff plate theory, as found in Reddy (2004) and seen in Figure B.1, are:

- Straight lines perpendicular to the mid-surface (i.e. transverse normals) before deformation remain straight after deformation.
- The transverse normals do not experience elongation - they are inextensible (i.e. thickness of a plate does not change during a deformation).
- The transverse normals rotate in such a way that they remain perpendicular to the mid-plane after deformation.

The first two assumptions imply that the transverse displacement is independent of the thickness and that the transverse normal strain ϵ_{zz} is zero. The third assumption shows that the transverse shear strains are zero, i.e. $\epsilon_{xz} = \epsilon_{yz} = 0$.

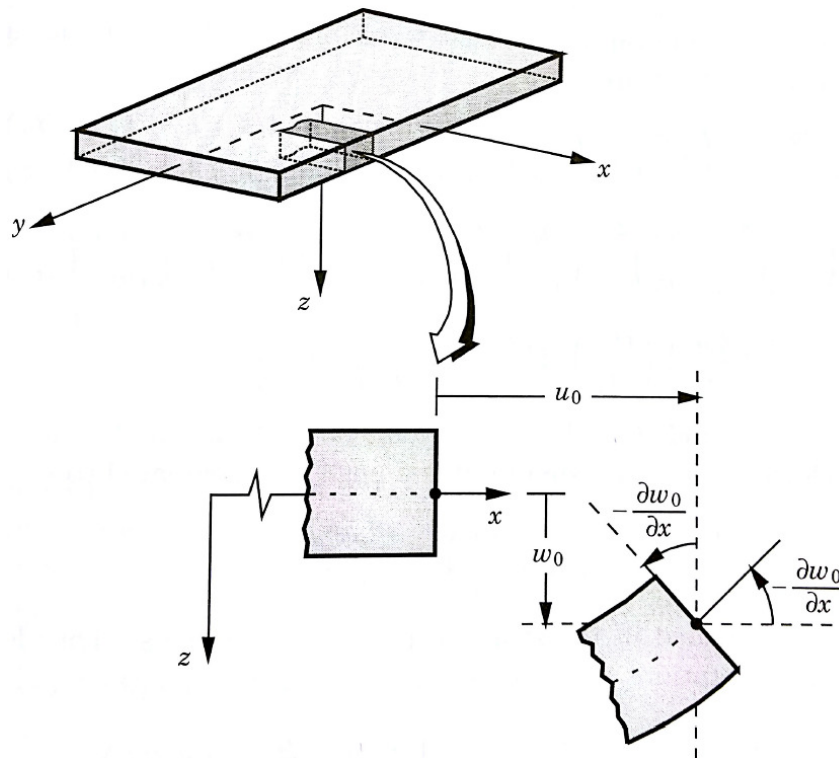


Figure B.1 Undeformed and deformed geometries of an edge of a plate under the Kirchhoff assumptions, from Reddy (2014).

When formulating the laminate plate theory, additional assumptions or restrictions should be added to the initial Kirchhoff's assumptions:

- The layers are perfectly bonded together.
- The material of each layer is linearly elastic and has three planes of material symmetry, i.e. orthotropic.
- Each layer is of uniform thickness.
- The strains and displacements are small.
- The transverse shear stresses on the top and bottom surfaces of the laminate are zero.

It should be pointed out that these assumptions are only valid for thin plates, where shear deformations are rather small and can therefore be neglected. With thick plates in mind, the first-order shear deformation plate theory was established, which relaxes the third Kirchhoff assumption in a way that the transverse normals can freely rotate but are still to remain straight after a deformation, as seen in Figure B.2. As a consequence of this relaxation, transverse shear strains need to be included in the strain field.

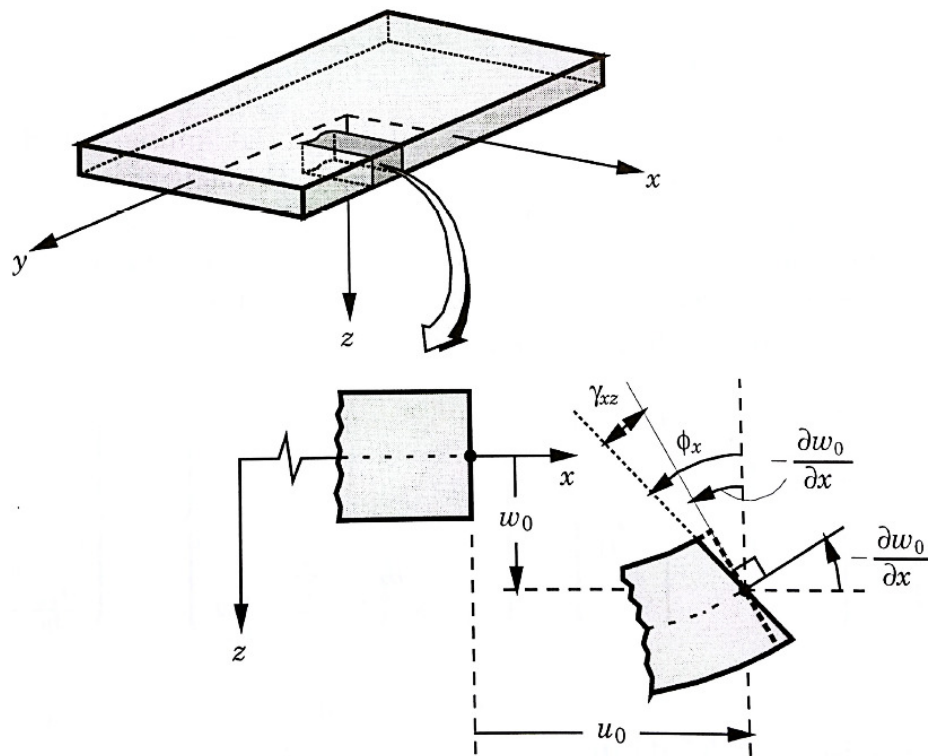


Figure B.2 Undeformed and deformed geometries of an edge of a plate under the assumptions of the first-order shear deformation plate theory, from Reddy (2014).

According to FSDT a displacement of a point in a plate can be defined as:

$$u(x, y, z) = u_0(x, y) + z\phi_x(x, y) \quad [\text{mm}] \quad (\text{B.1a})$$

$$v(x, y, z) = v_0(x, y) + z\phi_y(x, y) \quad [\text{mm}] \quad (\text{B.1b})$$

$$w(x, y) = w_0(x, y) \quad [\text{mm}] \quad (\text{B.1c})$$

The actual cross-sectional rotations, i.e. ϕ_x and ϕ_y , are obtained by differentiating the in-plane displacement field, as shown in Equations (B.2a) and (B.2b).

$$\phi_x = \frac{\partial u}{\partial z} \quad [-] \quad (\text{B.2a})$$

$$\phi_y = \frac{\partial v}{\partial z} \quad [-] \quad (\text{B.2b})$$

The strain-displacement relation can be divided into the mid-plane strains, i.e. membrane strains, and the plate curvatures as follows:

$$\{\boldsymbol{\varepsilon}\} = \begin{Bmatrix} \boldsymbol{\varepsilon}_x \\ \boldsymbol{\varepsilon}_y \\ \boldsymbol{\gamma}_{xy} \end{Bmatrix} = \begin{Bmatrix} \boldsymbol{\varepsilon}_x^0 \\ \boldsymbol{\varepsilon}_y^0 \\ \boldsymbol{\gamma}_{xy}^0 \end{Bmatrix} + z \begin{Bmatrix} k_x \\ k_y \\ k_{xy} \end{Bmatrix} \quad [-] \quad (\text{B.3})$$

where the mid-plane strains are:

$$\{\boldsymbol{\varepsilon}_0\} = \begin{Bmatrix} \boldsymbol{\varepsilon}_x^0 \\ \boldsymbol{\varepsilon}_y^0 \\ \boldsymbol{\gamma}_{xy}^0 \end{Bmatrix} = \begin{Bmatrix} \frac{\partial u_0}{\partial x} \\ \frac{\partial v_0}{\partial y} \\ \frac{\partial u_0}{\partial y} + \frac{\partial v_0}{\partial x} \end{Bmatrix} \quad [-] \quad (\text{B.4})$$

and the plate curvatures for FSDT are:

$$\{\boldsymbol{\kappa}\} = \begin{Bmatrix} k_x \\ k_y \\ k_{xy} \end{Bmatrix} = \begin{Bmatrix} \frac{\partial \phi_x}{\partial x} \\ \frac{\partial \phi_y}{\partial y} \\ \frac{\partial \phi_x}{\partial y} + \frac{\partial \phi_y}{\partial x} \end{Bmatrix} = \begin{Bmatrix} \frac{\partial^2 w}{\partial x^2} - \frac{\partial \gamma_{xz}}{\partial x} \\ \frac{\partial^2 w}{\partial y^2} - \frac{\partial \gamma_{yz}}{\partial y} \\ 2 \frac{\partial^2 w}{\partial x \partial y} - \frac{\partial \gamma_{xz}}{\partial y} - \frac{\partial \gamma_{yz}}{\partial x} \end{Bmatrix} \quad [-/\text{mm}] \quad (\text{B.5})$$

Appendix C – Anisotropic plate theory

This chapter presents plate theories for anisotropic plates based theories presented in Agarwal et al. (2006) and Reddy (2004).

The stress-strain relation can be rewritten for a lamina as follows:

$$\begin{aligned} \begin{Bmatrix} \sigma_x \\ \sigma_y \\ \tau_{xy} \end{Bmatrix}_k &= [T_1]_k^{-1} \begin{bmatrix} Q_{11} & Q_{12} & 0 \\ Q_{12} & Q_{22} & 0 \\ 0 & 0 & Q_{66} \end{bmatrix} [T_2]_k \begin{Bmatrix} \varepsilon_x \\ \varepsilon_y \\ \gamma_{xy} \end{Bmatrix} = \\ &= \begin{bmatrix} \overline{Q}_{11} & \overline{Q}_{12} & \overline{Q}_{16} \\ \overline{Q}_{12} & \overline{Q}_{22} & \overline{Q}_{26} \\ \overline{Q}_{16} & \overline{Q}_{26} & \overline{Q}_{66} \end{bmatrix}_k \begin{Bmatrix} \varepsilon_x \\ \varepsilon_y \\ \gamma_{xy} \end{Bmatrix} \quad [\text{MPa}] \end{aligned} \quad (\text{C.1})$$

Where $[T_1]^{-1}$ and $[T_2]$ in Equation (C.1) are inverse of the stress-transformation matrix and strain-transformation matrix defined for each lamina with ply orientation angle θ as:

$$[T_1]^{-1} = \begin{bmatrix} \cos^2 \theta & \sin^2 \theta & -2 \sin \theta \cos \theta \\ \sin^2 \theta & \cos^2 \theta & 2 \sin \theta \cos \theta \\ \sin \theta \cos \theta & -\sin \theta \cos \theta & \cos^2 \theta - \sin^2 \theta \end{bmatrix} \quad [-] \quad (\text{C.2})$$

$$[T_2] = \begin{bmatrix} \cos^2 \theta & \sin^2 \theta & \sin \theta \cos \theta \\ \sin^2 \theta & \cos^2 \theta & -\sin \theta \cos \theta \\ -2 \sin \theta \cos \theta & 2 \sin \theta \cos \theta & \cos^2 \theta - \sin^2 \theta \end{bmatrix} \quad [-] \quad (\text{C.3})$$

Resultant forces and moments acting on a laminate cross section are obtained by integrating the corresponding stress through the laminate thickness h (for resultant forces) and multiplying with the moment arm with respect to the mid-plane (for resultant moments):

$$\begin{Bmatrix} N_x \\ N_y \\ N_{xy} \end{Bmatrix} = \int_{-h/2}^{h/2} \begin{Bmatrix} \sigma_x \\ \sigma_y \\ \tau_{xy} \end{Bmatrix} dz = \sum_{k=1}^n \int_{h_{k-1}}^{h_k} \begin{Bmatrix} \sigma_x \\ \sigma_y \\ \tau_{xy} \end{Bmatrix}_k dz \quad [\text{N/mm}] \quad (\text{C.4})$$

$$\begin{Bmatrix} M_x \\ M_y \\ M_{xy} \end{Bmatrix} = \int_{-h/2}^{h/2} \begin{Bmatrix} \sigma_x \\ \sigma_y \\ \tau_{xy} \end{Bmatrix} z dz = \sum_{k=1}^n \int_{h_{k-1}}^{h_k} \begin{Bmatrix} \sigma_x \\ \sigma_y \\ \tau_{xy} \end{Bmatrix}_k z dz \quad [\text{N}] \quad (\text{C.5})$$

After inserting Equation (B.3) into Equations (C.4) and (C.5) the following relation is obtained:

$$\begin{aligned} \begin{Bmatrix} N_x \\ N_y \\ N_{xy} \end{Bmatrix} &= \sum_{k=1}^n \left\{ \int_{h_{k-1}}^{h_k} [\bar{Q}]_k \{\varepsilon_0\} dz + \int_{h_{k-1}}^{h_k} [\bar{Q}]_k \{\kappa\} z dz \right\} = \\ &= \left[\sum_{k=1}^n [\bar{Q}]_k \int_{h_{k-1}}^{h_k} dz \right] \{\varepsilon_0\} + \left[\sum_{k=1}^n [\bar{Q}]_k \int_{h_{k-1}}^{h_k} z dz \right] \{\kappa\} \end{aligned} \quad [\text{N/mm}] \quad (\text{C.6})$$

$$\begin{aligned} \begin{Bmatrix} M_x \\ M_y \\ M_{xy} \end{Bmatrix} &= \sum_{k=1}^n \left\{ \int_{h_{k-1}}^{h_k} [\bar{Q}]_k \{\varepsilon_0\} z dz + \int_{h_{k-1}}^{h_k} [\bar{Q}]_k \{\kappa\} z^2 dz \right\} = \\ &= \left[\sum_{k=1}^n [\bar{Q}]_k \int_{h_{k-1}}^{h_k} z dz \right] \{\varepsilon_0\} + \left[\sum_{k=1}^n [\bar{Q}]_k \int_{h_{k-1}}^{h_k} z^2 dz \right] \{\kappa\} \end{aligned} \quad [\text{N}] \quad (\text{C.7})$$

Three new matrices can be defined and Equations (C.6) and (C.7) can be rewritten as:

$$\begin{Bmatrix} N_x \\ N_y \\ N_{xy} \end{Bmatrix} = \begin{bmatrix} A_{11} & A_{12} & A_{16} \\ A_{12} & A_{22} & A_{26} \\ A_{16} & A_{26} & A_{66} \end{bmatrix} \begin{Bmatrix} \varepsilon_x^0 \\ \varepsilon_y^0 \\ \gamma_{xy}^0 \end{Bmatrix} + \begin{bmatrix} B_{11} & B_{12} & B_{16} \\ B_{12} & B_{22} & B_{26} \\ B_{16} & B_{26} & B_{66} \end{bmatrix} \begin{Bmatrix} k_x \\ k_y \\ k_{xy} \end{Bmatrix} \quad [\text{N/mm}] \quad (\text{C.8})$$

$$\begin{Bmatrix} M_x \\ M_y \\ M_{xy} \end{Bmatrix} = \begin{bmatrix} B_{11} & B_{12} & B_{16} \\ B_{12} & B_{22} & B_{26} \\ B_{16} & B_{26} & B_{66} \end{bmatrix} \begin{Bmatrix} \varepsilon_x^0 \\ \varepsilon_y^0 \\ \gamma_{xy}^0 \end{Bmatrix} + \begin{bmatrix} D_{11} & D_{12} & D_{16} \\ D_{12} & D_{22} & D_{26} \\ D_{16} & D_{26} & D_{66} \end{bmatrix} \begin{Bmatrix} k_x \\ k_y \\ k_{xy} \end{Bmatrix} \quad [\text{N}] \quad (\text{C.9})$$

Where the extensional stiffness matrix $[A]$, the stretching-bending coupling stiffness matrix $[B]$ and bending stiffness matrix $[D]$ are defined as follows:

$$[A] = \begin{bmatrix} A_{11} & A_{12} & A_{16} \\ A_{12} & A_{22} & A_{26} \\ A_{16} & A_{26} & A_{66} \end{bmatrix} = \sum_{k=1}^n [\bar{Q}]_k (h_k - h_{k-1}) \quad [\text{N/mm}] \quad (\text{C.10})$$

$$[B] = \begin{bmatrix} B_{11} & B_{12} & B_{16} \\ B_{12} & B_{22} & B_{26} \\ B_{16} & B_{26} & B_{66} \end{bmatrix} = \sum_{k=1}^n [\bar{Q}]_k (h_k^2 - h_{k-1}^2) \quad [\text{N}] \quad (\text{C.11})$$

$$[D] = \begin{bmatrix} D_{11} & D_{12} & D_{16} \\ D_{12} & D_{22} & D_{26} \\ D_{16} & D_{26} & D_{66} \end{bmatrix} = \sum_{k=1}^n [\bar{Q}]_k (h_k^3 - h_{k-1}^3) \quad [\text{Nmm}] \quad (\text{C.12})$$

Combining Equations (C.8) and (C.9) with Equations (C.10)-(C.12) one can rewrite the total plate constitutive equation in a relatively simple form as follows:

$$\begin{Bmatrix} N \\ M \end{Bmatrix} = \begin{bmatrix} A & B \\ B & D \end{bmatrix} \begin{Bmatrix} \epsilon_0 \\ \kappa \end{Bmatrix} \quad [\text{N/mm or N}] \quad (\text{C.13})$$

According to FSDT, shear stresses are not equal to zero. It is assumed that the transverse shear strains are constant through the laminate thickness. As a consequence of this assumption the shear stresses must be constant as well. However, this is not the case with plates in reality, where the shear stresses follow square function through the plate thickness, see Figure C.1. Therefore, the shear correction factor (K) has to be used to compensate for this assumption, as is shown in Equation (C.16).

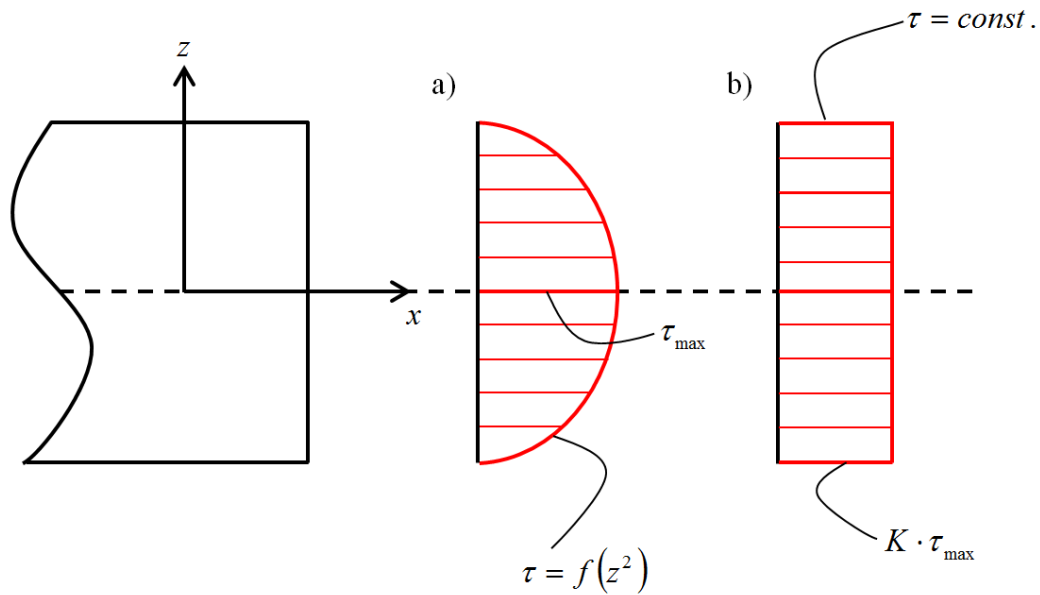


Figure C.1 The shear stress distribution through the plate thickness as in reality (a) and after compensated for a parameter K (b).

Shear stresses can be obtained on a lamina level as:

$$\begin{aligned} \{\tau\}_k &= \begin{Bmatrix} \tau_{yz} \\ \tau_{xz} \end{Bmatrix}_k = [\tilde{T}_1]^{-1} \begin{bmatrix} Q_{44} & Q_{45} \\ Q_{45} & Q_{55} \end{bmatrix}_k [\tilde{T}_1] = \\ &= \begin{bmatrix} \bar{Q}_{44} & \bar{Q}_{45} \\ \bar{Q}_{45} & \bar{Q}_{55} \end{bmatrix}_k \begin{Bmatrix} \gamma_{yz} \\ \gamma_{xz} \end{Bmatrix} = [\bar{Q}]_{shear,k} \{\gamma\} \end{aligned} \quad [\text{MPa}] \quad (\text{C.14})$$

Where $[\tilde{T}_1]$ is the rotational matrix, which is used for shear stress- and shear strain-transformation, and defined for each lamina with a ply orientation angle θ as:

$$[\tilde{T}_1] = \begin{bmatrix} \cos \theta & -\sin \theta \\ \sin \theta & \cos \theta \end{bmatrix} \quad [-] \quad (\text{C.15})$$

Shear forces are obtained by integrating the shear stresses through the thickness of a laminate:

$$\begin{aligned} \begin{Bmatrix} R_{yz} \\ R_{xz} \end{Bmatrix} &= K \int_{-h/2}^{h/2} [\bar{Q}]_{shear,k} dz \begin{Bmatrix} \gamma_{yz} \\ \gamma_{xz} \end{Bmatrix} = \\ &= K \left[\sum_{k=1}^n \int_{h_{k-1}}^{h_k} [\bar{Q}]_{shear,k} dz \right] \begin{Bmatrix} \gamma_{yz} \\ \gamma_{xz} \end{Bmatrix} = K \left[\sum_{k=1}^n [\bar{Q}]_{shear,k} \int_{h_{k-1}}^{h_k} dz \right] \begin{Bmatrix} \gamma_{yz} \\ \gamma_{xz} \end{Bmatrix} \quad [\text{N/mm}] \quad (\text{C.16}) \end{aligned}$$

Equation (C.16) can be simplified similar as before by introducing the shear stiffness matrix as follows:

$$\begin{Bmatrix} R_{yz} \\ R_{xz} \end{Bmatrix} = [A]_s \begin{Bmatrix} \gamma_{xz} \\ \gamma_{yz} \end{Bmatrix} \quad [\text{N/mm}] \quad (\text{C.17})$$

$$[A]_s = K \begin{bmatrix} A_{44} & A_{45} \\ A_{45} & A_{55} \end{bmatrix} = K \sum_{k=1}^n [\bar{Q}]_{shear,k} (h_k - h_{k-1}) \quad [\text{N/mm}] \quad (\text{C.18})$$

Appendix D – Energy principles

In this chapter an overview of different energy principles are presented and summarized from Reddy (2004), Byklum (2002) and Yoo and Lee (2011).

D.1 Potential energy

The potential energy of a system describes the amount of work that the system can perform, which depends on the internal/elastic strain energy and the potential of applied loads. The applied load has a potential if the load has the capacity to do work on a system during displacement in the system.

The potential energy for a static problem can be written as:

$$\Pi = U + W \quad [\text{Nmm}] \quad (\text{D.1})$$

where U is the internal strain energy and W is the load potential. For a dynamic problem, kinetic energy has to be added to the expression for the potential energy.

The strain energy density is the energy that is needed to deform a unit volume of material and it is defined as:

$$U_0 = \int_{\varepsilon} \{\sigma\}^T d\varepsilon = \frac{1}{2} \{\sigma\}^T \{\varepsilon\} = \frac{1}{2} \{\varepsilon\}^T [E] \{\varepsilon\} \quad [\text{N/mm}^2] \quad (\text{D.2})$$

The total strain energy of the plate is then the integration of the strain energy density over the whole volume of the body:

$$U = \int_V U_0 dV = \frac{1}{2} \{\sigma\}^T \{\varepsilon\} = \frac{1}{2} \int_V \{\varepsilon\}^T [E] \{\varepsilon\} dV \quad [\text{Nmm}] \quad (\text{D.3})$$

In general, the stress $\{\sigma\}$ and the strain $\{\varepsilon\}$ vectors each have six components and the material matrix $[E]$ is six by six in size. Since for sandwich plates the Mindlin-Reissner plate theory is applied, where the transverse normal strain ε_{zz} is neglected, the stress and strain vectors have only five components and the material matrix is five by five in size.

The total strain energy can be written in the form of the sum of the strain energies due to stretching (U_m , the membrane strain energy) and bending (U_b , the bending strain energy) for reasons of convenience when one looks at sandwich/composite plates. If the plate is asymmetric, the strain energy due to bending-stretching coupling should be added to the sum (U_{mb} , the bending-stretching strain energy). Energy contribution of the shear strains should be accounted for as well (U_s , the shear strain energy). The total strain energy is then:

$$U = U_m + U_b + U_{mb} + U_s \quad [\text{Nmm}] \quad (\text{D.4})$$

The external load potential is a sum of the work done by body loads, which act on the whole body's volume, and surface loads, which act only on the surface. It can be obtained as:

$$W = - \int_V \{u\}^T \{f_b\} dV - \int_S \{u\}^T \{f_s\} dS \quad [\text{Nmm}] \quad (\text{D.5})$$

where $\{u\}$ is a displacement vector, $\{f_b\}$ is a body loads vector and $\{f_s\}$ is a surface loads vector.

Combining Equations (D.3) and (D.5) the final expression for the total potential energy is obtained as:

$$\Pi = U + W = \frac{1}{2} \int_V \{\varepsilon\}^T [E] \{\varepsilon\} dV - \int_V \{u\}^T \{f_b\} dV - \int_S \{u\}^T \{f_s\} dS \quad [\text{Nmm}] \quad (\text{D.6})$$

D.2 The principle of virtual work

The principle of virtual work states that a system is in static equilibrium if the sum of virtual work of internal and external forces is zero for all virtual deformations and strains. These virtual deformations do not need to have any relation to the actual displacement caused by the loading. However, they have to be kinematically allowed.

$$\delta\Pi = \delta U + \delta W = 0 \quad (\text{D.7})$$

where δU is internal virtual work of the plate, δW is virtual work of external loads and δ is the variational operator, which denotes the “change” of the virtual work.

Since the solution to the nonlinear buckling problem, which is calculated using incremented method, is of interest in this thesis, the rates of the virtual work are solved for every increment. Therefore, the rate form of the principle of virtual work is being used:

$$\delta\dot{\Pi} = \delta\dot{U} + \delta\dot{W} = 0 \quad (\text{D.8})$$

where the dot represents the differentiation with respect to a rate parameter.

D.3 The principle of stationary potential energy

From the principle of virtual work, the principle of minimum potential energy is derived. It states that of all the possible deflections satisfying kinematic compatibility, those which satisfy static equilibrium will give a stationary value of the potential energy of the body, Byklum (2002). This can be expressed as:

$$\delta\Pi = \delta U + \delta W = 0 \quad (\text{D.9})$$

The principle is only valid for conservative, i.e. reversible, systems, where the material is elastic, but not necessarily linear elastic, and where the loads are directionally constant.

The system is a stable one if this stationary point of Π is also its minimum value. If the deformed configuration is described by the deflection w , the latter can be written as:

$$\frac{\partial\Pi}{\partial w} = 0 \quad (\text{D.10})$$

The principle of minimum potential energy can also be used on rate form:

$$\frac{\partial\dot{\Pi}}{\partial w} = 0 \quad (\text{D.11})$$

Appendix E – The Rayleigh-Ritz method

This chapter gives general information about the Rayleigh-Ritz method based on the work presented in Cook et al. (2002). General derivations and expressions implemented in the Sandwich PULS code, which are presented in this chapter, are based on the work done by Hareide (2012).

E.1 General introduction

The Rayleigh-Ritz method has been a well-known approximation method, also for the plate buckling problem, which is of interest in this thesis. For buckling of composite plates, the Rayleigh-Ritz method has some advantages over the direct, i.e. analytical, solutions since they are only limited for special cases. Unlike for analytical solutions, the Rayleigh-Ritz method describes the sought variable using a series of admissible functions together with unknown amplitudes, which are found using the principle of minimum potential energy.

These functions should be simple enough and practicable to use. The choice is usually limited to polynomials and occasionally sine and cosine functions. These series expressions are called shape or trail functions and are truncated at a finite number of terms, i.e. degrees of freedom. In order for the approximated system to converge the trial functions need to be complete. Completeness is satisfied if the exact displacements and their derivatives that appear in the potential energy formulation can be matched arbitrarily closely and if enough terms are used in the trail functions, Cook et al. (2002).

It should be mentioned that deflections approximated with the Rayleigh-Ritz method are under-predicted. This is due to the fact that the exact deflection shape is smooth and that it always takes the form of the least resistance. Even though the large number of degrees of freedom is used for the approximation, the approximated system will be made stiffer than it really is, since any other form than the exact one with the least resistance introduces slightly higher resistance, i.e. stiffness, Cook et al. (2002).

For the buckling problem the potential energy is described with approximated displacement and rotations, w_1 , w_2 and w_3 , which can be defined as:

$$w_1 = \sum_{m=1}^M \sum_{n=1}^N A_{mn} f(x)_m f(y)_n \quad [\text{mm}] \quad (\text{E.1a})$$

$$w_2 = \sum_{m=1}^M \sum_{n=1}^N B_{mn} f(x)_m f(y)_n \quad [-] \quad (\text{E.1b})$$

$$w_3 = \sum_{m=1}^M \sum_{n=1}^N C_{mn} f(x)_m f(y)_n \quad [-] \quad (\text{E.1c})$$

then the potential energy is described by several linear independent functions:

$$\Pi = \Pi(w_1, w_2, w_3) \rightarrow \Pi = \Pi(A_{11}, \dots, A_{MN}, B_{11}, \dots, B_{MN}, C_{11}, \dots, C_{MN}) \quad (\text{E.2})$$

where A_{mn} , B_{mn} and C_{mn} are the unknown amplitudes and $f(x)_m$ and $f(y)_n$ are the trial functions.

E.2 Displacement functions

The Rayleigh-Ritz approximated displacement functions used in the Sandwich PULS code are expressed as:

$$w = \sum_{m=1}^M \sum_{n=1}^N A_{mn} \sin \frac{m\pi x}{a} \sin \frac{n\pi y}{b} \quad [\text{mm}] \quad (\text{E.8a})$$

$$\gamma_{xz} = \sum_{m=1}^M \sum_{n=1}^N B_{mn} \cos \frac{m\pi x}{a} \sin \frac{n\pi y}{b} \quad [-] \quad (\text{E.8b})$$

$$\gamma_{yz} = \sum_{m=1}^M \sum_{n=1}^N C_{mn} \sin \frac{m\pi x}{a} \cos \frac{n\pi y}{b} \quad [-] \quad (\text{E.8c})$$

where M and N are the number of degrees of freedom used in the Rayleigh-Ritz approximation method. If they are set to infinity, the approximated series will limit to the exact solution. Therefore, finding a finite number of degrees of freedom that satisfies the convergence conditions, is crucial.

E.3 Differentiated displacement functions

To solve the plate buckling problem using the Rayleigh-Ritz method, the differentiated displacement functions need to be obtained in order to be later used in the expressions for the potential energy of the plate. The differentiated expressions are:

$$\frac{\partial w}{\partial x} = \sum_{m=1}^M \sum_{n=1}^N A_{mn} \left(\frac{m\pi}{a} \right) \cos \frac{m\pi x}{a} \sin \frac{n\pi y}{b} \quad [-] \quad (\text{E.9a})$$

$$\frac{\partial w}{\partial y} = \sum_{m=1}^M \sum_{n=1}^N A_{mn} \left(\frac{n\pi}{b} \right) \sin \frac{m\pi x}{a} \cos \frac{n\pi y}{b} \quad [-] \quad (\text{E.9b})$$

$$\frac{\partial^2 w}{\partial x^2} = - \sum_{m=1}^M \sum_{n=1}^N A_{mn} \left(\frac{m\pi}{a} \right)^2 \sin \frac{m\pi x}{a} \sin \frac{n\pi y}{b} \quad [-/\text{mm}] \quad (\text{E.9c})$$

$$\frac{\partial^2 w}{\partial y^2} = - \sum_{m=1}^M \sum_{n=1}^N A_{mn} \left(\frac{n\pi}{b} \right)^2 \sin \frac{m\pi x}{a} \sin \frac{n\pi y}{b} \quad [-/\text{mm}] \quad (\text{E.9d})$$

$$\frac{\partial^2 w}{\partial x \partial y} = \sum_{m=1}^M \sum_{n=1}^N A_{mn} \left(\frac{m\pi}{a} \right) \left(\frac{n\pi}{b} \right) \cos \frac{m\pi x}{a} \cos \frac{n\pi y}{b} \quad [-/\text{mm}] \quad (\text{E.9e})$$

$$\frac{\partial \gamma_{xz}}{\partial x} = - \sum_{m=1}^M \sum_{n=1}^N B_{mn} \left(\frac{m\pi}{a} \right) \sin \frac{m\pi x}{a} \sin \frac{n\pi y}{b} \quad [-/\text{mm}] \quad (\text{E.9f})$$

$$\frac{\partial \gamma_{xz}}{\partial y} = \sum_{m=1}^M \sum_{n=1}^N B_{mn} \left(\frac{n\pi}{b} \right) \cos \frac{m\pi x}{a} \cos \frac{n\pi y}{b} \quad [-/\text{mm}] \quad (\text{E.9g})$$

$$\frac{\partial \gamma_{yz}}{\partial x} = \sum_{m=1}^M \sum_{n=1}^N C_{mn} \left(\frac{m\pi}{a} \right) \cos \frac{m\pi x}{a} \cos \frac{n\pi y}{b} \quad [-/\text{mm}] \quad (\text{E.9h})$$

$$\frac{\partial \gamma_{yz}}{\partial y} = - \sum_{m=1}^M \sum_{n=1}^N C_{mn} \left(\frac{n\pi}{b} \right) \sin \frac{m\pi x}{a} \sin \frac{n\pi y}{b} \quad [-/\text{mm}] \quad (\text{E.9i})$$

E.4 Energy contributions

Only energy contributions from the bending and shear strains are presented here, since these are the ones that change if the FSDT is applied. Their energy contribution can be expressed as:

$$\begin{aligned}
 U &= \frac{1}{2} \int_A \left(\{\kappa\}^T [D] \{\kappa\} + t_c G_{c,xz} \gamma_{xz} \gamma_{xz} + t_c G_{c,yz} \gamma_{yz} \gamma_{yz} \right) dA = \\
 &= \frac{1}{2} \int_0^a \int_0^b \left[D_{11} (k_x)^2 + 2D_{12} k_x k_y + D_{22} (k_y)^2 + 2D_{16} k_x k_{xy} + \right. \\
 &\quad \left. + 2D_{26} k_y k_{xy} + D_{66} (k_{xy})^2 + t_c G_{c,xz} \gamma_{xz} \gamma_{xz} + t_c G_{c,yz} \gamma_{yz} \gamma_{yz} \right] dx dy = \\
 &= \frac{1}{2} \int_0^a \int_0^b \left[D_{11} \left(\frac{\partial}{\partial x} \left(\frac{\partial w}{\partial x} - \gamma_{xz} \right) \right)^2 + D_{22} \left(\frac{\partial}{\partial y} \left(\frac{\partial w}{\partial y} - \gamma_{yz} \right) \right)^2 + \right. \\
 &\quad \left. + 2D_{12} \left(\frac{\partial}{\partial x} \left(\frac{\partial w}{\partial x} - \gamma_{xz} \right) \right) \left(\frac{\partial}{\partial y} \left(\frac{\partial w}{\partial y} - \gamma_{yz} \right) \right) + \right. \\
 &\quad \left. + 2D_{16} \left(\frac{\partial}{\partial x} \left(\frac{\partial w}{\partial x} - \gamma_{xz} \right) \right) \left(\frac{\partial}{\partial y} \left(\frac{\partial w}{\partial x} - \gamma_{xz} \right) + \frac{\partial}{\partial x} \left(\frac{\partial w}{\partial y} - \gamma_{yz} \right) \right) + \right. \\
 &\quad \left. + 2D_{26} \left(\frac{\partial}{\partial y} \left(\frac{\partial w}{\partial y} - \gamma_{yz} \right) \right) \left(\frac{\partial}{\partial y} \left(\frac{\partial w}{\partial x} - \gamma_{xz} \right) + \frac{\partial}{\partial x} \left(\frac{\partial w}{\partial y} - \gamma_{yz} \right) \right) + \right. \\
 &\quad \left. + D_{66} \left(\frac{\partial}{\partial y} \left(\frac{\partial w}{\partial x} - \gamma_{xz} \right) + \frac{\partial}{\partial x} \left(\frac{\partial w}{\partial y} - \gamma_{yz} \right) \right)^2 + \right. \\
 &\quad \left. + t_c G_{c,xz} \gamma_{xz} \gamma_{xz} + t_c G_{c,yz} \gamma_{yz} \gamma_{yz} \right] dx dy
 \end{aligned} \tag{E.10a}$$

$$\begin{aligned}
 U &= \frac{1}{2} \int_0^a \int_0^b \left[D_{11} \left(\frac{\partial^2 w}{\partial x^2} - \frac{\partial \gamma_{xz}}{\partial x} \right)^2 + D_{22} \left(\frac{\partial^2 w}{\partial y^2} - \frac{\partial \gamma_{yz}}{\partial y} \right)^2 + \right. \\
 &\quad \left. + 2D_{12} \left(\frac{\partial^2 w}{\partial x^2} - \frac{\partial \gamma_{xz}}{\partial x} \right) \left(\frac{\partial^2 w}{\partial y^2} - \frac{\partial \gamma_{yz}}{\partial y} \right) + \right. \\
 &\quad \left. + 2D_{16} \left(\frac{\partial^2 w}{\partial x^2} - \frac{\partial \gamma_{xz}}{\partial x} \right) \left(2 \frac{\partial^2 w}{\partial x \partial y} - \frac{\partial \gamma_{xz}}{\partial y} - \frac{\partial \gamma_{yz}}{\partial x} \right) + \right. \\
 &\quad \left. + 2D_{26} \left(\frac{\partial^2 w}{\partial y^2} - \frac{\partial \gamma_{yz}}{\partial y} \right) \left(2 \frac{\partial^2 w}{\partial x \partial y} - \frac{\partial \gamma_{xz}}{\partial y} - \frac{\partial \gamma_{yz}}{\partial x} \right) + \right. \\
 &\quad \left. + D_{66} \left(2 \frac{\partial^2 w}{\partial x \partial y} - \frac{\partial \gamma_{xz}}{\partial y} - \frac{\partial \gamma_{yz}}{\partial x} \right)^2 + \right. \\
 &\quad \left. + t_c G_{c,xz} \gamma_{xz} \gamma_{xz} + t_c G_{c,yz} \gamma_{yz} \gamma_{yz} \right] dx dy
 \end{aligned} \tag{E.10b}$$

When the differentiated displacement functions shown in Equations from (E.9a) to (E.9i) are inserted into the expression for the bending and shear strain energy, i.e Equation (E.10b), the following expressions are obtained step-by-step:

$$\begin{aligned}
U = \frac{1}{2} \int_0^a \int_0^b & \left[D_{11} \left(- \sum_{m=1}^M \sum_{n=1}^N A_{mn} \left(\frac{m\pi}{a} \right)^2 \sin \frac{m\pi x}{a} \sin \frac{n\pi y}{b} + \sum_{m=1}^M \sum_{n=1}^N B_{mn} \left(\frac{m\pi}{a} \right) \sin \frac{m\pi x}{a} \sin \frac{n\pi y}{b} \right)^2 + \right. \\
& + D_{22} \left(- \sum_{m=1}^M \sum_{n=1}^N A_{mn} \left(\frac{n\pi}{b} \right)^2 \sin \frac{m\pi x}{a} \sin \frac{n\pi y}{b} + \sum_{m=1}^M \sum_{n=1}^N C_{mn} \left(\frac{n\pi}{b} \right) \sin \frac{m\pi x}{a} \sin \frac{n\pi y}{b} \right)^2 + \\
& + 2D_{12} \left(- \sum_{m=1}^M \sum_{n=1}^N A_{mn} \left(\frac{m\pi}{a} \right)^2 \sin \frac{m\pi x}{a} \sin \frac{n\pi y}{b} + \sum_{m=1}^M \sum_{n=1}^N B_{mn} \left(\frac{m\pi}{a} \right) \sin \frac{m\pi x}{a} \sin \frac{n\pi y}{b} \right) \cdot \\
& \cdot \left(- \sum_{m=1}^M \sum_{n=1}^N A_{mn} \left(\frac{n\pi}{b} \right)^2 \sin \frac{m\pi x}{a} \sin \frac{n\pi y}{b} + \sum_{m=1}^M \sum_{n=1}^N C_{mn} \left(\frac{n\pi}{b} \right) \sin \frac{m\pi x}{a} \sin \frac{n\pi y}{b} \right) + \\
& + 2D_{16} \left(- \sum_{m=1}^M \sum_{n=1}^N A_{mn} \left(\frac{m\pi}{a} \right)^2 \sin \frac{m\pi x}{a} \sin \frac{n\pi y}{b} + \sum_{m=1}^M \sum_{n=1}^N B_{mn} \left(\frac{m\pi}{a} \right) \sin \frac{m\pi x}{a} \sin \frac{n\pi y}{b} \right) \cdot \\
& \cdot \left(2 \sum_{m=1}^M \sum_{n=1}^N A_{mn} \left(\frac{m\pi}{a} \right) \left(\frac{n\pi}{b} \right) \cos \frac{m\pi x}{a} \cos \frac{n\pi y}{b} + \right. \\
& \quad \left. - \sum_{m=1}^M \sum_{n=1}^N B_{mn} \left(\frac{n\pi}{b} \right) \cos \frac{m\pi x}{a} \cos \frac{n\pi y}{b} - \sum_{m=1}^M \sum_{n=1}^N C_{mn} \left(\frac{m\pi}{a} \right) \cos \frac{m\pi x}{a} \cos \frac{n\pi y}{b} \right) + \\
& + 2D_{26} \left(- \sum_{m=1}^M \sum_{n=1}^N A_{mn} \left(\frac{n\pi}{b} \right)^2 \sin \frac{m\pi x}{a} \sin \frac{n\pi y}{b} + \sum_{m=1}^M \sum_{n=1}^N C_{mn} \left(\frac{n\pi}{b} \right) \sin \frac{m\pi x}{a} \sin \frac{n\pi y}{b} \right) \cdot \\
& \cdot \left(2 \sum_{m=1}^M \sum_{n=1}^N A_{mn} \left(\frac{m\pi}{a} \right) \left(\frac{n\pi}{b} \right) \cos \frac{m\pi x}{a} \cos \frac{n\pi y}{b} + \right. \\
& \quad \left. - \sum_{m=1}^M \sum_{n=1}^N B_{mn} \left(\frac{n\pi}{b} \right) \cos \frac{m\pi x}{a} \cos \frac{n\pi y}{b} - \sum_{m=1}^M \sum_{n=1}^N C_{mn} \left(\frac{m\pi}{a} \right) \cos \frac{m\pi x}{a} \cos \frac{n\pi y}{b} \right) + \\
& + D_{66} \left(2 \sum_{m=1}^M \sum_{n=1}^N A_{mn} \left(\frac{m\pi}{a} \right) \left(\frac{n\pi}{b} \right) \cos \frac{m\pi x}{a} \cos \frac{n\pi y}{b} + \right. \\
& \quad \left. - \sum_{m=1}^M \sum_{n=1}^N B_{mn} \left(\frac{n\pi}{b} \right) \cos \frac{m\pi x}{a} \cos \frac{n\pi y}{b} - \sum_{m=1}^M \sum_{n=1}^N C_{mn} \left(\frac{m\pi}{a} \right) \cos \frac{m\pi x}{a} \cos \frac{n\pi y}{b} \right)^2 + \\
& \left. + t_c G_{c,xz} \left(\sum_{m=1}^M \sum_{n=1}^N B_{mn} \cos \frac{m\pi x}{a} \sin \frac{n\pi y}{b} \right)^2 + t_c G_{c,yz} \left(\sum_{m=1}^M \sum_{n=1}^N C_{mn} \sin \frac{m\pi x}{a} \cos \frac{n\pi y}{b} \right)^2 \right] dx dy
\end{aligned}
\tag{E.11a}$$

$$\begin{aligned}
U = & \frac{1}{2} \sum_{m=1}^M \sum_{n=1}^N \sum_{p=1}^P \sum_{q=1}^Q \int_0^a \int_0^b \left[D_{11} \left(A_{mn} A_{pq} \left(\frac{m\pi}{a} \right)^2 \left(\frac{p\pi}{a} \right)^2 - A_{mn} B_{pq} \left(\frac{m\pi}{a} \right)^2 \left(\frac{p\pi}{a} \right) + \right. \right. \\
& \left. \left. - A_{pq} B_{mn} \left(\frac{m\pi}{a} \right) \left(\frac{p\pi}{a} \right)^2 + B_{mn} B_{pq} \left(\frac{m\pi}{a} \right) \left(\frac{p\pi}{a} \right) \right) [SIN] + \right. \\
& + D_{22} \left(A_{mn} A_{pq} \left(\frac{n\pi}{b} \right)^2 \left(\frac{q\pi}{b} \right)^2 - A_{mn} C_{pq} \left(\frac{n\pi}{b} \right)^2 \left(\frac{q\pi}{b} \right) + \right. \\
& \left. \left. - A_{pq} C_{mn} \left(\frac{n\pi}{b} \right) \left(\frac{q\pi}{b} \right)^2 + C_{mn} C_{pq} \left(\frac{n\pi}{b} \right) \left(\frac{q\pi}{b} \right) \right) [SIN] + \right. \\
& + 2D_{12} \left(A_{mn} A_{pq} \left(\frac{m\pi}{a} \right)^2 \left(\frac{q\pi}{b} \right)^2 - A_{mn} C_{pq} \left(\frac{m\pi}{a} \right)^2 \left(\frac{q\pi}{b} \right) + \right. \\
& \left. \left. - A_{pq} B_{mn} \left(\frac{m\pi}{a} \right) \left(\frac{q\pi}{b} \right)^2 + B_{mn} C_{pq} \left(\frac{m\pi}{a} \right) \left(\frac{q\pi}{b} \right) \right) [SIN] + \right. \\
& + 2D_{16} \left(-2A_{mn} A_{pq} \left(\frac{m\pi}{a} \right)^2 \left(\frac{p\pi}{a} \right) \left(\frac{q\pi}{b} \right) + 2B_{mn} A_{pq} \left(\frac{m\pi}{a} \right) \left(\frac{p\pi}{a} \right) \left(\frac{q\pi}{b} \right) + \right. \\
& + A_{mn} B_{pq} \left(\frac{m\pi}{a} \right)^2 \left(\frac{q\pi}{b} \right) - B_{mn} B_{pq} \left(\frac{m\pi}{a} \right) \left(\frac{q\pi}{b} \right) + A_{mn} C_{pq} \left(\frac{m\pi}{a} \right)^2 \left(\frac{p\pi}{a} \right) + \right. \\
& \left. \left. - B_{mn} C_{pq} \left(\frac{m\pi}{a} \right) \left(\frac{p\pi}{a} \right) \right) [SIN \cdot COS] + \right. \\
& + 2D_{26} \left(-2A_{mn} A_{pq} \left(\frac{n\pi}{b} \right)^2 \left(\frac{p\pi}{a} \right) \left(\frac{q\pi}{b} \right) + 2C_{mn} A_{pq} \left(\frac{n\pi}{b} \right) \left(\frac{p\pi}{a} \right) \left(\frac{q\pi}{b} \right) + \right. \\
& + A_{mn} B_{pq} \left(\frac{n\pi}{b} \right)^2 \left(\frac{q\pi}{b} \right) - C_{mn} B_{pq} \left(\frac{n\pi}{b} \right) \left(\frac{q\pi}{b} \right) + A_{mn} C_{pq} \left(\frac{n\pi}{b} \right)^2 \left(\frac{p\pi}{a} \right) + \right. \\
& \left. \left. - C_{mn} C_{pq} \left(\frac{n\pi}{b} \right) \left(\frac{p\pi}{a} \right) \right) [SIN \cdot COS] + \right. \\
& + D_{66} \left(4A_{mn} A_{pq} \left(\frac{m\pi}{a} \right) \left(\frac{n\pi}{b} \right) \left(\frac{p\pi}{a} \right) \left(\frac{q\pi}{b} \right) - 2B_{mn} A_{pq} \left(\frac{n\pi}{b} \right) \left(\frac{p\pi}{a} \right) \left(\frac{q\pi}{b} \right) + \right. \\
& - 2C_{mn} A_{pq} \left(\frac{m\pi}{a} \right) \left(\frac{p\pi}{a} \right) \left(\frac{q\pi}{b} \right) - 2A_{mn} B_{pq} \left(\frac{m\pi}{a} \right) \left(\frac{n\pi}{b} \right) \left(\frac{q\pi}{b} \right) + \right. \\
& + B_{mn} B_{pq} \left(\frac{n\pi}{b} \right) \left(\frac{q\pi}{b} \right) + C_{mn} B_{pq} \left(\frac{m\pi}{a} \right) \left(\frac{q\pi}{b} \right) - 2A_{mn} C_{pq} \left(\frac{m\pi}{a} \right) \left(\frac{n\pi}{b} \right) \left(\frac{p\pi}{a} \right) + \right. \\
& \left. \left. + B_{mn} C_{pq} \left(\frac{n\pi}{b} \right) \left(\frac{p\pi}{a} \right) + C_{mn} C_{pq} \left(\frac{m\pi}{a} \right) \left(\frac{p\pi}{a} \right) \right) [COS] + \right. \\
& + t_c G_{c,xz} B_{mn} B_{pq} \cos \frac{m\pi x}{a} \sin \frac{n\pi y}{b} \cos \frac{p\pi x}{a} \sin \frac{q\pi y}{b} \\
& \left. + t_c G_{c,yz} C_{mn} C_{pq} \sin \frac{m\pi x}{a} \cos \frac{n\pi y}{b} \sin \frac{p\pi x}{a} \cos \frac{q\pi y}{b} \right] dx dy
\end{aligned}$$

(E.11b)

Some of the trigonometric functions found in Equation (E.11a) can be used in the simplified form in Equation (E.11b) as:

$$[SIN] = \sin \frac{m\pi x}{a} \sin \frac{n\pi y}{b} \sin \frac{p\pi x}{a} \sin \frac{q\pi y}{b} \quad [-] \quad (E.12a)$$

$$[COS] = \cos \frac{m\pi x}{a} \cos \frac{n\pi y}{b} \cos \frac{p\pi x}{a} \cos \frac{q\pi y}{b} \quad [-] \quad (E.12b)$$

$$[SIN \cdot COS] = \sin \frac{m\pi x}{a} \sin \frac{n\pi y}{b} \cos \frac{p\pi x}{a} \cos \frac{q\pi y}{b} \quad [-] \quad (E.12c)$$

E.5 Integrals used in the Rayleigh-Ritz method

The integrals appearing in the potential energy expressions are solved and yield the exact solution for a certain combination of set values for m, n, p and q .

Appearing in the terms with D_{11} , D_{12} and D_{22} :

$$\begin{aligned} \int_0^a \int_0^b \sin \frac{m\pi x}{a} \sin \frac{n\pi y}{b} \sin \frac{p\pi x}{a} \sin \frac{q\pi y}{b} dx dy &= \\ &= \int_0^a \sin \frac{m\pi x}{a} \sin \frac{p\pi x}{a} dx \int_0^b \sin \frac{n\pi y}{b} \sin \frac{q\pi y}{b} dy = \\ &= \begin{cases} \frac{a}{2} & \text{if } m = p \\ 0 & \text{if } m \neq p \end{cases} \cdot \begin{cases} \frac{b}{2} & \text{if } n = q \\ 0 & \text{if } n \neq q \end{cases} = \\ &= \begin{cases} \frac{ab}{4} & \text{if } m = p \text{ and } n = q \\ 0 & \text{otherwise} \end{cases} = \frac{ab}{4} \delta_{mp} \delta_{nq} \end{aligned} \quad (E.13)$$

Appearing in the terms with D_{66} :

$$\begin{aligned} \int_0^a \int_0^b \cos \frac{m\pi x}{a} \cos \frac{n\pi y}{b} \cos \frac{p\pi x}{a} \cos \frac{q\pi y}{b} dx dy &= \\ &= \int_0^a \cos \frac{m\pi x}{a} \cos \frac{p\pi x}{a} dx \int_0^b \cos \frac{n\pi y}{b} \cos \frac{q\pi y}{b} dy = \\ &= \begin{cases} \frac{a}{2} & \text{if } m = p \\ 0 & \text{if } m \neq p \end{cases} \cdot \begin{cases} \frac{b}{2} & \text{if } n = q \\ 0 & \text{if } n \neq q \end{cases} = \\ &= \begin{cases} \frac{ab}{4} & \text{if } m = p \text{ and } n = q \\ 0 & \text{otherwise} \end{cases} = \frac{ab}{4} \delta_{mp} \delta_{nq} \end{aligned} \quad (E.14)$$

Appearing in the terms with S_{xz} :

$$\begin{aligned}
& \int_0^a \int_0^b \cos \frac{m\pi x}{a} \sin \frac{n\pi y}{b} \cos \frac{p\pi x}{a} \sin \frac{q\pi y}{b} dx dy = \\
& = \int_0^a \cos \frac{m\pi x}{a} \cos \frac{p\pi x}{a} dx \int_0^b \sin \frac{n\pi y}{b} \sin \frac{q\pi y}{b} dy = \\
& = \begin{cases} \frac{a}{2} & \text{if } m = p \\ 0 & \text{if } m \neq p \end{cases} \cdot \begin{cases} \frac{b}{2} & \text{if } n = q \\ 0 & \text{if } n \neq q \end{cases} = \\
& = \begin{cases} \frac{ab}{4} & \text{if } m = p \text{ and } n = q \\ 0 & \text{otherwise} \end{cases} = \frac{ab}{4} \delta_{mp} \delta_{nq}
\end{aligned} \tag{E.15}$$

Appearing in the terms with S_{yz} :

$$\begin{aligned}
& \int_0^a \int_0^b \sin \frac{m\pi x}{a} \cos \frac{n\pi y}{b} \sin \frac{p\pi x}{a} \cos \frac{q\pi y}{b} dx dy = \\
& = \int_0^a \sin \frac{m\pi x}{a} \sin \frac{p\pi x}{a} dx \int_0^b \cos \frac{n\pi y}{b} \cos \frac{q\pi y}{b} dy = \\
& = \begin{cases} \frac{a}{2} & \text{if } m = p \\ 0 & \text{if } m \neq p \end{cases} \cdot \begin{cases} \frac{b}{2} & \text{if } n = q \\ 0 & \text{if } n \neq q \end{cases} = \\
& = \begin{cases} \frac{ab}{4} & \text{if } m = p \text{ and } n = q \\ 0 & \text{otherwise} \end{cases} = \frac{ab}{4} \delta_{mp} \delta_{nq}
\end{aligned} \tag{E.16}$$

Appearing in the term with D_{16} and D_{26} :

$$\begin{aligned}
& \int_0^a \int_0^b \sin \frac{m\pi x}{a} \sin \frac{n\pi y}{b} \cos \frac{p\pi x}{a} \cos \frac{q\pi y}{b} dx dy = \\
& = \int_0^a \cos \frac{p\pi x}{a} \sin \frac{m\pi x}{a} dx \int_0^b \sin \frac{n\pi y}{b} \cos \frac{q\pi y}{b} dy = \\
& = \begin{cases} \frac{a[1 - (-1)^m (-1)^p]m}{\pi^2(m^2 - p^2)} & \text{if } m \neq p \\ 0 & \text{if } m = p \end{cases} \cdot \begin{cases} \frac{b[1 - (-1)^n (-1)^q]n}{\pi^2(n^2 - q^2)} & \text{if } n \neq q \\ 0 & \text{if } n = q \end{cases} = \\
& = \left[\frac{a[1 - (-1)^m (-1)^p]m}{\pi^2(m^2 - p^2)} \right] \left[\frac{b[1 - (-1)^n (-1)^q]n}{\pi^2(n^2 - q^2)} \right] I_{mp} I_{nq}
\end{aligned} \tag{E.17}$$

The terms δ_{mp} and δ_{nq} , which are the Kronecker deltas, are used to simplify the Equations from (E.13) to (E.16). They ensure that the integrals are non-zero only for terms where m equals p and for the terms where n equals q .

Similarly, the terms I_{mp} and I_{nq} are defined and used in Equation (E.17), which ensure that the integrals are non-zero only for the terms when m is not equal to p and for the terms where n is not equal to q .

E.6 Final expressions for energy contribution

After Equations from (E.13) to (E.17) and Equation (E.11b) are combined together the final expression for the bending and shear strain energy contribution is obtained as:

$$\begin{aligned}
U = & \frac{1}{2} \sum_{m=1}^M \sum_{n=1}^N \left[D_{11} \left(A_{mn}^2 \left(\frac{m\pi}{a} \right)^4 - 2A_{mn} B_{mn} \left(\frac{m\pi}{a} \right)^3 + B_{mn}^2 \left(\frac{m\pi}{a} \right)^2 \right) + \right. \\
& + D_{22} \left(A_{mn}^2 \left(\frac{n\pi}{b} \right)^4 - 2A_{mn} C_{mn} \left(\frac{n\pi}{b} \right)^3 + C_{mn}^2 \left(\frac{n\pi}{b} \right)^2 \right) + \\
& + 2D_{12} \left(A_{mn}^2 \left(\frac{m\pi}{a} \right)^2 \left(\frac{n\pi}{b} \right)^2 - A_{mn} C_{mn} \left(\frac{m\pi}{a} \right)^2 \left(\frac{n\pi}{b} \right) + \right. \\
& \quad \left. - A_{mn} B_{mn} \left(\frac{m\pi}{a} \right) \left(\frac{n\pi}{b} \right)^2 + B_{mn} C_{mn} \left(\frac{m\pi}{a} \right) \left(\frac{n\pi}{b} \right) \right) + \\
& + D_{66} \left(4A_{mn}^2 \left(\frac{m\pi}{a} \right)^2 \left(\frac{n\pi}{b} \right)^2 - 4A_{mn} B_{mn} \left(\frac{m\pi}{a} \right) \left(\frac{n\pi}{b} \right)^2 + B_{mn}^2 \left(\frac{n\pi}{b} \right)^2 + \right. \\
& \quad \left. - 4A_{mn} C_{mn} \left(\frac{m\pi}{a} \right)^2 \left(\frac{n\pi}{b} \right) + 2B_{mn} C_{mn} \left(\frac{m\pi}{a} \right) \left(\frac{n\pi}{b} \right) + C_{mn}^2 \left(\frac{m\pi}{a} \right)^2 \right) + \\
& \quad \left. + t_c G_{c,xz} B_{mn}^2 + t_c G_{c,yz} C_{mn}^2 \right] \frac{ab}{4} + \\
& + \sum_{m=1}^M \sum_{n=1}^N \sum_{p=1}^P \sum_{q=1}^Q \left[D_{16} \left(-2A_{mn} A_{pq} \left(\frac{m\pi}{a} \right)^2 \left(\frac{p\pi}{a} \right) \left(\frac{q\pi}{b} \right) + 2B_{mn} A_{pq} \left(\frac{m\pi}{a} \right) \left(\frac{p\pi}{a} \right) \left(\frac{q\pi}{b} \right) + \right. \\
& \quad + A_{mn} B_{pq} \left(\frac{m\pi}{a} \right)^2 \left(\frac{q\pi}{b} \right) - B_{mn} B_{pq} \left(\frac{m\pi}{a} \right) \left(\frac{q\pi}{b} \right) + \\
& \quad + A_{mn} C_{pq} \left(\frac{m\pi}{a} \right)^2 \left(\frac{p\pi}{a} \right) - B_{mn} C_{pq} \left(\frac{m\pi}{a} \right) \left(\frac{p\pi}{a} \right) \right) + \\
& + D_{26} \left(-2A_{mn} A_{pq} \left(\frac{n\pi}{b} \right)^2 \left(\frac{p\pi}{a} \right) \left(\frac{q\pi}{b} \right) + 2C_{mn} A_{pq} \left(\frac{n\pi}{b} \right) \left(\frac{p\pi}{a} \right) \left(\frac{q\pi}{b} \right) + \right. \\
& \quad + A_{mn} B_{pq} \left(\frac{n\pi}{b} \right)^2 \left(\frac{q\pi}{b} \right) - C_{mn} B_{pq} \left(\frac{n\pi}{b} \right) \left(\frac{q\pi}{b} \right) + \\
& \quad \left. + A_{mn} C_{pq} \left(\frac{n\pi}{b} \right)^2 \left(\frac{p\pi}{a} \right) - C_{mn} C_{pq} \left(\frac{n\pi}{b} \right) \left(\frac{p\pi}{a} \right) \right) \right] \cdot \\
& \quad \cdot \left[\frac{a[1 - (-1)^m (-1)^p] m}{\pi^2 (m^2 - p^2)} \right] \left[\frac{b[1 - (-1)^n (-1)^q] n}{\pi^2 (n^2 - q^2)} \right] I_{mp} I_{nq}
\end{aligned} \tag{E.18}$$

Appendix F – Derived stiffness matrices

The derived stiffness matrices that are needed for the eigenvalue analysis and for the incremental solution method are presented in this chapter, together with the derivation process to obtain them.

F.1 Derivation process

When derivations for obtaining sub-matrices are made, the following chain rule is applied:

$$\begin{aligned}
 \frac{\partial f(m, n, p, q)}{\partial \alpha_{ij} \partial \beta_{kl}} &= \\
 &= \left[\frac{\partial}{\partial \alpha_{ij}} \left(\frac{\partial f(k, l, p, q)}{\partial \beta_{kl}} + \frac{\partial f(m, n, k, l)}{\partial \beta_{kl}} \right) \right]^{(1)} = \\
 &= \left[\frac{f(m, n, p, q, k, l)}{\partial \alpha_{ij}} \right]^{(2)} = \\
 &= \left[\frac{\partial f(i, j, p, q, k, l)}{\partial \alpha_{ij}} + \frac{\partial f(m, n, i, j, k, l)}{\partial \alpha_{ij}} \right]^{(3)} = \\
 &= [f(i, j, k, l)]^{(4)}
 \end{aligned} \tag{F.1}$$

The chain rule expressed in Equation (F.1) can be explained in the following four steps as well:

- (1): In the first term m and n are set to k and l and derived with respect to coefficient β_{kl} and in the second term p and q are set to k and l and derived with respect to coefficient β_{kl}
- (2): Result of the first derivation is a function dependent on m, n, p, q, k and l , which needs to be derived with respect to α_{ij}
- (3): Chain derivation rule is then repeated as in the first term m and n are set to i and j and derived with respect to the coefficient α_{ij} and in the second term p and q are set to i and j and derived with respect to the coefficient α_{ij}
- (4): The final result is a function dependent only on i, j, k and l

F.2 Derived eigenvalue stiffness matrices

$$\begin{aligned}
[K_{AA}^M] = & \sum_{i=1}^M \sum_{j=1}^N \left[D_{11} \left(\frac{i\pi}{a} \right)^4 + D_{22} \left(\frac{j\pi}{b} \right)^4 + (2D_{12} + 4D_{66}) \left(\frac{i\pi}{a} \right)^2 \left(\frac{j\pi}{b} \right)^2 \right] \frac{ab}{4} + \\
& - 2 \sum_{m=1}^M \sum_{n=1}^N \sum_{p=1}^P \sum_{q=1}^Q \left[D_{16} \left(\frac{i\pi}{a} \right)^2 \left(\frac{k\pi}{a} \right) \left(\frac{l\pi}{b} \right) + D_{26} \left(\frac{j\pi}{b} \right)^2 \left(\frac{k\pi}{a} \right) \left(\frac{l\pi}{b} \right) \right] \cdot \\
& \cdot \left[\frac{a[1 - (-1)^i (-1)^k] i}{\pi^2 (i^2 - k^2)} \right] \left[\frac{b[1 - (-1)^j (-1)^l] j}{\pi^2 (j^2 - l^2)} \right] I_{ik} I_{jl} + \\
& - 2 \sum_{m=1}^M \sum_{n=1}^N \sum_{p=1}^P \sum_{q=1}^Q \left[D_{16} \left(\frac{k\pi}{a} \right)^2 \left(\frac{i\pi}{a} \right) \left(\frac{j\pi}{b} \right) + D_{26} \left(\frac{l\pi}{b} \right)^2 \left(\frac{i\pi}{a} \right) \left(\frac{j\pi}{b} \right) \right] \cdot \\
& \cdot \left[\frac{a[1 - (-1)^k (-1)^i] k}{\pi^2 (k^2 - i^2)} \right] \left[\frac{b[1 - (-1)^l (-1)^j] l}{\pi^2 (l^2 - j^2)} \right] I_{ik} I_{jl}
\end{aligned} \tag{F.2}$$

$$\begin{aligned}
[K_{BB}^M] = & \sum_{m=1}^M \sum_{n=1}^N \left[D_{11} \left(\frac{i\pi}{a} \right)^2 + D_{66} \left(\frac{j\pi}{b} \right)^2 + t_c G_{c,xz} \right] \frac{ab}{4} + \\
& - \sum_{m=1}^M \sum_{n=1}^N \sum_{p=1}^P \sum_{q=1}^Q \left[D_{16} \left(\frac{i\pi}{a} \right) \left(\frac{l\pi}{b} \right) \right] \cdot \\
& \cdot \left[\frac{a[1 - (-1)^i (-1)^k] i}{\pi^2 (i^2 - k^2)} \right] \left[\frac{b[1 - (-1)^j (-1)^l] j}{\pi^2 (j^2 - l^2)} \right] I_{ik} I_{jl} + \\
& - \sum_{m=1}^M \sum_{n=1}^N \sum_{p=1}^P \sum_{q=1}^Q \left[D_{16} \left(\frac{k\pi}{a} \right) \left(\frac{j\pi}{b} \right) \right] \cdot \\
& \cdot \left[\frac{a[1 - (-1)^k (-1)^i] k}{\pi^2 (k^2 - i^2)} \right] \left[\frac{b[1 - (-1)^l (-1)^j] l}{\pi^2 (l^2 - j^2)} \right] I_{ik} I_{jl}
\end{aligned} \tag{F.3}$$

$$\begin{aligned}
[K_{CC}^M] = & \sum_{m=1}^M \sum_{n=1}^N \left[D_{22} \left(\frac{j\pi}{b} \right)^2 + D_{66} \left(\frac{i\pi}{a} \right)^2 + t_c G_{c,yz} \right] \frac{ab}{4} + \\
& - \sum_{m=1}^M \sum_{n=1}^N \sum_{p=1}^P \sum_{q=1}^Q \left[D_{26} \left(\frac{j\pi}{b} \right) \left(\frac{k\pi}{a} \right) \right] \cdot \\
& \cdot \left[\frac{a[1 - (-1)^i (-1)^k] i}{\pi^2 (i^2 - k^2)} \right] \left[\frac{b[1 - (-1)^j (-1)^l] j}{\pi^2 (j^2 - l^2)} \right] I_{ik} I_{jl} + \\
& - \sum_{m=1}^M \sum_{n=1}^N \sum_{p=1}^P \sum_{q=1}^Q \left[D_{26} \left(\frac{l\pi}{b} \right) \left(\frac{i\pi}{a} \right) \right] \cdot \\
& \cdot \left[\frac{a[1 - (-1)^k (-1)^i] k}{\pi^2 (k^2 - i^2)} \right] \left[\frac{b[1 - (-1)^l (-1)^j] l}{\pi^2 (l^2 - j^2)} \right] I_{ik} I_{jl}
\end{aligned} \tag{F.4}$$

$$\begin{aligned}
[K_{AB}^M] = & -\sum_{m=1}^M \sum_{n=1}^N \left[D_{11} \left(\frac{i\pi}{a} \right)^3 + (D_{12} + 2D_{66}) \left(\frac{i\pi}{a} \right) \left(\frac{j\pi}{b} \right)^2 \right] \frac{ab}{4} + \\
& + \sum_{m=1}^M \sum_{n=1}^N \sum_{p=1}^P \sum_{q=1}^Q \left[D_{16} \left(\frac{i\pi}{a} \right)^2 \left(\frac{l\pi}{b} \right) + D_{26} \left(\frac{j\pi}{b} \right)^2 \left(\frac{l\pi}{b} \right) \right] \cdot \\
& \cdot \left[\frac{a[1 - (-1)^i (-1)^k] i}{\pi^2 (i^2 - k^2)} \right] \left[\frac{b[1 - (-1)^j (-1)^l] j}{\pi^2 (j^2 - l^2)} \right] I_{ik} I_{jl} + \quad (F.5) \\
& + \sum_{m=1}^M \sum_{n=1}^N \sum_{p=1}^P \sum_{q=1}^Q \left[2D_{16} \left(\frac{k\pi}{a} \right) \left(\frac{i\pi}{a} \right) \left(\frac{j\pi}{b} \right) \right] \cdot \\
& \cdot \left[\frac{a[1 - (-1)^k (-1)^i] k}{\pi^2 (k^2 - i^2)} \right] \left[\frac{b[1 - (-1)^l (-1)^j] l}{\pi^2 (l^2 - j^2)} \right] I_{ik} I_{jl}
\end{aligned}$$

$$\begin{aligned}
[K_{AC}^M] = & -\sum_{m=1}^M \sum_{n=1}^N \left[D_{22} \left(\frac{j\pi}{b} \right)^3 + (D_{12} + 2D_{66}) \left(\frac{i\pi}{a} \right)^2 \left(\frac{j\pi}{b} \right) \right] \frac{ab}{4} + \\
& + \sum_{m=1}^M \sum_{n=1}^N \sum_{p=1}^P \sum_{q=1}^Q \left[D_{16} \left(\frac{i\pi}{a} \right)^2 \left(\frac{k\pi}{a} \right) + D_{26} \left(\frac{j\pi}{b} \right)^2 \left(\frac{k\pi}{a} \right) \right] \cdot \\
& \cdot \left[\frac{a[1 - (-1)^i (-1)^k] i}{\pi^2 (i^2 - k^2)} \right] \left[\frac{b[1 - (-1)^j (-1)^l] j}{\pi^2 (j^2 - l^2)} \right] I_{ik} I_{jl} + \quad (F.6) \\
& + \sum_{m=1}^M \sum_{n=1}^N \sum_{p=1}^P \sum_{q=1}^Q \left[2D_{26} \left(\frac{l\pi}{b} \right) \left(\frac{i\pi}{a} \right) \left(\frac{j\pi}{b} \right) \right] \cdot \\
& \cdot \left[\frac{a[1 - (-1)^k (-1)^i] k}{\pi^2 (k^2 - i^2)} \right] \left[\frac{b[1 - (-1)^l (-1)^j] l}{\pi^2 (l^2 - j^2)} \right] I_{ik} I_{jl}
\end{aligned}$$

$$\begin{aligned}
[K_{BC}^M] = & \sum_{m=1}^M \sum_{n=1}^N \left[(D_{12} + D_{66}) \left(\frac{i\pi}{a} \right) \left(\frac{j\pi}{b} \right) \right] \frac{ab}{4} + \\
& - \sum_{m=1}^M \sum_{n=1}^N \sum_{p=1}^P \sum_{q=1}^Q \left[D_{16} \left(\frac{i\pi}{a} \right) \left(\frac{k\pi}{a} \right) \right] \cdot \\
& \cdot \left[\frac{a[1 - (-1)^i (-1)^k] i}{\pi^2 (i^2 - k^2)} \right] \left[\frac{b[1 - (-1)^j (-1)^l] j}{\pi^2 (j^2 - l^2)} \right] I_{ik} I_{jl} + \quad (F.7) \\
& - \sum_{m=1}^M \sum_{n=1}^N \sum_{p=1}^P \sum_{q=1}^Q \left[D_{26} \left(\frac{l\pi}{b} \right) \left(\frac{j\pi}{b} \right) \right] \cdot \\
& \cdot \left[\frac{a[1 - (-1)^k (-1)^i] k}{\pi^2 (k^2 - i^2)} \right] \left[\frac{b[1 - (-1)^l (-1)^j] l}{\pi^2 (l^2 - j^2)} \right] I_{ik} I_{jl}
\end{aligned}$$

In order to reduce computational effort and since the stiffness matrix is symmetrical, the following relations are implemented in the PULS code:

$$[K_{BA}^M] = [K_{AB}^M]^T \quad (\text{F.8a})$$

$$[K_{CA}^M] = [K_{AC}^M]^T \quad (\text{F.8b})$$

$$[K_{CB}^M] = [K_{BC}^M]^T \quad (\text{F.8c})$$

Appendix G – Hashin-Rotem/Hashin (Abaqus)

The Hashin-Rotem and the Hashin failure criteria are presented here as they are interpreted in Abaqus, see Dassault Systèmes (2014).

Failure in fibre tension:

$$\left(\frac{\sigma_{11}}{X_T}\right)^2 + \alpha \left(\frac{\tau_{12}}{S_L}\right)^2 = 1 \quad (\text{G.1})$$

Failure in fibre compression:

$$\left(\frac{\sigma_{11}}{X_C}\right)^2 = 1 \quad (\text{G.2})$$

Failure in matrix tension:

$$\left(\frac{\sigma_{22}}{Y_T}\right)^2 + \left(\frac{\tau_{12}}{S_L}\right)^2 = 1 \quad (\text{G.3})$$

Failure in matrix compression:

$$\left(\frac{\sigma_{22}}{2S_T}\right)^2 + \left[\left(\frac{Y_C}{2S_T}\right)^2 - 1\right] \frac{\sigma_{22}}{Y_C} + \left(\frac{\tau_{12}}{S_L}\right)^2 = 1 \quad (\text{G.4})$$

Where α is a coefficient that determines the contribution of the shear stress to the expression for the fibre tension failure. If $\alpha = 1$ the Hashin criteria are used, while if $\alpha = 0$ the Hashin-Rotem failure criteria are used as interpreted by Abaqus.